The ultrafast magnetisation dynamics and the role of the exchange interactions

Roberto Moreno Ortega

Advisor: Dr. Oksana Fesenko Morozova (Chubykalo-Fesenko)
Advisor: Dr. María del Carmen Muñoz de Pablo

Department Condensed Matter, Universidad Autonoma de Madrid

Tutor: Dr. Julio Camarero de Diego

A thesis submitted for the degree of

PhilosophiæDoctor (PhD), in Physics,

2017 April

Resumen

La manipulación de la configuración magnética de un material, en escalas de tiempo de picosegundos, usando pulsos laser cuya duración puede variar entre femtosegundos y picosegundos, y en ausencia de campo magnéticos aplicados, es hoy en día un campo de investigación importante para aplicaciones tecnológicas como, por ejemplo, nuevos sistemas de grabación magnética. De hecho, el utilizar pulsos laser en lugar campos magnéticos para invertir la imanación en un material, no solo conlleva un correspondiente ahorro energético si no que además el tiempo necesario para la inversión se reduce de nanosegundos a unos pocos picosegundos.

Este efecto, denominado en inglés como '*All Optical Switching*', debido a la ausencia de campos magnéticos externos para la inversión de la imanación, ha sido ampliamente comprobado de forma experimental para diferentes materiales como ferrimagnetos [10, 145], ferromagnetos [96] y sistemas de multicapas [103]. Sin embargo, a pesar del gran número de experimentos donde se ha observado este efecto, quedan todavía muchos aspectos por comprender. Por ejemplo, en algunos casos, la inversión de la imanación se produce dependiendo de la polarización del pulso de láser, en otros no. Además, en algunos casos, para producir la inversión de la imanación en un material es necesario que un gran número de pulsos láser incidan sobre el material, en otros, con un solo pulso es suficiente.

Desde un punto de vista fundamental, la inversión de la imanación por pulsos láser no ha sido completamente explicada. Por el contrario, algunos aspectos de este nuevo fenómeno si han conseguido ser descritos modelizando el efecto del pulso láser sobre el material. Véase por ejemplo como la inversión en FeGdCo, con un solo pulso láser, independientemente de la polarización del pulso incidente, ha sido modelizada utilizando simulaciones atomísticas basadas en la dinámica de Langevin, reproduciendo además el estado ferromagnetico transitorio que se produce durante la inversión entre las dos subredes del material ferrimagnético [123].

La dinámica ultrarápida de la imanación también puede ser modelizada utilzando simulaciones micromagnéticas a altas temperaturas basadas en la ecuación de Landau Lifshitz Bloch (LLB). En este tipo de simulaciones, el tamaño de los sistemas que se puede tener en cuenta es mayor. Esto permite analizar aspectos de la inversión por pulso láser como por ejemplo qué ocurre con las paredes de dominio del sistema.

Ambos métodos, simulaciones atomísticas y LLB, requieren de una correcta parametrización de las interactiones mágneticas que se tienen en cuenta, principalmente canje y anisotropía, para describir adecuadamente las propiedades de un material. De hecho, parametrizar adecuadamente la interación de canje se hace mas importante si cabe, porque la energía típica de estas interactiones corresponde, utilizando el principio de incertidumbre de Heisenberg, a la duración típica de los pulsos láser para los cuales se ha observado el efecto de *All Optical Switching*. Esto lleva a pensar que quizá, estas interacciones puedan ser especialmente relevantes para que inversión de la imanación ocurra.

Por lo tanto en esta tesis, con el objetivo de investigar el efecto de *All Optical Switching* desde un punto de vista teórico, presentamos los siguientes capítulos de resultados:

- Parametrización de la interacción de canje en simulaciones atomísticas (Hamiltoniano de Heisenberg) a partir de la aproximación de Tight Binding para Fe, Ni y Co.

- Parametrización de la interacción de canje y la dependencia de parámetros macroscópicos con la temperatura para LLB para Cobalto.

- Parametrización de la interacción de canje en simulaciones atomísticas, para una aleación desordenada de TbCo, a partir de los datos experimentales de la temperatura de Curie y de la temperatura de compensación de imanación previamente publicados. Estudio de la posibilidad de producir inversión de imanación en TbCo, usando simulaciones atomísticas, al ser excitado con pulsos láser cuya duración varía desde unas decenas de femtosegundos hasta picosegundos. Discusión de condiciónes de inversión basándose en este material como ejemplo.

- Modelización atomística de la dinámica de imanación ultrarápida en las estructuras cristalinas de fases de Laves C15 de TbFe y GdFe, utilizando las interacciones de canje calculadas a partir de primeros principios. Estudio de la influencia de la variación de la magnitud de las interacciones de canje en la inversión de imanación por pulsos láser para estas estructuras.

Contents

Si crees que has descubierto algo grande piensa que seguramente te hayas equivocado.

R. Ferreira

AGRADECIMIENTOS

1

Introduction.

1.1 Modern technological perspectives based on high temperature magnetisation dynamics.

Magnetic recording media industry demands new technologies for storage devices in which the bit density per inch, the energy consumption and the data writing speed are improved. Actual magnetic memory devices are based on magnetic materials with a strong perpendicular magnetic anisotropy (PMA) [1] that ensures the stability of the information under thermal fluctuations. Logical bits are stored, by setting up or down, the magnetisation of the perpendicular magnetic domains [2]. The usual way of reversing magnetisation domain (write a bit), is using an external stimuli (writing head) such as a magnetic field, pointing in the opposite direction of the magnetisation, in order to move the magnetisation to the magnetic field direction. Therefore, the external magnetic field must be greater than the corresponding anisotropy field of the media used for magnetic memory devices, to perform the magnetisation switching.

On one hand, the time needed for a bit writing process is directly related with the strength and duration of the magnetic applied field. Actual magnetic memory devices use writing heads that can create magnetic fields of ca. $1T$, which leads to switching times of nanoseconds order of magnitude [149]. An increase of the magnitude of the applied magnetic field implies a decrease of the magnetisation reversal time [18, 19], indeed, in 2002, Gerrits *et al* showed that a precessional magnetisation switching in $200ps$ is achieved using ultrashort strong magnetic pulses specifically shaped [53]. However, developing writing heads capable of

[1] The preferred direction of the magnetisation is perpendicular to the material

[2] Regions of the material in which the magnetisation is pointing to the same direction.

creating stronger magnetic fields than $1T$ is a challenge because of different technological issues. In addition, even in the case of developing a new generation of writing heads achieving higher magnetic fields, it was demonstrated by Tudosa *et al*, using ultrashort pulses of high magnetic fields ($\sim 3T$), that the magnetisation switching time, assisted only by magnetic fields, is limited, because at this extreme conditions the magnetisation breaks down into random paterns [66]. Additionally, strong fields require more energy.

On the other hand, the bit density per inch is related to the strength of the *PMA* of the magnetic material. If the magnitude of the *PMA* is increased, the stability of the magnetic domains under the effects of thermal fluctuations is increased too. Besides, the domain wall width [1] that separates magnetic domains is inversely proportional to the strength of *PMA*, thus, using magnetic materials with stronger *PMA* leads to the possibility of increasing the bit density per inch. Together with this, the strength of the magnetic field needed to switch the magnetisation increases, as the *PMA* of the magnetic materials does, which leads again to limitations on the magnetic field generation.

Therefore, because of the existing limitations of using stronger magnetic fields than the actually used to reverse magnetisation, novel technologies must be developed in order to continue increasing the data density and the data storage speed. To accomplish these requirements, many recent applications with appealing technological perspectives, based on the magnetization dynamics have been developed. Some of these possibilities include the use of high-temperature magnetisation dynamics as heat-assisted magnetic recording [91], thermally-assisted MRAMs [132], dynamics under thermal gradients (spin-Seebeck effect) [157]or ultrafast laser-induced magnetization dynamics [123], or.

The spin Seebeck effect [157], which is the spin analogue of the Seebeck effect, is defined as the generation of a spin current due to the presence of a temperature gradient. This feature opens the door to generate spin currents in spintronics devices using the heat generated by other devices, such as multiprocessors, which leads to the corresponding energy save. This new emerging field was called spin caloritronics [23].

Heat assisted magnetic recording (*HAMR*) [91] is a technology developed with the aim of reducing the magnitude of the external magnetic field and the corresponding energy consumption for data writing processes. In *HAMR*, heat assists the data recording process, because the magnetic anisotropy of a material decreases with increasing the temperature [113, 160]. Thus, heating the material

[1] A domain wall is a region of the magnetic material that separates two different magnetic domains varying the magnetisation from one domain to the other smoothly. The domain wall width refers to the distance needed to separate two magnetic domains smoothly.

during the writing process reduces the PMA, making the magnetic field value required to switch the magnetisation smaller. After the writing process, the system starts to cool down recovering its initial PMA value. Because of $HAMR$ has beaten the limitations imposed by the generation of stronger enough magnetic fields, ultra-high bit densities above $1Tb/inch^2$ have been reported [91]. A similar example is the temperature-assisted Magnetic random access memories where the heat generated by current assist s in magnetization switching [133].

Ultrafast laser induced magnetisation dynamics is defined as the possibility of controlling magnetisation with optical pulses instead of electric currents or magnetic fields. The first successful experiment using ultrashort laser pulses instead of other external stimulus to manipulate the magnetisation of a magnetic material, nickel in this case, was performed by Beaurepaire *et al* in 1996 [24]. However, it was in 2007, when Stanciu *et al* demonstrated that it was possible to reverse magnetisation (write a bit) in ferrimagnetic materials[1], $GdFeCo$ in this case, using circularly-polarised lases pulses [145] without the assistance of any other external stimuli, when this research field reached its maximum interest. In addition to the absence of an external magnetic field, they reported a magnetisation switching time of $2ps$, which beat the fastest writing event reported up that moment [53, 66], opening the door to a new generation of magnetic memory devices for which the data speed writing and the energy consumption are improved. Because of the magnetisation switching was successful only using laser pulses, this effect was dubbed *All Optical Switching* (AOS). Even more surprising was the work performed by Ostler *et al* [123], in which, both experimentally and with atomistic simulations, the authors reported the magnetisation reversal of a ferrimagnetic material on the picosecond time scale and below, using femtosecond laser pulses, independently of the polarization of the laser pulse and without the assistance of any external magnetic field. This effect, which is included in AOS, was named *Thermally induced magnetisation switching* ($TIMS$). AOS opens an incredible possibilities to save the energy in magnetic recording by removing the necessity of external field as well as to make the recording speed much faster. Indeed, recently, it has been demostrated that $TIMS$ can be carried out in $GdFeCo$ using the heat produced by ultrashort electric currents instead of laser pulses [170]. Besides, the reversal was accompanied by a record low dissipations. Yang *et al* reported that reversal occurs for a current pulse with a peak of $\sim 3mA$, which corresponds to an energy of $4fJ$ [170].

These three examples of new possibilities for spintronics devices show the necessity of investigating, both experimentally and theoretically, the magnetisation

[1]Materials in which two different sublattices are coupled antiferromagnetically.

dynamics at high temperatures. Here we will focus on the theoretical investigation of the *All Optical Switching* effect because this is the most recently discovered and astonishing effect of the presented above with incredible technological perspectives.

1.2 All optical switching.

1.2.1 Previous works on the ultrafast magnetisation switching

In the last two decades the development and availability of means of exciting magnetic materials on the sub-picosecond time-scale, such as femtosecond laser pulses [24, 25, 148], THz [72, 92] or mid-infrared sources, has given rise to a growing area of science broadly known as ultrafast spin dynamics. The interest in this field is on the one hand to understand the non-equilibrium processes and on the other - to use this knowledge to develop next generation technologies that operate at much higher data rates than present day technology.

The first successful attempt to manipulate magnetisation with ultrashort laser pulses was performed by Beaurepaire *et al* in 1996 [24]. In that work, it was demonstrated that Nickel metal (Ni), under the effect of an ultrashort laser pulse of $60fs$, demagnetizes after the laser pulse reaches the material on the timescale below $1ps$. The experimental results obtained in [24] are shown in fig. 1.1.

The interaction of the material magnetisation with the light at femtosecond time scale was unexplored at that moment, consequently, many experiments have been performed since Beaurepaire's results, using the similar time scales for the laser pulses and different materials instead of Ni. Among them, similar experiments with Ni were performed in order to confirm Beaurepaire's results [65, 140] as well as with Fe[32], Co [7, 58], magnetic semiconductors [161], dielectrics [83], half-metals [115], ferrimagnetic materials [9, 103, 145], $\left[Co/Pt\right]$ multilayers [96], FePt magnetic recording media[71, 108, 119] and synthetic ferrimagnets [103]. Some of these materials only demagnetize and recover the magnetisation after the laser pulse action as in Ni, in others the AOS has been reported. The first report on AOS is for $GdFeCo$ using circularly polarized laser pulses [145].

Since the discovery of AOS in $GdFeCo$ disordered alloys [145], great effort has been performed both theoretically and experimentally in order to explain the magnetisation reversal mechanisms as well as to find new materials exhibiting AOS. Indeed, AOS has been demostrated in other materials such as other ferrimagnets like $TbCo$ [9, 10] or $TbFe$ [60], ferromagnets [96]; and multilayer combination [48, 103, 167].

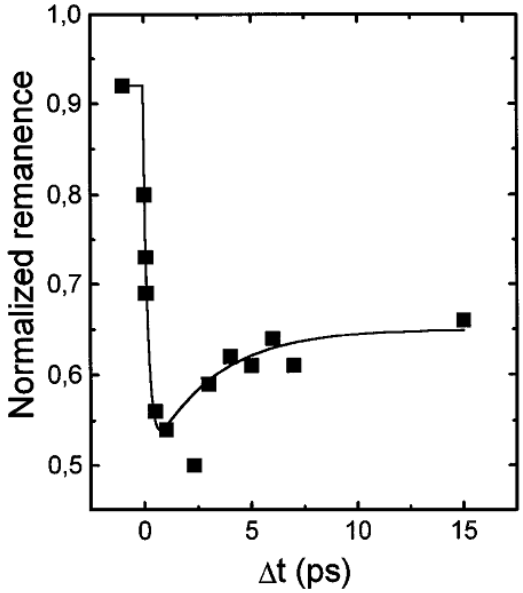

Figure 1.1: Experimental results of the ultrafast magnetic response in Nickel to a laser pulse of 60fs. Fig 1.1 has been extracted from [24]

For many materials exhibiting *AOS*, the magnetisation is reversed depending on the polarization of the incident laser pulse [10, 44, 96, 145], nevertheless, it has been demostrated both experimentally and theoretically that for $GdFeCo$ there is a large range of laser fluences for which the magnetisation is reversed independently of the polarization of the incident laser pulse[123, 135]. Thus, it is clear that there exists at least two different types of ultrafast magnetisation switching. The first one is dubbed helicity-dependent all optical switching *HD-AOS* [44], the second one is dubbed thermally induced magnetisation switching *TIMS* [123]. Typically, the helicity-dependent all optical switching requires multiple laser pulses to reverse magnetisation while the second if feasible with only a single, femtosecond laser pulse. Nevertheless, it has been demonstrated for $GdFeCo$ that the first type of switching, the *HD-AOS*, can be also achived with only one laser shot in the threshold of laser fluences for which *TIMS* appears [158].

Explaining the all optical switching effect in terms of direct transfer of angular

moment from the electrons to the spins is not possible, because, the total angular momentun of the photons is not strong enough to produce magnetisation changes in the material [88]. Direct estimations of the temperature needed to be reached by the electronic system for the ocurrence of the magnetisation reversal due to this process, gives as a result that the difference between the electronic temperature T_e and the Curie temperature (T_C)[1] must be $\sim 1mK$, which did not occur in the experiments [145]. On the fundamental level there is a strong debate on the mechanism of the angular momentum transfer and several quantum mechanical origins such as the Elliott-Yafet [33, 147] or the exchange scattering [20, 90] are under debate. The complete description of the switching from the quantum mechanical point of view, including the correct timescale, has not been reported so far and more phenomenological classical models based on the statistical mechanics (such as the Heisenberg atomistic modeling[46, 123, 135], the Landau-Lifshitz-Bloch equation [16, 47, 51], the M3TM [87] or the Baryakhtar model [109]) have been more succesful.

1.2.2 Helicity-dependent all optical switching

The first observation of magnetisation switching in ferrimagnetic alloys ($GdFeCo$) was reported by Hohlfeld *et al* in 2001 [64], using $100fs$ laser pulses and magnetic fields in order to stabilize the magnetization. However, it was in 2007 when Stanciu *et al* showed that for ferrimagnetic disorderd alloy of $Gd_{22}Fe_{74.6}Co_{3.4}$, the material magnetisation can be reversed with the help of the cumulative laser pulses of $40fs$ circularly polarized, leading a new controllable way of writing bits for modern storage devices [145]. The reversal took place in $2ps$ without the assistance of any external magnetic field.

In addition, the direction of the light polarization[2] in combination with the magnetisation direction of the domain where the pump pulse is applied, determined if the magnetisation is reversed or not. This is evidenced in Fig. 1.2, where different magnetic domains are presented before and after the laser pulses interact with them. We see that each circularly polarization set the magnetisation to opposite directions as well as the linerly laser pulses create random magnetic domains. Thus, this effect was dubbed helicity-dependent all optical switching *HD-AOS*.

Apart from ferrimagnetic materials, the *HD-AOS* effect has been also demostrated in ferromagnets such as $CoPt$ [96] or $FePt$ [71, 119], which are more interesting materials for data storage devices than ferrimagnets because, firstly,

[1] Temperature at which the material magnetization vanishes.
[2] Right circularly, left circuarly or linear.

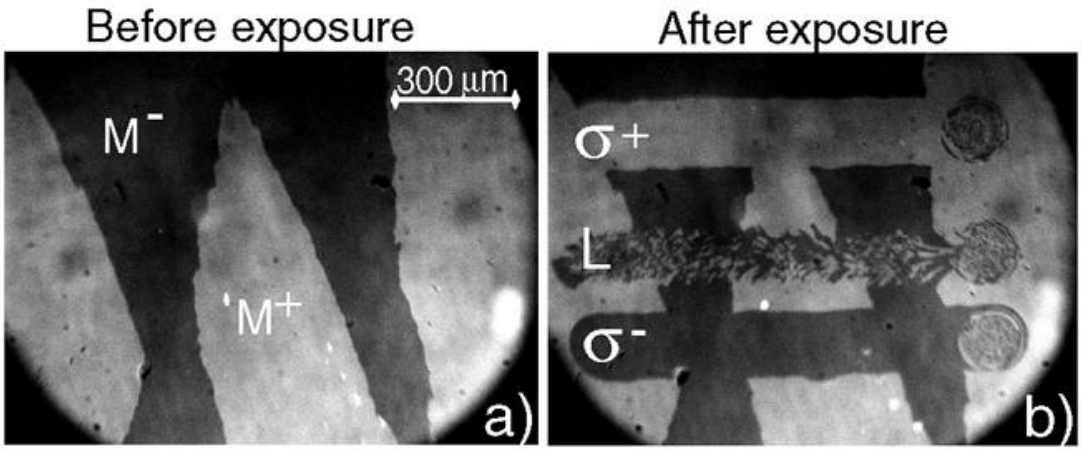

Figure 1.2: Ultrashort laser pulse effects on magnetic domains for $Gd_{22}Fe_{74.6}Co_{3.4}$. (a) Magnetic state before the exposure. White and black means domains with opposite magnetisation direction. (b) Magnetic state after the pump laser with polarization right-handed (σ^+), left-handed (σ^-) and linear (L). Figure 1.2 has been extracted from [145]

they are rare earth free, and secondly, they have a strong perpendicular magnetic anisotropy (*PMA*). However, in these cases the *HD-AOS* seems not to be possible with one laser pulse only.

The switching process was explained, at the beginning, with the combination of two different effects: firstly the energy of the laser pulse was absorbed by the electronic system leading to the corresponding ultrafast demagnetization, as in Fig 1.1 for *Ni*; secondly the circularly polarized laser pulse behaves like an effective magnetic field pointing parallel or antiparallel to the remaining magnetisation, stimulating the magnetisation direction for which the effective magnetic field of the laser pulse is pointing. The latter effect is called inverse Faraday effect *IFE* [82]. When the electronic temperature (T_e) reaches values close to T_{C}, the magnetic susceptibility diverges, which means that with the help of the effective magnetic field due to the laser pulse, magnetisation switching could be produced. Thus, this processes works like a heat assisted magnetic recording device but with the difference that there is no external magnetic field applied. However, estimations [119, 158] indicate that such a field must be strong (larger than 10 T) and act on the timescale larger than the laser pulse duration which seems

not to be feasible. Recent ab-initio theory [71] shows that the IFE acts rather a increase/decrease of the local magnetisation rather than an effective field.

Alternatively to the *IFE*, the magnetic circular dychroism *MCD* [1] has been suggested as the microscopic mechanism for the *HD-AOS* [79]. Recent calculations [71] have shown that the magnitudes of the IFE and MCD effects may be similar, both being the source for asymmetric spin-flip probability during the laser heating and thus we do not distinguish between them. Furthermore, the cumulative heating effect is likely to contribute to the reversal process where the system is driven close to the phase transition temperature. Consequently, during one laser pulse the effect is most probably small but is accumulating (similar to the superparamagnetic effect) in the experiments with many laser pulses.

Additionally, on the larger timescale the asymmetry in spin-flip probabilities leads to non-symmetric domain expansion, the domain sizes being proposed as the criterion for AOS [44, 107].

1.2.3 Second mechanism of ultrafast magnetisation switching: helicity-independent TIMS.

In 2011 Radu *et al* demonstrated by measurements with X-ray circular magnetic dichroism that for $Gd_{25}Fe_{65.6}Co_{9.4}$ a single linearly polarized laser pulse of $60fs$ was enough stimulus to switch the material magnetisation deterministically [135]. In addition, they showed that the magnetisation reversal occurs via transient ferromagnetic-like state between the different sublattices, which are coupled antiferromagnetically. To determine the different dynamics of the magnetisation corresponding to each sublattice, the transition metal ($FeCo$) and the rare-earth (Gd), an element-specific ($XMCD$), was used. First, as a consequence of the laser pulse, the $FeCo$ magnetisation reversed $300fs$ after the laser excitation. After that, the Gd magnetisation needed $1.5ps$ to reverse, leading to transient ferromagnetic-like state between both sublattices, what was completely unexpected. Besides, atomistic spin simulations of this effect were performed, confirming the existence of the transient ferromagnetic-like state, as a feature intrinsic to the ultrafast magnetisation switching. Fig. 1.3 shows the experimental data as well as the fittings performed by Radu *et al* of the switching process published in [135]. The transient ferromagnetic state has been suggested as a reason for the reversal. However, it is not clear if its existence is the reason for this effect or the consequence.

[1] Different absortion of light in materials induced by a magnetic field, depending on the polarization of the light

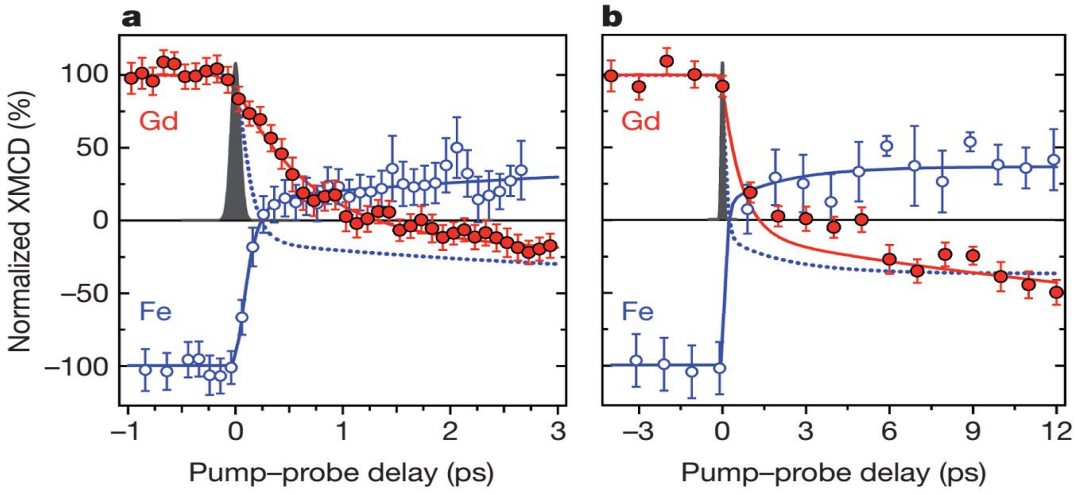

Figure 1.3: a) and b) represent the same experimental magnetisation dynamics of Fe (Red dots) and Gd (Blue dots) sublattices, together with their corresponding fittings (red and blue lines correspondly), for two different time scales. Fig. 1.3 have been extracted from [135]

In 2012, Ostler *et al*, based on the previous work published by Radu *et al*[135], demostrated that the magnetisation switching observed via transient ferromagnetic-like was completly independent of the light polarization of the incident laser pulse, besides, they proposed that only the thermal energy given by the laser pulse to the ferrimagnetic material is responsible of the magnetisation switching [123]. In addition, the atomistic simulations performed showed that the switching cannot be avoided with a magnetic field lower than $40T$ pointed in the opposite direction. Experimetally, they verified their theoretical results, showing that each laser pulse ($100fs$) is capable to reverse the magnetisation in $Gd_{25}Fe_{65.6}Co_{9.4}$ films, independently of the initial state of the magnetisation and the polarization of the light. This also occurred in materials with different compositions, in thin films and dots with in-plane and out-of plane anisotropy. Fig. 1.4 shows the experimental demonstration published in [123]. As the magnetisation is reversed due to the heat absorved by the sample from the laser pulse, this effect, which is included in AOS, was dubbed Thermally induced magnetisation switchig ($TIMS$).

TIMS is a deterministic phenomenon which does not require any asymmetry of the spin-flip probability coming from IFE, MCD or external field. The essential characteristics of the reversal is that the FeCo sublattice is faster than the Gd one.

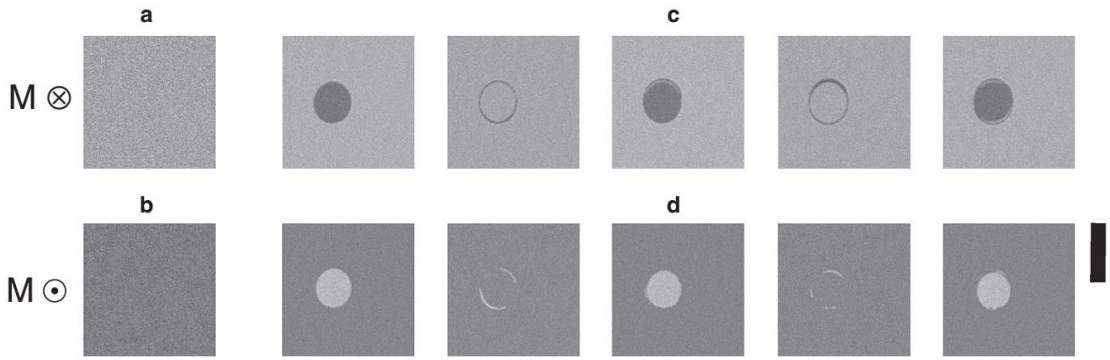

Figure 1.4: Figs. a) and b) are magneto-optical images showing the homogenously magnetized film (up and down respectively) of $Gd_{24}Fe_{66.5}Co_{9.5}$ before the laser pulse interaction. c) and d) are the magneto-optical images after each laser pulse. Fig. 1.3 have been extracted from [123]

Under the action of the laser heating it demagnetizes almost to zero while the Gd magnetisation remains constant and provides an exchange field responsible for the angular momentum transfer from one sublattice to another. In Refs. [123, 135], it was empirically demonstrated (see also discussion in Ref.[84]) that a number of requirements for TIMS must be satisfied to observe the phenomena. These include; (i) two or more magnetic species with antiferromagnetic exchange; (ii) different intrinsic demagnetization times of each sublatice; (iii) the presence and traversal of the magnetic compensation point, T_{M} [1]; and (iv) ultrashort laser pulses.

Recent works have used the pioneer results of [123, 135] to produce *TIMS* in $GdFeCo$ disordered alloys. Firstly, using larger pulses durations ($\sim ps$), which are much more interesting for technological implementation and heating directly the $GdFeCo$ sample [55]. Secondly, with the heat currents produced in $Au/GdFeCo$ bilayers by heating with laser pulses the gold surface [164]. Finally, the most interesting, *TIMS* was produced in $GdFeCo$ with the heat produced by ultrashort electric currents ($\sim 0.5ps$) [170].

[1] Temperature at which the material magnetization vanishes because the magnetization of the sublattices compensate each other.

TIMS has been also reported in other transition metal/rare earth compounds such as TbFeCo [101], which is more appealing from technological point of view due to their high anisotropy value, with laser pulses of $500fs$ and with the help of two gold nanoantennas leading to swithing areas of $53nm$ of diameter comparable with the $55nm$ recently reported using heat assisted magnetic recording [166].

1.3 The role of the magnetisation compensation point.

AOS is found in ferrimagnetic materials only for some range of rare-earth concentrations. Thus, two features widely discussed as a condition for the ocurrence of *AOS* in ferrimagnets are the existence of the angular momentum (T_{A}) or the magnetisation compensation (T_{M}) points and crossing these temperatures during the laser heating of the sample.

The angular momentum for each sublattice is defined as $A_i = M(T)_i/\gamma_i$, with $i = TM, RE$, $M(T)_i$ is the magnetisation of the sublattice i at some temperature T and γ_i corresponds to the gyromagnetic factor. Thus, the angular moment compensation temperature is defined as the temperature for which the angular momentum of both sublattices compensates.

$$\frac{M(T_A)_{RE}}{\gamma_{RE}} = \frac{M(T_A)_{TM}}{\gamma_{TM}} \tag{1.1}$$

The magnetisation compensation point in a ferrimagnetic material is defined as the temperature for which the magnetisations of both sublattices compensate each other, because they are coupled antiferromagnetically, leading to a net magnetisation equal to zero while the magnetisation of both sublattices is non zero [59]. Not for all the ferrimangnetic materials such a point exists, in many of them the two sublattices share the Curie temperature. To have a T_{M} some requirements must be accomplished.

Firstly, the concentration of rare earth in a ferrimagnetic material for which a T_{M} exists, is limited both above and below. In the case of existing, for low temperatures, the magnetisation has to be dominated by the rare earth sublattice because its atomic magnetic moment is bigger than for the transition metal sublattice. Usually, the rare earth Curie temperatures (T_{C}), in general, are lower than for transition metals, and therefore, their normalized magnetisation decrease stronger with temperature than the transition metal one leading to the existence of T_{M}.

Secondly, the antiferromagnetic exchange between sublattices must be in some range. It should be weak enough to enable different magnetisation versus temperature curves for each sublattice. Strong antiferromagnetic exchange makes the system to have similar magnetisation versus curves for each sublattice, and T_{M} does not exist.

The existance of the angular momentum compensation point is defined by a different gyromagnetic factor of the rare earth material than that of the transition metal. This temperature is normally very close to T_{M} and experimentally in disordered materials they are different to distinguish. Crossing this point was suggested as one of the first origins for the ultra fast reversal since the effective Gilbert damping parameter diverges there. Later it was demonstrated by atomistic modeling [139] that the damping parameter does not really diverge. Additionally, in modelling TIMS happens equally of one sets the same gyromagnetic factors for both sublattices.

Earlier works on AOS suggested that the fact that the electron temperature crossing T_{M} during the laser heating may play a fundamental role on the magnetisation switching, for example [155]. By contrast, it has been demonstrated in other works that the T_{M} is a relevant parameter for the occurrence of AOS but not essential, so that the role of T_{M} in AOS is still not clear. For example, on one hand, Ostler *et al* showed in [123] that the helicity independent switching mechanism occurs for $GdFeCo$ for some materials without T_{M} or starting the experiment with a room temperature (T_{Room}) above the T_{M} of the sample. Thus, to cross the T_{M} with the laser heating is not a necessary condition. On the other hand, the work performed by Alebrand *et al* on Tb_xCo_{1-x} [10] has reported the helicity dependent mechanism only in the range of Tb concentration for which a T_{M} exists and it is below the T_{Room}.

In 2013 Barker *et al*, proposed the origin of the helicity independent mechanism as the excitation of two magnon-bound states, via angular momentum transfer from the ferromagnetic to the antiferromagnetic spin wave modes [21]. Fig. 1.5 shows numerical simulations of $GdFeCo$ magnetisation dynamics for different rare earth concentration, as well as their corresponding magnon dispersion relations. The energy gap existing between the ferromagnetic and the antiferromagnetic bands depends on the concentration as the T_{M} does. For typical concentrations in which T_{M} exists, the energy gap between the ferromagnetic and the antiferromagnetic bands is small and reachable with the laser pulse energy. Thus, the most energy efficient AOS switching occurs for materials with the magnetisation compensation point although its existence is not completely necessary.

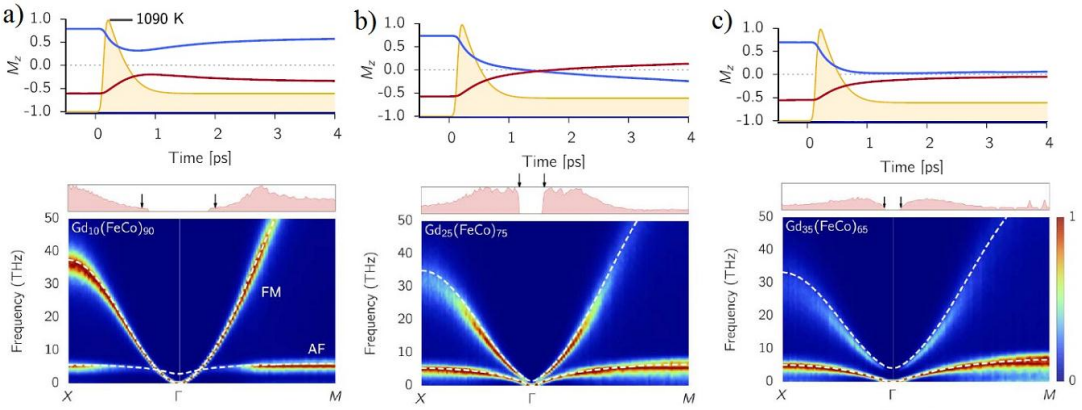

Figure 1.5: Numerical simulations of $GdFeCo$ magnetisation dynamics for different rare earth concentrations, as well as their corresponding magnon structures. a) $Gd_{10}(FeCo)_{90}$, b) $Gd_{25}(FeCo)_{75}$ and $Gd_{35}(FeCo)_{65}$. Fig. 1.5 Barker has been extracted from [21].

1.4 The time scale of the exchange interaction.

One feature common in both magnetisation reversal mechanisms presented before, is that the laser pulses used to carry out the switching, usually are in the femtosecond time scale. At this time scale, the physics governing the interaction between the light and the material magnetisation is still not clear, however, this time scale corresponds to the exchange interaction energy scale via the uncertainly principle $\Delta t \Delta E = \hbar/2$, where $\hbar$ is the Planck's constant divided by 2π. It means that this interaction plays the most important role in the occurrence of AOS. Fig. 1.6 shows the corresponding time scales associated with each magnetic energy term. In fact, neither anisotropy, nor the Zeeman energy have been shown to influence the AOS. The AOS happens even if very large fields are applied in the opposite direction [123]. It has been also reported in materials with in-plane and out-of-plane low and high anisotropy materials [10, 123]. Although of course the spin-orbit coupling must play an important role in the processes by promoting specific spin-flips events.

Theoretical results for AOS by Ostler *et al* in Ref. [123] were obtained from many-spin atomistic spin dynamics simulations[1] (ASD). In ASD, the exchange interaction is introduced in the spin Hamiltonian using the classical 3D Heisenberg model, see [50].

[1] In section 2 a detailed description of the ASD will be given .

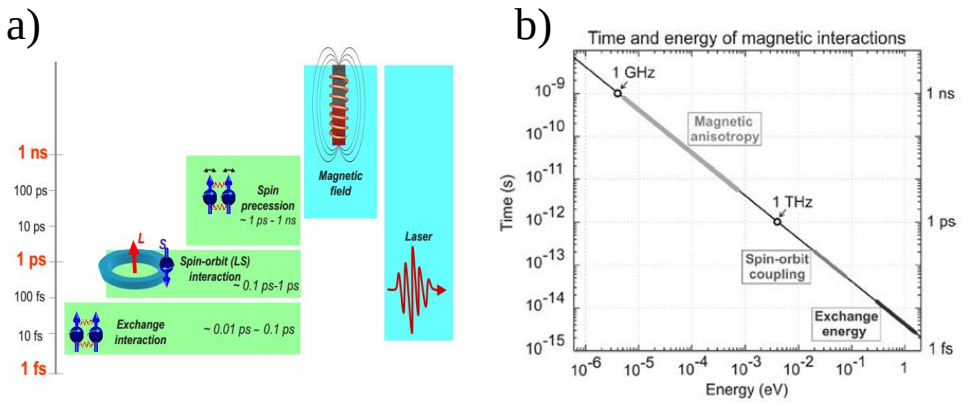

Figure 1.6: a) shows the time scales associated to the corresponding energy terms in magnetism and the energy of lasers or magnetic fields experimentally accesible. b) shows the energy value and the magnetism term that corresponds to the laser frecuency. Figure a and b has been extracted from Ref.[85],[149] respectively.

$$\mathbb{H} = -\frac{1}{2}\sum_{i,j} J_{ij} s_i \cdot s_j, \tag{1.2}$$

The exchange coupling parameters of the Heisenberg Hamiltonian J_{ij}, could be parametrized both from experimental data of the T_C or using the *ab initio* methods. For example, in Ref. [124] the authors parametrized the nearest-neighbour exchange interactions from experimental values of T_C and T_M as a function of Gd concentration, with good results. However, the magnetic exchange interaction is known to be long range, of RKKY type in transition metals. Therefore, while the *ab initio* calculations provide a more correct and long range parametrization, fitting from experimental data only provides first neighbours interactions.

As the exchange interaction is related with the laser pulse time scale, it becomes necessary to pay a special attention to this magnetic energy term, in order to investigate AOS from a theoretical point of view. Indeed, the timescale of the

magnetisation dynamics is defined by $\mu/\lambda T_c$ [150], where T_c is the Curie temperature and μ is the magnetic moment. The Curie temperature is directly related to exchange interactions, $J_{ij} \propto T_c$, see chapter 5. In the two-sublattice materials, ferrimagnets, this is more complicated and the Curie temperature is related to the exchange field acting on each sublattice [150]. Thus, the correct values of the exchange is of paramount importance for description of the *AOS* effect.

1.4.1 *AOS* with longer laser pulses.

It must be pointed out that the influence of the laser pulse duration on the occurrence of *AOS*, or in the specific case of the occurrence of $TIMS$, is still an open question. In fact, in spite of both magnetisation reversal mechanisms explained before were discovered using femtosecond laser pulses, recent experiments, for example, on *TbCo* disordered alloys demonstrated that the helicity dependent mechanism also occurs with laser pulses of $10ps$ and $400fs$ duration [10]. Fig. 1.7 shows the helicity dependence of the magnetisation switching under the effect of $10ps$ laser pulses on *TbCo* disordered alloys.

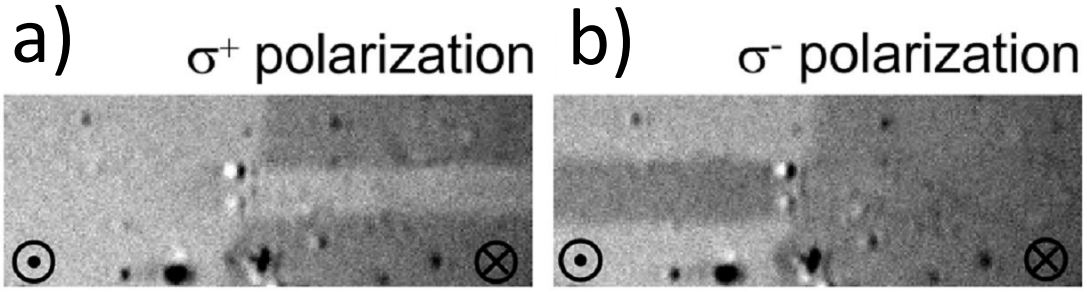

Figure 1.7: Helicity dependent magnetisation reversal for TbCo disordered alloys. The sample was initially prepared with two different magnetic domains. a) shows the results after sweeping a line with right handed polarized laser pulses. b) shows the corresponding results after sweeping with left handed polarized laser pulses. Fig. 1.7 has been extracted from [10].

Recently, experiments performed by Gorchon *et al* with $GdFeCo$ thin films showed that, even with longer laser pulses of $10ps$, the helicity independent switching mechanism is observed if the laser fluence is in some range of values [55]. The magnetisation reversal time is decreased as the laser pulse duration is increased, however, the switching occurs after all the laser pulse energy is deposited in the ferromangetic material. Thus, the switching time is still much

faster than in actual magnetic memory devices as well as the constrain of using expensive femtosecond laser is removed.

More surprising is the discovery of Wilson *et al* with $Au/GdFeCo$ bilayers [164]. In their experiment, a laser pulse duration up to $500fs$ heating the Au film instead of the $GdFeCo$, creates a temperature gradient between both layers, which generates heat currents flowing from the Au to the $GdFeCo$ film that produce AOS, or better said $TIMS$ because it is independent of the helicity of the incident laser pulse.

All these very recent findings indicate the necessity to investigate the influence of the laser pulse duration on the occurrence of AOS and more concretly TIMS.

1.5 About this thesis

As it has been discussed, all-optical laser-induced ultrafast magnetisation reversal is a promising technology for the next generation of magnetic memory devices as well as a really interesting physical effect from a fundamental point of view. Especially prmosing is TIMS; i.e. the deterministic reversal with once pulse. Because the physics underlying the AOS effect (especially on quantum level) is in reality unknown at this moment, in this thesis, we want to collaborate with the physical understanding of the mechanisms that produce switching as well as to determine the necessary conditions and material design in terms of the exchange interactions. We believe that this research could expedite the implementation of this new physical effect into future technology devices.

In this thesis we will focus on the atomistic spin simulations of TIMS in ferrimagnetic materials different from $GdFeCo$ which has been extensively both theoretically and experimentally studied. However, before simulating magnetic system, a correct description of the magnetic parameters involved in the calculations must be done. As majority of the experiments have been performed using femtosecond laser pulses, which are directly related with the exchange interaction on the energy scale, therefore we pay special attention to the parametrization of the exchange energy term. The thesis is structured as the following:

Chapter 2 This chapter discusses the models used in the system. The atomistic spin Hamiltonian is described together with the Landau-Lifshitz-Gilbert dynamics equation. The thermal fluctuations are included to describe high temperature magnetisation dynamics, called Langevin dynamics. In addition, a brief introduction of the multi-scale modeling in terms of the LLB equation is also included for the description of the micromagnetic exchange interactions.

Chapter 3 This chapter deals with the problem of parametrizing the atomistic exchange interaction. To parametrize the Heisenberg exchange Hamiltonian, we use a tight-binding approach. The materials are the magnetic transition metals. Our results are compared with more precise *ab-initio* methods. The Curie temperature is evaluated using the Langevin dynamics. Comparison between different methods and the experimental values is presented,

Chapter 4 In this chapter we present the evaluation of the macrosopic exchange stiffness A based on the long range atomistic exchange parameters (evaluated from different *ab-initio* approaches) for the case of Co *HCP* and Co *FCC* metals. We also establish the temperature dependence of $A(T)$ via its scaling relation with magnetisation. This is done both analitically and numerically via simulating domain wall thickness at different temperature. Analytical estimations based on the classical spectrum density method is presented and compared with the numerical evaluation.

Chapter 5 We numerically study the possibility of producing $TIMS$ in Tb_xCo_{1-x} disordered alloys using atomistic spin simulations. In this case, the exchange interaction is fitted to reproduce experimental data of T_{C} and T_{M} rare earth concentration x dependence, allowing us to study the influence of the existence and the position of the T_{M} relative to T_{room}. We investigate the occurrence of TIMS varying the Tb concentration, laser pulse fluency and its duration. This allows us to elucidate the conditions for the TIMS occurrence. We show that the deterministic TIMS occurs only for femtosecond laser pulse durations.

Chapter 6 In this chapter, $TIMS$ on ferromagnetic materials with a crystalline structure (Laves phase C15) instead of disordered alloys are studied using atomistic spin simulations. We use *ab-initio* exchange parametrizations. We show that in perfect Laves phases no deterministic TIMS occurs. We proceed with a material design letting the Laves phase C15 system to vary the exchange parameters and study the influence of the exchange values on the $TIMS$ occurrence.

2

Modelling methods for magnetisation dynamics

2.1 Multi-scale approach for magnetic parameters.

To simulate high temperature magnetisation dynamics processes, such as the all optical switching effect (AOS) [123, 145] or the heat assisted magnetic recording ($HAMR$) [91], standard micromagnetims is no longer useful because it does not take into account the variation of the magnetisation magnitude with temperature. Nevertheless, two different methods could be used instead of standard micromagnetism: atomistic spin dynamics and the novel micromagnetics based on the Landau-Lifshitz-Bloch equation.

On one hand, the material parameters needed for simulations with atomistic spin dynamics (ASD), such as the exchange coupling constants J_{ij} or the magnetic moments μ, could be extracted from *ab-initio* methods. Chapter 3, for example, deals with the parametrization of the exchange interaction, as well as with the calculation of the magnetic moments, for the magnetic transition metals, using the tight binding (TB) method [26, 128, 144]. Apart from *ab-initio* methods, the parameters needed for ASD can be also fitted from experimental results. For example, in chapter 5, we describe the methodology needed to extract the exchange coupling constants for a ferrimagnetic material ($TbCo$), from the experimental Curie temperature (T_{C}) and compensation point (T_{M}) using the mean-field approximation [15, 105, 106, 124, 149]. Thus, one advantage of ASD simulations is that the suitable parameters can be found. The main problem of atomistic spin simulations is that each spin is associated with one atom, therefore, from a computational point of view, there exist limitations to simulate big

systems.

On the other hand, Landau-Lifshitz-Bloch (LLB) micromagnetics considers macrospins instead of atomistic spins, therefore, LLB allows to calculate bigger systems than ASD. However, it is necessary to know the temperature dependence of the macrosopic material parameters in order to perform simulations. In section 2.3, a brief description of the LLB equation is given in order to show that the temperature dependent exchange stiffness and anisotropy are needed.

An illustration of the different approaches is presented in Fig. 2.1. The figure of the left shows the atomic spins considered in atomistic spin dynamics and the average magnetisation obtained from them. The simulated systems usually are smaller than $100nm^3$. The figure of the right shows that the average magnetisation obtained from atomistic simulations, are the macrospins considered in LLB micromagnetics. Simulations with LLB approach could consider systems with volumes up to $1\mu m^3$.

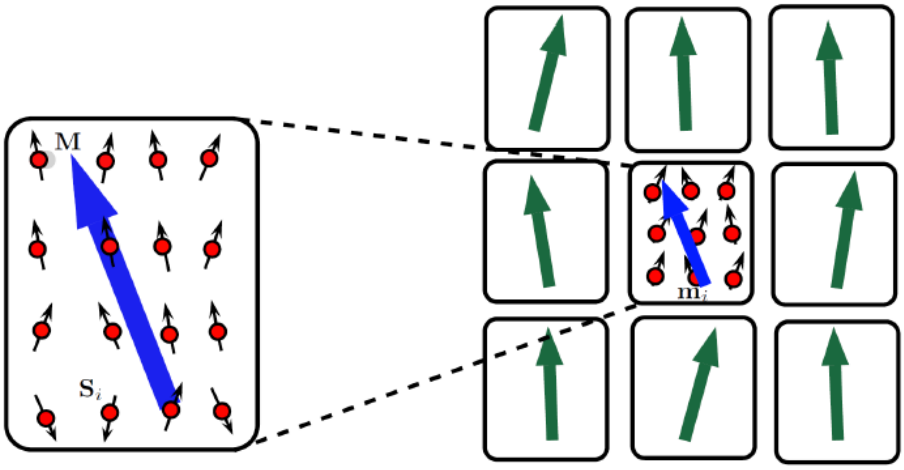

Figure 2.1: On the left, the localized spin configuration considered in ASD simulations. Red balls are the atoms of the atomic structure, their corresponding arrows are the spins associated with the atoms, the big blue arrow represents the average magnetisation obtained from fluctuating atomic spins. On the right, macro-spins considered in LLB simulations are presented.

The multi-scale apporach is a hieraechical method proposed by Kazantseva *et al* for $FePt$ to calculate the micromagnetic parameters as well as their temperature dependence, the parameters needed for LLB simulations, from an *ab-initio*

parametrization , [63, 74]. Firstly, using *ab-initio* methods, the hamiltonian used for atomistic spin simulations is parametrized. The *ab-initio* methods provide the information about the local magnetic moments (μ), the Heinseberg exchange parameters (J_{ij}) and the on-site magnetic anisotropy (d_z) [1]

Once the spin Hamiltonian is parametrized, the next step is obtaining the macroscopic material magnetic parameters temperature dependence, namely, the saturation magnetisation ($M(T)$), the exchange stiffness ($A(T)$) and the anisotropy ($K(T)$). The simulation of $M(T)$ is straightfoward using the ASD methods. For the case of the exchange stiffness, two different kind of atomistic spin simulations, which are described in Refs. [63, 74] could be used: from the domain walls and from the spin waves dispersion. For the case of the anisotropy, $K(T)$ could be calculated from domain walls simulations [74] or using the Constrained Monte-Carlo (CMC) method [14]. A schematic representation of the hierarchical multi-scale apporach is shown in Fig. 2.2.

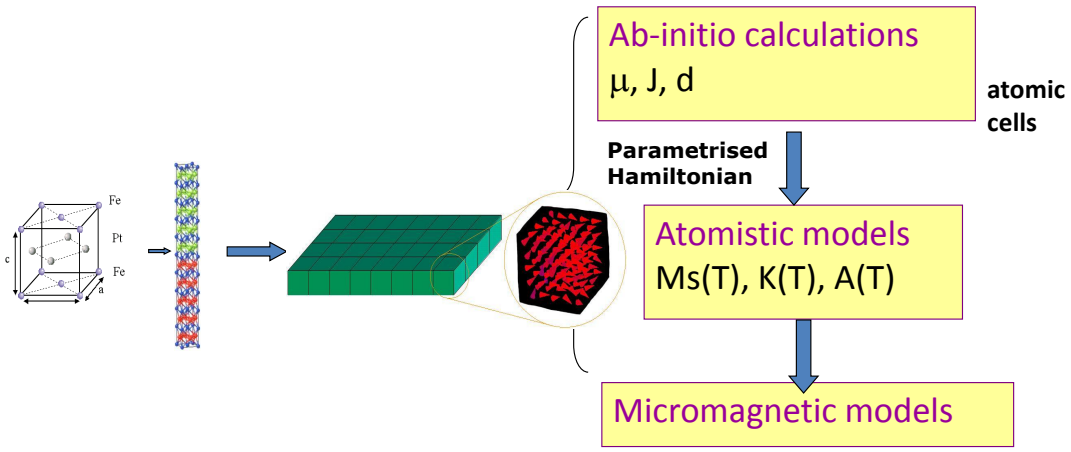

Figure 2.2: Schematic representation of the Multiscale approach, showing which parameters, obtained from *ab-initio* methods, are neeeded in ASD to obtain the corresponding micromagnetic parameters needed for the LLB simulations.

[1] Magnetic anisotropy values are often taken from measurements due to the difficulty to be calculated from *ab-initio* approaches.

2.2 Atomistic spin model

2.2.1 The atomistic spin Hamiltonian.

The magnetic moments of a material could be generated by localized or itinerant electrons, but in atomistic spin models, the magnetic moment is considered to be localized on the atoms. Even for the case of itinerant ferromagnets, for many purposes considering the magnetic moments localized on the atomic site is a good approximation [141]. The simplest Hamiltonian used to described a magnetic system in these models is

$$\mathbb{H} = -\sum_i \mu_i \vec{H} \cdot \vec{s}_i - \sum_i d_i s_{i,z}^2 - \frac{1}{2}\sum_{i,j} J_{ij} \vec{s}_i \cdot \vec{s}_j, \tag{2.1}$$

where $\vec{H}$ is the external magnetic field, μ_i is the magnetic moment associated with atom placed in the site i, $\vec{s}_i$ is a unit vector representing the direction of the magnetic moment placed on the site i, $s_{i,z}$ is its z component, d_i is the atomic uniaxial magnetic anisotropy and J_{ij} is the exchange energy between the atoms placed in sites i and j. The first term of the Hamiltonian represents the Zeeman energy, the second - the uniaxial anisotropy energy and the third is the exchange energy, which is described with the Heisenberg Hamiltonian.

The exchange interaction considered in Eq. (2.1) is the simplest one, the isotropic exchange, for which J_{ij} are scalars. It means that energy between two spins depends only on the angle they form. The exchange interaction can be generalized, in order to describe more complex magnetic systems, replacing the scalars J_{ij} by tensors $\mathbf{J_{ij}}$. Thus, the energy between two spins depends also on the direction they are pointing. In addition, the anisotropic exchange interactions, the two-ion anisotropy and the Dzyaloshinskii-Moriya interaction, are included in this tensor. A description of how the isotropic exchange, the two-ion anisotropy [114] and the Dzyaloshinskii-Moriya [169] interaction arise from the tensor $\mathbf{J_{ij}}$ is given in section 2.2.5.

The magnetic anisotropy considered in eq. (2.1) has been choosen to be uniaxial. Uniaxial magnetic anisotropy usually appears in materials with atomic structures for which one direction is elongated with respect to the others, such as HCP [43, 113] or $L1_0$ [74] phases. In experiments, AOS has been observed in thin films, which exhibit an uniaxial and often perpendicular anisotropy [10], therefore, in this thesis we use the uniaxial magnetic anisotropy to describe AOS processes in ASD simulations. For cubic anisotropy, this term must be substituted by

$$H_{ani}^{cub} = \frac{k_c}{2}\sum_i \left(S_{i,x}^4 + S_{i,y}^4 + S_{i,z}^4\right), \tag{2.2}$$

where k_c is the atomic cubic anistropy, and $S^4_{i,\nu}$, with $\nu = x, y, z$, are the components ν of the atomic spin placed in the atomic site i.

2.2.2 The time evolution of the atomic spins.

The time evolution of the normalized spins s_i is described with the phenomenological Landau-Lifshitz-Gilbert equation (LLG) [54] [1].

$$\dot{\vec{s}} = -\frac{\gamma}{1+\lambda^2}\left[\left(\vec{s}_i \times \vec{H}_{eff,i}\right) + \lambda\left(\vec{s}_i \times \left(\vec{s}_i \times \vec{H}_{eff,i}\right)\right)\right] \tag{2.3}$$

where $\vec{s}_i$ is a unit vector representing the direction of the magnetic moment placed on the site i, γ is the gyromagnetic factor, λ is the atomistic damping and $\vec{H}_{eff,i}$ is the effective magnetic field which interacts with the spin placed on the site i. The effective magnetic field $\vec{H}_{eff,i}$ is extracted from the derivate of the eq. (2.1),

$$\vec{H}_{eff,i} = -\frac{\partial \mathbb{H}}{\mu_i \partial \vec{s}_i}, \tag{2.4}$$

where μ_i is the atomic magnetic moment of the atom placed on the site i. The LLG equation, eq. (2.3), is composed of two different terms, describing two different physical effects of the magnetic moments interaction with a magnetic field. The first term, represents the precession of the atomic spins ($\vec{s}_i$) around the effective field interecting with them ($\vec{H}_{eff,i}$). The second term, represents a damping which at long time leads to the alignment of spin with the effective field ($\vec{H}_{eff,i}$). While the first term has a quantum mechanical origin, the second one is completely phenomenological, at least at the atomic level. This term represents the coupling to the bath parameter and contains the microsopic spin-flip probabilities due to some particular mechanism, such as the Elliott-Yafet scattering [33, 147].

2.2.3 Langevin dynamics

LLG equation, as it is written in 2.3, is stricktly speaking applicable to zero temperatures. Nevertheless, thermal effects can be included using the Langevin Dynamics approach, developed by Brown [27]. Langevin Dynamics introduces an extra random field for each atom site with a Gaussian distribution $\Gamma(t)$ in three dimensions with mean zero. For each time step the thermal field is described as

[1] To be noted that the pages from 1236 to 1272 from this reference in Phys. Rev. journal are missing although ref. [54] has hundreds of citations. However, the missing pages contain some abstracts which include ref. [54]. A complete description of this curious reference could be found in [2]

$$\vec{\zeta}_i = \vec{\Gamma}(t)\sqrt{\frac{2\lambda k_B T}{\gamma \mu_i \Delta t}} \tag{2.5}$$

where k_B is Boltzmann constant, T is the system temperature, γ is the gyromangetic ratio, μ_i is the magnetic moment magnitude of the atom placed in i and Δt is the time step. The thermal field (ζ_i), giving rise to Langevin Dynamics, is included in the LLG equation as follows,

$$\dot{\vec{s}} = -\frac{\gamma}{1+\lambda^2}\left(\left(\vec{s}_i \times \left(\vec{H}_{eff,i} + \vec{\zeta}_i\right)\right) + \lambda\left(\vec{s}_i \times \left(\vec{s}_i \times \left(\vec{H}_{eff,i} + \vec{\zeta}_i\right)\right)\right)\right) \tag{2.6}$$

Thus, Langevin Dynamics allows to simulate atomic systems with temperature different to zero, giving the possibility of calculating for example the magnetization versus temperature curve or more complex magnetic dynamics processes such as the ultrafast laser heating or heat assisted magnetic recording. For example, in the case of magnetization versus temperature simulations, the macroscopic magnetization for a given temperature (T) is calculated as an average on space and time of all the atomic spins considered in ASD simulations.

$$\vec{M}(T) = \left\langle \frac{1}{V}\sum_{i=1}^{N} \mu_i \vec{s}_i(t) \right\rangle_t \tag{2.7}$$

The ASD information presented here has been extracted, mainly, from the review written by Evans *et al* [46]. In this review, apart from describing the theoretical background of atomistic spin models, it is presented a public code, named "VAMPIRE", for which the atomistic spin model described before is implemented, allowing everyone interested on the investigation of mangetic processes in nanosystems to perform atomistic spin simulations. In this thesis, "VAMPIRE" has been used, as well as our home-made code.

2.2.4 Constrained MonteCarlo method.

The Langevin dynamics is useful to calculate both equilibrium states and dynamics of spins at any temperature. Nevertheless, apart from this method, equilibrium thermodynamics properties could be described using Monte-Carlo methods, in particular Metropolis algorithm [111].

Metropolis algorithm chooses randomly a spin S_i and change its direction to a new trial one S_i'. Then computing the energy difference between the old state and the new one $\left(\Delta E = E(S_i') - E(S_i)\right)$ we calculate the probability of acceptance of the trial movement

$$P = exp\left(-\frac{\Delta E}{k_B T}\right), \tag{2.8}$$

where k_B is the Boltmann constant and T is the temperature. If the the system has reduced its energy, the trial move is accepted unconditionally. Else, the trial move has a probability of being accepted P. This procedure is repeated N times where N is the number of atoms of the system. Each N trial moves are named as one Monte-Carlo step. Metropolis Monte Carlo is a useful algorithm to calculate the equilibrium properties such as the $M(T)$ curve. However, its does not contain the real dynamics since it does not describe the precession and there is not correspondence between the Monte Carlo step and the real time step in the general case.

Based on the Metropolis method, P. Asselin et al have developed the Constrained Monte Carlo method (CMC) [14] which allows us to calculate the temperature dependence of the magnetic anisotropy. In CMC method the trial moves act on two spins at the same time with the aim of remaining fixed the direction of the average magnetization $\hat{M}$. As in Metropolis method, a random spin S_i is selected to have a move trial S_i' but at the same time other random spin S_j is transformed to S_j' to compensated S_i move in order to keep fixed the $\hat{M}$ direction. Supposing that we have fixed the direction of $\hat{M}$ in the z axis, the acceptance of the trial move is given by

$$P = min\left[1, \left(\frac{M_z'}{M_z}\frac{|\hat{s_z}|}{|\hat{s_z'}|}\right) exp\left(\frac{-\Delta E}{k_B T}\right)\right] \tag{2.9}$$

As the direction of $\hat{M}$ is fixed, the system is not completely in equilibrium because there exits a torque $T = \left\langle -\sum_i s_i \times \partial \mathbb{H}/\partial s_i \right\rangle$. When the system reaches equilibrium, this torque is proportional to the uniaxial anisotropy constant,

$$K_u sin(2\theta) = T, \tag{2.10}$$

where θ is the angle between the anisotropy axis and the fixed direction of the magnetization in CMC. Therefore, calculating the torque T over the range $\theta \in (0, 2\pi)$, gives the possibility of fitting the results to eq (2.10) and extract the anisotropy value. As it can be done for all the temperatures range, the anisotropy temperature dependence can be found. In Ref. [14], where this method is presented, $K_u(T)$ is calculated for the uniaxial and cubic anisotropies, recovering the well-known Callen-Callen scaling laws with magnetization [29].

2.2.5 The generalized Heisenberg Hamiltonian

The most general term that describes the exchange energy of a magnetic system is written as

$$E_{exc} = -\frac{1}{2}\sum_{i\neq j}\vec{s}_i\mathbf{J_{ij}}\vec{s}_j, \tag{2.11}$$

where i and j represent the lattice sites, s_i and s_j are the spins vectors placed in the positions i and j respectively, and $\mathbf{J_{ij}}$ is a tensor 3×3 that represent the exchange energy between the spins s_i and s_j.

$$\mathbf{J_{ij}} = \begin{pmatrix} J_{ij}^{xx} & J_{ij}^{xy} & J_{ij}^{xz} \\ J_{ij}^{yx} & J_{ij}^{yy} & J_{ij}^{yz} \\ J_{ij}^{zx} & J_{ij}^{zy} & J_{ij}^{zz} \end{pmatrix} \tag{2.12}$$

J_{ij} tensor can be descomposed in three different terms that correspond to three physical exchange interactions.

$$\mathbf{J}_{ij} = J_{ij}\mathbf{I} + \mathbf{J}_{ij}^{S} + J\mathbf{J}_{ij}^{A} \tag{2.13}$$

The first term represents the isotropic exchange interaction and corresponds to the Heisenberg Hamiltonian used in this thesis for atomistic spin simulations.

$$J_{ij} = \frac{1}{3}\left(J_{ij}^{xx} + J_{ij}^{yy} + J_{ij}^{zz}\right) \tag{2.14}$$

The second term is the symetric part of the tensor and corresponds to the two-ion anisotropy interaction. This interaction is not taken into account in this thesis, however, it is necessary for more complex systems such FePt [74].

$$\mathbf{J}_{ij}^{S} = \begin{pmatrix} J_{ij}^{xx} - J_{ij} & \frac{J_{ij}^{xy}+J_{ij}^{yx}}{2} & \frac{J_{ij}^{xz}+J_{ij}^{zx}}{2} \\ \frac{J_{ij}^{xy}+J_{ij}^{yx}}{2} & J_{ij}^{yy} - J_{ij} & \frac{J_{ij}^{yz}+J_{ij}^{zy}}{2} \\ \frac{J_{ij}^{xz}+J_{ij}^{zx}}{2} & \frac{J_{ij}^{yz}+J_{ij}^{zy}}{2} & J_{ij}^{zz} - J_{ij} \end{pmatrix} \tag{2.15}$$

The third term is the antisymetric part of the tensor and is related to the Dzialoshinsky-Moriya interaction.

$$\mathbf{J}_{ij}^{A} = \begin{pmatrix} 0 & \frac{J_{ij}^{xy}-J_{ij}^{yx}}{2} & \frac{J_{ij}^{xz}-J_{ij}^{zx}}{2} \\ \frac{J_{ij}^{yx}-J_{ij}^{xy}}{2} & 0 & \frac{J_{ij}^{yz}-J_{ij}^{zy}}{2} \\ \frac{J_{ij}^{zx}-J_{ij}^{xz}}{2} & \frac{J_{ij}^{zy}-J_{ij}^{yz}}{2} & 0 \end{pmatrix}$$

(2.16)

2.3 The Landau Lifshitz Bloch equation.

The classical Landau Lifshitz Bloch (LLB) equation, was derived in 1997 by D.Garanin [51] for the averaged magnetisation using the ASD for atomistic spins, the Fokker-Planck equation and the mean-field approximation. The LLB equation then describes the time evolution of macrospins[1]. The main difference with standarad micromagnetics described by the LLG equation is that now the equation allows the variation of the magnitude of the magnetisation, leading to the possibility of modeling magnetic systems for which the temperature is changing, such as AOS or $HAMR$. Besides, LLB equation is useful for temperature over and below the Curie temperature (T_C), and this is important because in AOS the temperature of magnetic systems crosses T_C. Its validity has been checked by comparing the results with the experimental domain wall mobility in YIG crystals [75, 89] or comparing the relaxation times with atomistic simulations [36].

The LLB equation, without considering the stochastic term, is written as follows

$$\frac{dm_i}{dt} = -\gamma \left[m_i \times H^i_{eff} \right] + \frac{\gamma \alpha_{\parallel}}{m_i^2} \left(m_i \cdot H^i_{eff} \right) - \frac{\gamma \alpha_{\perp}}{m_i^2} \left[m_i \times \left[m_i \times H^i_{eff} \right] \right], \qquad (2.17)$$

where $m_i = M_i/Ms$ is the normalized magnetisation of the macrospin i, with Ms the magnetisation at saturation, γ is the gyromagnetic factor, $\alpha_{\parallel}$ and $\alpha_{\perp}$ are the longitudinal and tranverse relaxation parameters respectively and H^i_{eff} is the effective magnetic field interacting with the macrospin i. In eq. (2.17) there is an additional term with respect to the LLG equation (2.3). The first term in eq. (2.17) represents the precession of the macrospins around the effective magnetic field (H^i_{eff}). The second one, is the new which allows the macrospins to change their magnitude of the magnetisation during the simulations. The third term, represents the macroscopic damping leading to the aligment of the macrospins to the direction of the effective magnetic field. It is easy to check that the second term of the LLB equation allows to change the magnitude of the magnetisation, while in LLG equation (2.3) it does not change, multiplying in both equations dm_i/dt by m_i. Fig. 2.3 shows a schematic representation of the effect that each term of eq. 2.17 produces in the magnetisation time evolution.

[1] In fig. 2.1 the difference between macrospins and atomic spins is explained.

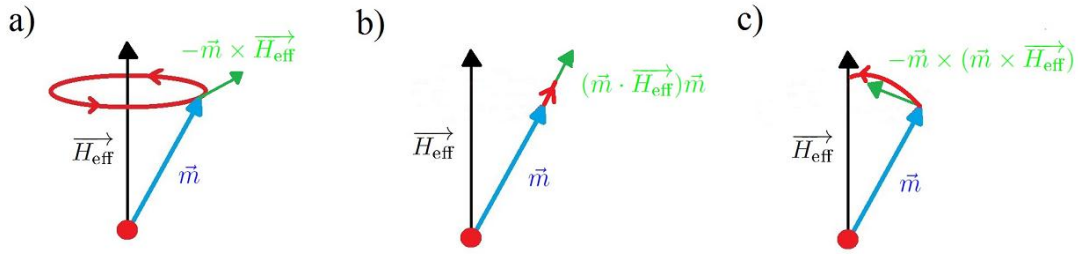

Figure 2.3: a), b) and c) represents the effect of the corresponding terms in eq. (2.17) in the magnetisation. Figure has been taken from [118].

The longitudinal and transversal relaxation parameters for each temperature have the following form

$$\alpha_{\parallel} = \lambda \frac{2T}{3T_C} \qquad \alpha_{\perp} = \lambda \cdot \begin{cases} \left[1 - \frac{T}{3T_c}\right] & T \leq T_C \\ \frac{2T}{3T_C} & T \geq T_C \end{cases} \tag{2.18}$$

where T is the temperature of the system, T_C is the Curie temperature and λ is coupling parameter to the bath (the atomistic damping parameter). Note that as LLB is valid for temperatures over and below T_C, the transversal relaxation parameter is also defined for both cases.

The effective fields in eq. (2.17) are also dependent on the temperature of the system

$$H^i_{eff} = H_{app} + H_{i,exc} + H_{i,ani} + \begin{cases} \frac{1}{2\tilde{\chi}_{\parallel}} \left(1 - \frac{m_i^2}{m_e^2(T)}\right) m_i & T \leq T_C \\ \frac{J_0}{\mu_{at}} \left(1 - \frac{T}{T_C} - \frac{3m_i^2}{5}\right) m_i & T \geq T_C \end{cases} \tag{2.19}$$

where H_{app} is an external applied magnetic field, $H_{i,exc}$ is the field arising from the exchange interaction, $H_{i,ani}$ corresponds to the field created by the uniaxial magnetic anisotropy. The last field, dependent on the temperature of the system with respect to the T_C, is a specific field in the LLB equation, which tries to take the magnetisation magnitude to its equilibrium value $m_e(T) = M_e(T)/M_S$ in the case of $T \leq T_C$. $\tilde{\chi}_{\parallel}$ is the longitudinal susceptibility, J_0 is the manitude of the atomistic exchange interaction (in the simple cubic lattice with nearest-neigbours interactions only $J_0 = 6J_{ij}$ and μ_{at} is the atomic magnetic moment.

The micromagnetic exchange field ($H_{i,exc}$) between two macrospins has the following form:

$$H_{i,exc} = \frac{2A_i(T)}{m_i^2 M_S}\nabla^2 m_i = \frac{2A_i(T)}{m_i^2 M_S l^2}\sum_j \left(m_j - m_i\right), \tag{2.20}$$

where j runs for all the macrospins which are neighbors of the macrospin i, l is the discretization length and finally it is shown the necessity of the exchange stiffness temperature dependence $A_i(T)$ for the LLB micromagnetic simulations.

The uniaxial anisotropy field $H_{i,ani}$ (for anisotropy pointing in z direction) is written as

$$H_{i,ani} = -\frac{2K(T)}{M^2}\left(m_{i,x}e_x + m_{i,y}e_y\right), \tag{2.21}$$

where $K(T)$ is the anisotropy constant, M is the magnetisation magnitude and e_i, with $i = x, y$, are unit vectors pointing in the x and y directions respectively.

2.4 Two-temperature model

Two-temperature model ($2TM$) was developed in 1957 by Kaganov [68, 134, 137] considering the rate-equations for the dynamics of electron and phonon (and may be spin) systems. It has been revived in ourdays with the aim of modeling the ultrafast thermal response of the electrons and the lattice (phonons) when the material is heated with ultrashort laser pulses. Many years later, a semiclassical two-temperature model was derived by Chen *et al* based on the Boltzmann transport equation which describes properly non-equilibrium electron effects [34].

The model presented in Ref. [34] allows the description of the electronic temperature dynamics of a metalic material. Including this model in both atomistic spin dynamics and LLB simulations allows to simulate the ultrafast magnetic response to the laser heating of a material . Although this model incorparates terms which represent the heat propagation in the sample, usually, the heat difussion on the sample is neglected because two main reasons: firstly, the experimental laser spot typically has around few μm of diameter. This area is bigger than the area able to be simulated in atomistic spin dynamics and similar to the LLB possibilities. Secondly, the typical samples used in experiments are thin films with a thickness less than the laser penetration depth. In this thesis the thermal diffusion is skipped from the two temperature model and it is considered that the system as whole is heated equally and the temperature is constant over the space. However, several works have been published considering the thermal diffusion such as Refs. [31, 52, 138].

Thus, neglecting thermal difussion, the equations of the two temperature model used to model the ultrafast laser heating are

$$\begin{aligned} C_e \frac{dT(t)_e}{dt} &= -G[T(t)_e - T(t)_{ph}] + P(t) \\ C_p \frac{dT(t)_p}{dt} &= G[T(t)_e - T(t)_{ph}] \\ P(t) &= (I_0 \cdot F) e^{-(t/\tau_p)^2} \end{aligned} \tag{2.22}$$

where $T_e(t)$ is the electronic temperature, $T_{ph}(t)$ is the phononic temperature, $C_e = \gamma T_e$ and C_p are the heat capacities for electrons and phonons and G is a coupling parameter between these systems. P(t) is assumed to be the pump laser energy received by the electronic system, I_0 describes the amount of laser energy absorbed by the sample, F is the laser fluence and τ_p describes the laser pulse duration. More specifically, the atomistic simulations use the value $(I_0 \cdot F)$ characterising the input energy (units of $J/(m^3 \cdot s)$), where F is the laser fluence while the experimental papers report the values in terms of F (units J/m^2).

Some of the parameters of the 2T model are known to some extend (such as the specific heats). Other parameters (specifically the absorbed energy) are usually fitted to reproduce experimental results. A brief description of the methods used to fit the two temperature model parameters are presented in [108, 118]. In this thesis, $2TM$ parameters are taken from literature.

The reliability of adding the two temperature model $2TM$ to Langevin dynamics for AOS modeling has been demonstrated in many published works for example Refs. [21, 123, 135]. Also adding two temperature model $2TM$ to LLB equations has been proved to give good results [108, 118].

3

The parametrization of the exchange interactions within a tight binding approach

3.1 Introduction

The Heisenberg Hamiltonian exchange parameters (J_{ij}) used in atomistic spin simulations (see section 2.2), are usually obtained phenomenologically from experimental properties within a mean-field approach (MFA) [149], see for example [46]. To be specific, the nearest neighbors exchange interactions for a ferromagnetic material are derived from the experimental Curie temperature (T_{C}). In the case of ferrimagnetic materials, the antiferromagnetic exchange between the two sublattices can be also obtained from the experimental compensation point (T_{M}).

On the one hand, the exchange parameters (J_{ij}) obtained via the mean-field approach can be used for methods such as atomistic spin simulations [46]. However, in case of using them for atomistic spin simulations, the exchange parameters must be corrected by a factor ϵ, that depends on the atomic structure, in order to reproduce the experimental results from which they are fitted [50]. In chapter 5, the fitting procedure of the exchange parameters from experimental data is widely discussed because in chapter 5, this method is used to parametrize the Heisenberg Hamiltonian for Tb_xCo_{1-x} disordered alloys.

On the other hand, it is well known that the exchange interaction is long-range, nevertheless, fitting exchange parameters from experimental data only provides first neighbors interactions. Although the magnitude of the exchange interactions decreases as the distance of the interacting spins increases, long-range exchange interactions must be taken into account in atomistic spin simulations because they could modify important features of a magnetic system, as the domain wall

width value [113], which may be strongly influenced by the long-range interaction (see chapter 4). In this regard, the long-range interactions can be calculated from *ab-initio* methods.

The first method to parametrize the Heisenberg Hamiltonian, using the local spin density approximation ($LSDA$) within the KKR-Green function, was developed by Liechtenstein *et al* in 1987 [100]. Some years later, in 2000, Katnelson *et al* generalized this method to include strongly correlated systems such as rare-earth [73]. Using these methods, the Heisenberg Hamiltonian has been parametrized for several magnetic materials, see for example the earlier works of Antropov *et al* in 1997 for Fe BCC and Ni FCC [12] or Katnelson *et al* for Fe BCC [73] and more recent works performed by Padja *et al* for Fe BCC, Ni FCC, Co FCC [126] or Turek *et al* for Co HCP, Gd HCP or Eu BCC [156].

In connection with the all optical switching effect (AOS), A. Secchi *et al*, derived in 2013 the formalism needed to parametrize the Heisenberg Hamiltonian for strong correlated systems, using a multiband Hubbard model within the tight binding approach (TB), when the system is out of equilibrium due to an external stimuli such as an ultrafast laser pulse [142]. As the magnetic system is in a non-equilibrium state, the exchange parameters (J_{ij}) are dependent on time ($J_{ij}(t)$), and they could explain the all optical switching effect (AOS) in terms of the time dependent exchange parameters.

In this chapter, with the final of calculating ($J_{ij}(t)$) for typical materials used in (AOS) experiments, such as $GdFeCo$, we start simplifying the problem, neglecting the non-equilibrium state due to the laser heating and considering only bulk magnetic transition metals: Fe BCC, Ni FCC, Co FCC and Co HCP. In addition, making use of the tight binding method [26, 128, 144], well-known properties of the electronic structure for these materials, such as the band structure, the density of states (DOS) or the magnetic moments, are calculated. However, the results obtained for J_{ij} in these materials are not as succesful as desired, thus, we stop at this point with the calculation of the time dependence of exchange parameters ($J_{ij}(t)$).

3.2 Theoretical background.

3.2.1 Tight-binding method.

The linear combination of atomic orbitals (LCAO) or tight-binding (TB) method was originally proposed by Bloch in 1928 [26] to solve the periodic potential in solids. The tight binding method consists in making linear combination of atomic orbitals with coefficents defined as plane waves $e^{i\vec{K}\cdot\vec{R}}$, where $\vec{k}$ is the Bloch wave

vector and $\vec{R}$ is the position of the atom. This method is a powerful tool to solve the single particle Schödinger equation at any point of the Brillouin zone (BZ) and shows the proper symetries of the energy bands. However, the main difficulty of LCAO is the necessity of numerically solve a great number of integrals. These integrals are the matrix elements of the Hamiltonian between different Bloch sums.

To avoid calculating such a great number of difficult integrals, in 1954 Slater and Koster (SK) proposed a modification of the LCAO method, which consists of fitting these integrals values, in order to reproduce the results of more accurate *ab-initio* methods, at high symetry points of the first Brillouin zone (BZ) [144]. Thus, once the integrals are fitted, the LCAO method allows to interpolate results of more accurate *ab-initio* calculations at any point of the BZ.

The SK method takes into account a set of atoms i at positions $\vec{b}_i$ inside a unit cell that is periodically replicated with lattice vectors $\vec{R}_m$. A set of atomic-like orbitals $\phi_{i\alpha}$ is associated to each atom i, where α is the atomic orbital considered. Due to the fact that orbitals placed in different atoms are in general non orthogonal, it is prefered to create a new set of atomic states $\psi_{i\alpha}$ that have the same symmetry properties as the original set as well as they are orthogonal. The new set of orthonormalized atomic states is called Löwdin functions [102].

$$\int \psi^*_{i\alpha}\left(\vec{r}-\vec{R}_m-\vec{b}_i\right)\psi^*_{j\beta}\left(\vec{r}-\vec{R}_n-\vec{b}_j\right)d^3r = \delta_{ij}\delta nm \tag{3.1}$$

Using Bloch's theorem, it is possible to rewrite Löwdin functions in the following form

$$\Psi_{ki\alpha}\left(\vec{r}\right) = N^{-1/2}\sum_n exp(i\vec{k}\cdot\vec{R}_n)\psi_{i\alpha}\left(\vec{r}-\vec{R}_n-\vec{b}_i\right), \tag{3.2}$$

where $\vec{k}$ is the Bloch wavevector and N is the total number of units cells of the system. Because of the periodicity is the same both for the Hamiltonian of the system and for the lattice, this basis diagonalizes the Hamiltonianin in blocks, with each block depending only in a single value of $\vec{k}$. In other words, the Hamiltonian will not have terms depending on two different values of the wave vector $H(\vec{k},\vec{k}')$. For a given value of the wave vector $\vec{k}$ the matrix elements of the Hamiltonian can be expresed as

$$H_{i\alpha,j\beta}\left(\vec{k}\right) = \frac{1}{N}\sum_n exp\left(i\vec{k}\cdot\left(\vec{R}_n-\vec{R}_m\right)\right)\int \psi^*_{i\alpha}\left(\vec{r}-\vec{R}_m-\vec{b}_i\right)H\psi^*_{j\beta}\left(\vec{r}-\vec{R}_n-\vec{b}_j\right)d^3r \tag{3.3}$$

But using the translation symetry of the lattice it is possible to remove one of the sums simplifying the Hamiltonian matrix elements.

$$H_{i\alpha,j\beta}\left(\vec{k}\right) = \sum_n exp\left(i\vec{k}\cdot\vec{R}_n\right)\int \psi^*_{i\alpha}\left(\vec{r}-\vec{R}_m-\vec{b}_i\right)H\psi^*_{j\beta}\left(\vec{r}-\vec{R}_n-\vec{b}_j\right)d^3r \quad (3.4)$$

The Hamiltonian includes a single-particle potential, which is a sum of potentials placed in each atom i and vanishes at some distance away from the atom.

$$V\left(\vec{r}\right) = \sum_{nk} V_i\left(\vec{r}-\vec{R}_n-\vec{b}_i\right) \quad (3.5)$$

Taking into account the site in which the wavefunctions and the potential are placed, is possible to distinguish between different integral types:

1. The first case occurs when the wavefuntions and the potential are placed in the same site. This kind of integrals are called on site.

2. The second case is when the potential and one of the wavefunctions coincide in the same place. These integrals are called two-center integrals.

3. The third case is when both wavefunctions and the potential term do not coincide in any site. These integrals are called three-center integrals.

4. The fourth case is when the wavefunctions have the same center but the Hamiltonian does not. They haven't been included in the original SK paper and its formalism was developed later [37, 110].

With the aim of simplifying the problem, we will work with the two-center approximation. This approximation neglects integrals types 3 and 4 in order to reduce the number of constants needed to construct the tight binding Hamiltonian of a solid. Integral types 3 and 4 can be neglected because, although their values are not negligible, they are smaller than the two center integrals. In the following the two center integrals are named as hoppings.

As we are using Löwdin functions, which have the same symmetry with respect to the crystal than the atomic orbitals, it is possible to considerer that the decomposition of an orbital, with orbital quantum number l, into its component with respect to the axis σ, π and δ is a good approximation, where σ, π and δ are the differents types of bonding for s, p and d atomic orbitals. In fig. 3.1 the different possibilities of bonding between s and p orbitals are shown. Therefore, the integrals in eq (3.4) will have non-vanishing contributions if the component with respect to the axis σ, π and δ of ψ_n and ψ_m coincide, reducing again the number of integrals needed to construst the tight binding Hamiltonian.

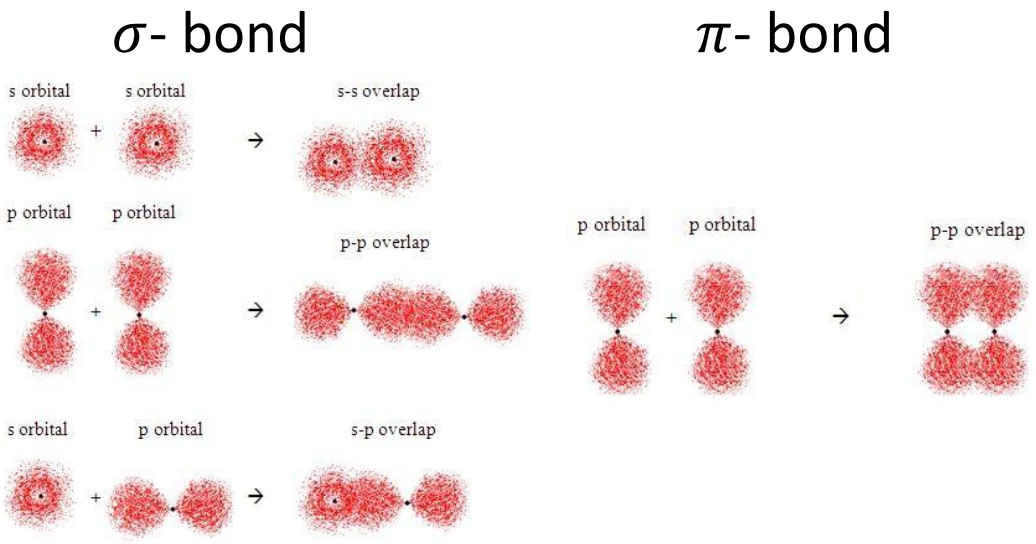

Figure 3.1: Different types of bonding for orbitals s and p. The figure has been extracted from [3].

To calculate the integrals in eq. 3.4, the contribution of the product of atomic orbitals placed in $\vec{R}_n$ and $\vec{R}_m$ is needed. Defining l,m,n as the direction cosines of the vector $\vec{R}_n - \vec{R}_m$, and using the cubic harmonics it is possible to derive the SK energy table in terms of the two-center integrals. Table 3.1 shows some examples of the two-center integrals for orbitals s, p and d extracted from the original Slater-Koster table [144]. The two center integrals $ss\sigma$, $sp\sigma$, $pp\pi$, etc are constants used to fit results from more accurate calculation.

$E_{s,s}$	$(ss\sigma)$
$E_{s,x}$	$l\,(sp\sigma)$
$E_{x,x}$	$l^2\,(pp\sigma) + (1 - l^2)\,(pp\pi)$
$E_{s,xy}$	$\sqrt{3}lm\,(sd\sigma)$
E_{s,x^2-y^2y}	$\frac{1}{2}\sqrt{3}\,(l^2 - m^2)\,(sd\sigma)$
E_{y,x^2-y^2y}	$\frac{1}{2}\sqrt{3}m\,(l^2 - m^2)\,(pd\sigma) - m\,(1 + l^2 - m^2)\,(pd\pi)$
$E_{z,3z^2-r^2}$	$n\left[n^2 - \frac{1}{2}\,(l^2 + m^2)\right](pd\sigma) - \sqrt{3}n\,(l^2 + m^2)\,(pd\pi)$

Table 3.1: Some examples of energy integrals in terms of two-center integrals extracted from the original Slater-Koster table parameters [144].

These constants have been fitted for several materials, among them, the magnetic transition metals: Fe, Co and Ni. These parameters are published in [127]

and we will use these parametrization for our calculations. The method used to fit them as well as an extensive description of the tight binding method could be found in [128].

3.2.2 The Green function

Given a Hamiltonian $H(\vec{k})$, its corresponding Green function for a given energy E is defined as

$$G(z,\vec{k}) = \lim_{\epsilon\to 0}(z - H(\vec{k}))^{-1} \tag{3.6}$$

where k is the Bloch wave vector, $z \in \mathbb{C}$ is a complex number with $z = E + \epsilon i$, where E is the energy of system and ϵ is it complex part.

Green functions can be written is terms of the eigenvectors $|\psi(\vec{k})_{\alpha S}>$ and eigenvalues $a(\vec{k})_{\alpha S}$ of the Hamiltonian $H(k)$.

$$G(z,\vec{k}) = \lim_{\epsilon\to 0}\frac{|\psi(\vec{k})_{\alpha S}><\psi(\vec{k})_{\alpha S}|^*}{a(\vec{k})_{\alpha S} - z} = \lim_{\epsilon\to 0}\frac{|\psi(\vec{k})_{\alpha S}><\psi(\vec{k})_{\alpha S}|^*}{a(\vec{k})_{\alpha S} - E + \epsilon i} \tag{3.7}$$

Where α represents the atomic orbital and S the spin.

One the advantages of calculating Green functions instead of the hamiltonian diagonalization is that the density of states of a system can be easily calculated in terms of its trace. For example, the total density of states is given by

$$n(E) = \int dk^3 \left(-\frac{1}{\pi} Im\left(Tr_{\alpha S}\left(G(z,\vec{k}_{\alpha S,\alpha' S'}\right)\right)\right) \tag{3.8}$$

Where $n(E)$ is the total density if states, $Tr_{\alpha S}$ is the trace of the Green function over its atomic orbitals α and spin component S. In addition, the spin or orbital resolved density of states is the following

$$n(E)_{\alpha S} = \int dk^3 \left(-\frac{1}{\pi} Im\left(G(z,\vec{k})_{\alpha S,\alpha S}\right)\right) \tag{3.9}$$

The Green function $G(z,\vec{k})$ is defined in the reciprocal space $(\vec{k})$, however, by performing a Fourier transform they can be calculated in the real space $(\vec{r}_{ij})$.

$$G(z,\vec{r}_{ij}) = \int_{BZ} dk^3 G(z,\vec{k}) e^{-i\vec{k}\cdot\vec{r}_{ij}} \tag{3.10}$$

Where the integral in the reciprocal space must be performed over all the first Brillouin zone (BZ) and $\vec{r}_{ij}$ is the vector for which we calculate $G(z,\vec{r}_{ij})$.

3.2.3 The Heisenberg Hamiltonian parametrization with a tight-binding scheme

From the Green functions it is possible to calculate the exchange coupling constants, providing a mapping to a Heisenberg model. Firstly, it is important to stress that the Heisenberg Hamiltonian assumed in the calculations is the following

$$H = -\frac{1}{2}\sum_{i\neq j} J_{ij}\vec{s}_i\vec{s}_j, \tag{3.11}$$

where $\vec{s}_i$ are unit vectors that represent the atomic spins placed at site i and J_{ij} are the exchange coupling constants between the local moments at site i and j, with absolute value of the moments included in the constants J_{ij}. The Hamiltonian expressed in eq. 3.11 is the commonly used in atomistic spin simulations, see [46], however, there are equivalent definitions as $H = -\sum_{i\neq j} J'_{ij}\vec{s}_i\vec{s}_j$, see [100, 126]. Consequently, the relation between both exchange parameters is

$$J_{ij} = 2J'_{ij}. \tag{3.12}$$

The calculation of the J_{ij} requires several approximations. The adiabatic approximation, assuming that the time scale of fluctuations of the magnetic moment is larger than that for electron hopping and the magmetic force theorem. The change in the orientation of the moment does not produce significant changes in the value of the magnetic moment.

The ground state in a ferromagnet is given by

$$E_0 = -\frac{1}{2}\sum_{i\neq j} J_{ij}, \tag{3.13}$$

where we have assumed that spins $\vec{s}_i$ from eq. (3.11) are parallel, pointing to the direction of a vector $\vec{s}_0$.

The energy difference of a single site infitesimal rotation of the spin $\vec{s}_i$ is given by

$$\delta E(\vec{s}_i) = E(\vec{s}_i) - E_0 = (1 - \vec{s}_i\vec{s}_k)\sum_{k(\neq i)} J_{ik}. \tag{3.14}$$

We stress that vectors $\vec{s}_k$ are pointing in the $\vec{s}_0$ direction.

The energy difference of a two-site excitation is

$$\delta E(\vec{s}_i,\vec{s}_j) = -\left(\vec{s}_i - \vec{s}_0\right)\left(\vec{s}_j - \vec{s}_0\right)J_{ij} + \delta E(\vec{s}_i) + \delta E(\vec{s}_j) = \delta\vec{s}_i\delta\vec{s}_j J_{ij} + \delta E(\vec{s}_i) + \delta E(\vec{s}_j) \tag{3.15}$$

Thus, the interaction energy between two spins can be written as the energy difference of varying both spins at the same time minus varying both separately.

$$E_{ij}^{int} = \delta E(\vec{s}_i, \vec{s}_j) - \delta E(\vec{s}_i) - \delta E(\vec{s}_j) = J_{ij}\delta\vec{s}_i\delta\vec{s}_j \tag{3.16}$$

Using the magnetic force theorem [62, 125], the energy variation can be exprесed in terms of the Green function of the system.

$$E_{ij}^{int} = -\frac{1}{\pi}\int_{\infty}^{\varepsilon_F} dEf(E)Im\delta^* TrlnG(E) \tag{3.17}$$

Where $f(\varepsilon)$ and ε_F are the well known Fermi distribution and Fermi energy respectively. $G(E)$ is the Green operator of the unperturbed system, with $z \in \mathbb{C}$ and $z = E + \epsilon i$, where E is the energy of system and ϵ is the complex part of the energy. δ^* means the variation without considering self-consistent change on the system. For a given hamiltonian H the corresponding green function $G(E)$ is defined in eq. (3.6).

Considering the same variation on spins in eq. (3.17) as considered in eq. (3.16),

$$\begin{aligned} J_{ij}\delta\vec{s}_i\delta\vec{s}_j &= \delta E(\vec{s}_i, \vec{s}_j) - \delta E(\vec{s}_i) - \delta E(\vec{s}_j) \\ &= -\frac{1}{\pi}\int_{\infty}^{\varepsilon_F} d\varepsilon f(\varepsilon) ImTr\left(\delta^{ij} lnG(z) - \delta^i lnG(z) - \delta^j lnG(z)\right), \end{aligned} \tag{3.18}$$

Following the derivation of ref. [100] the relation between the exchange parameters J_{ij} of the Heisenberg Hamiltonian and the Green functions corresponding to the Hamiltonian of the system is obtained [121]. The final expression used the calculation of the exchange parameters using the tight binding method is the following.

$$J_{il,jl'} = \frac{1}{2\pi}\int_{-\infty}^{\varepsilon_F} f(\varepsilon) Tr_\alpha \left[\left(\left(H_{ii,l}^{\uparrow} - H_{ii,l'}^{\downarrow}\right) G^{\uparrow}(z, \vec{r}_{ij}) \left(H_{jj,l'}^{\uparrow} - H_{jj,l'}^{\downarrow}\right) G^{\downarrow}(z, \vec{r}_{ji})\right] d\varepsilon \tag{3.19}$$

where J_{ij} is the exchange interaction between the spins i and j, $f(\varepsilon)$ is the fermi distribution, H_{ii} and H_{jj} are the onsite interactions of the Hamiltonian in a tight binding scheme (see subsection 3.2.1), $G^{\uparrow}(z, \vec{r}_{ij})$, Tr_α is the trace on atomic orbitals, l and l' are the corresponding atomic orbitals and $G^{\downarrow}(z, \vec{r}_{ji})$ are the spin up and down one-particle Green functions in real space respectively with $\vec{r}_{ij}$ being the vector that separates the spins i and j.

3.3 Modeling results

3.3.1 Atomic structures

We calculate the exchange interactions J_{ij} for the magnetic Fe BCC, Ni FCC, Co FCC and Co HCP, where BCC, FCC and HCP mean body centered cubic, face and hexagonal close packed atomic structures respectively, see [13].

BCC and FCC atomic structures are Bravais lattice. Thus, both lattices can be generated from linear combinations of the lattice vectors $\vec{R}_1, \vec{R}_2, \vec{R}_3$, that corresponds to each Bravais lattice, using as coefficients only integer numbers [13]. Apart from these structures, there exists others like the simple cubic (SC) or the hexagonal (HEX) atomic structure which are also Bravais lattices, nevertheless, the HCP atomic structure is not. The HCP atomic structure is composed of two hexagonal atomic structures interpenetrated. In other words, HCP atomic structure is generated using the hexagonal lattice vectors $\vec{R}_1, \vec{R}_2, \vec{R}_3$, but for each unit cell there are two atoms separated by a vector B, which is the basis vector.

Given a Bravais lattice, i.e, BCC or FCC atomic structures, with primitive vectors $\vec{R}_1, \vec{R}_2, \vec{R}_3$, the corresponding vectors in the reciprocal space that defines the first Brillouin zone, $\vec{K}_1, \vec{K}_2, \vec{K}_3$ are calculated using the equation $\vec{R}_i \cdot \vec{K}_j = 2\pi\delta_{ij}$ [13]. In contrast, because of the HCP atomic structure is not a Bravais lattice[1] its BZ is defined as the BZ of the underlying Bravais lattice, in this case is the BZ of the hexagonal lattice [13]. Fig. 3.2 shows the Brillouin zone for the different atomic structures taken into account.

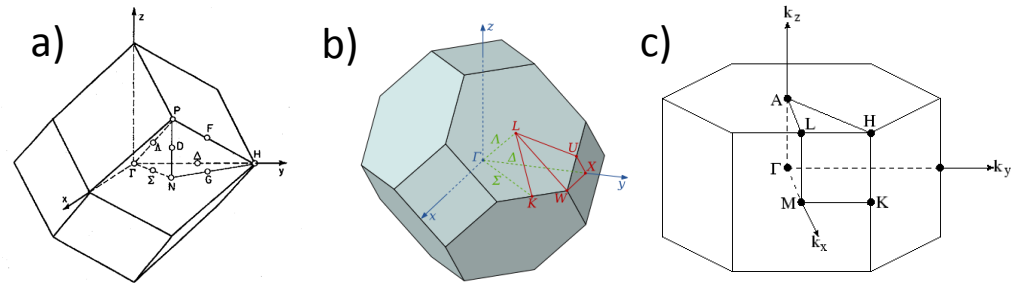

Figure 3.2: a), b) and c) represent the corresponding first Brillouin zone of the BCC, FCC and HCP atomic structures, showing their high symetry points.

[1] It is a hexagonal lattice with two atoms per basis.

3.3.2 The electronic band structure

Firstly, we calculate the ground state properties and electronic structure for Fe BCC, Ni FCC, Co FCC and Co HCP within the tight binding approach. The tight binding hamiltonian $H(\vec{k})$ has been constructed following the Slater Koster approach, using the parametrizations of Papaconstantopoulos's book [127] for all the materials considered in this chapter.

In Papaconstantopoulos's book [127] it is possible to find different parametrizations for the same material like the orthogonal two center approximation, the non-orthogonal or the three center approximation. Among the different parametrizations. the orthogonal two center approximation, which is described at the end of the subchapter 3.2.1, has been selected for simplicity. It must be pointed out that for Co FCC, we have had to introduce an spin polarization on the onsite parameters [1], extracted from [130], because the parametrization published in [127] are for the paramagnetic case.

Fe, Co, and Ni have electronic configurations $[Ar]3d^64s^2$, $[Ar]3d^74s^2$, $[Ar]3d^84s^2$ respectively, therefore, in all our calculations, only $4s$, $4p$ and $3d$ atomic orbitals are considered in the tight binding Hamiltonian.

To construct the tight binding hamiltonian matrix elements written in eq. (3.4), firstly, it is needed to substitute the integral on the right by the corresponding Slater-Koster term of Table 3.1. Secondly, the tight binding parameters obtained from [127] are introduced in the corresponding Slater-Koster term. Finally, the sum over the neighbors of the atomic structure must be performed.

Once the tight binding hamiltonian $H(\vec{k})$ has been constructed for one $\vec{k}$ vector, eq. (3.4), it can be diagonalized in order to obtain its eigenvalues $a_{\alpha S}(\vec{k})$, where α represents the atomic otrbital and S represents the spin index. The band structure of any material is defined as the eigenvalues of the corresponding hamiltonian for the high symetry directions of the first Brillouin zone. Fig. 3.3 shows the band structure for the materials considered in this chapter.

From fig. 3.3 a *sd* bonding as well as a concentration of d-bands around the Fermi level is observed for all the materials studied in this chapter. For the cubic structures, BCC and FCC, it is observed the degeneracy of d-orbitals into T_2G and eg orbitals at γ. For the case of the HCP, it is shown that the corresponding plot has the double of bands than for BCC or FCC. This difference is due to HCP atomic structure has two atoms per unit cell.

The band structure for the different materials depicted on fig. 3.3 agrees perfectly with those published in [127], which are calculated for a different set of parameters, instead of using the orthogonal two center parameters.

[1] The onsite parameters are defined in subchapter 3.2.1

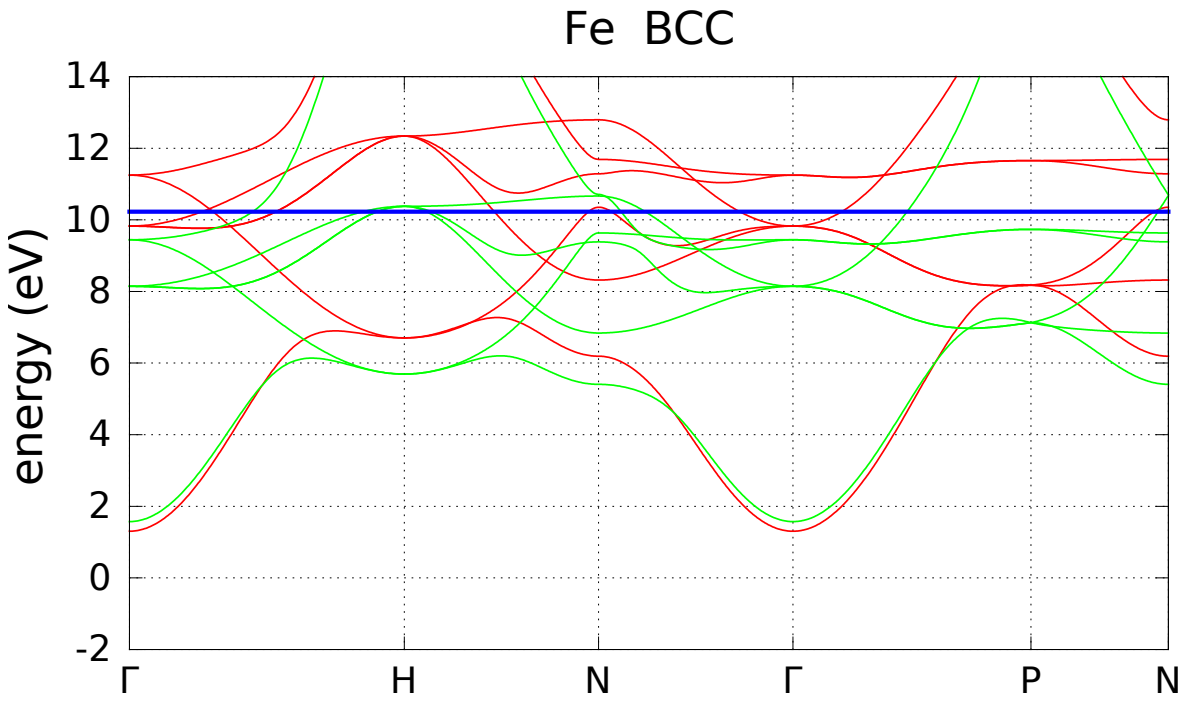
Fe BCC
energy (eV)
14
12
10
8
6
4
2
0
-2
Γ
H
N
Γ
P
N

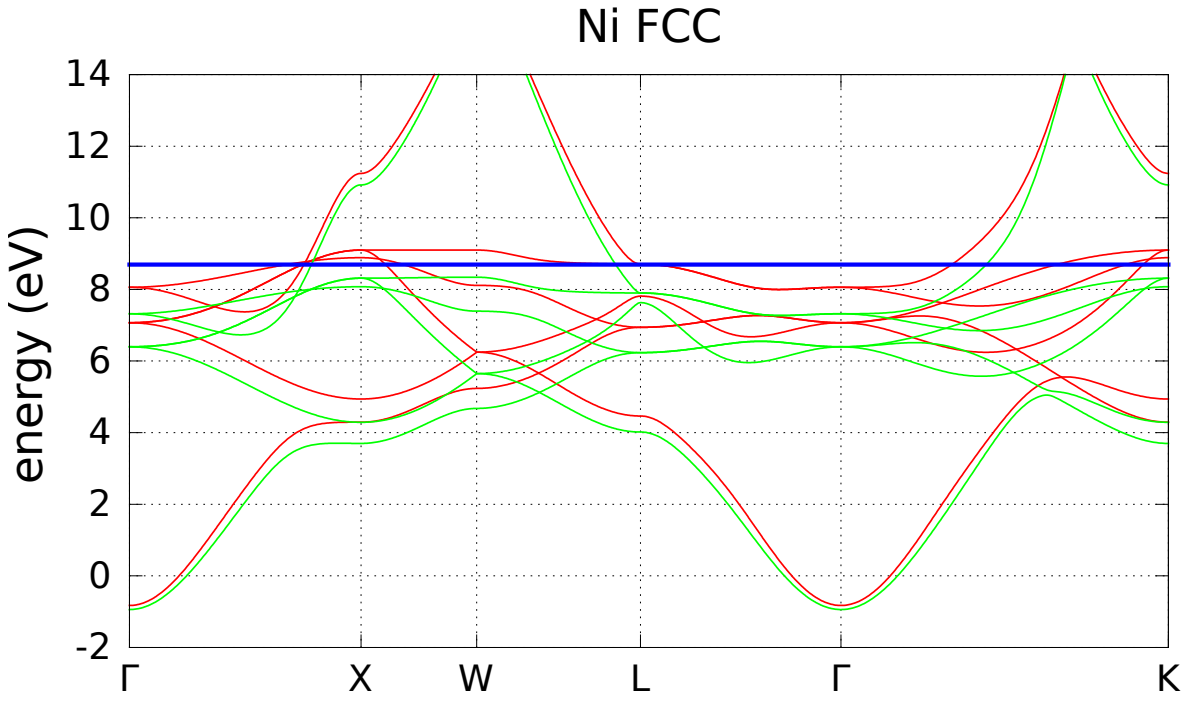
Ni FCC
energy (eV)
14
12
10
8
6
4
2
0
-2
Γ
X
W
L
Γ
K

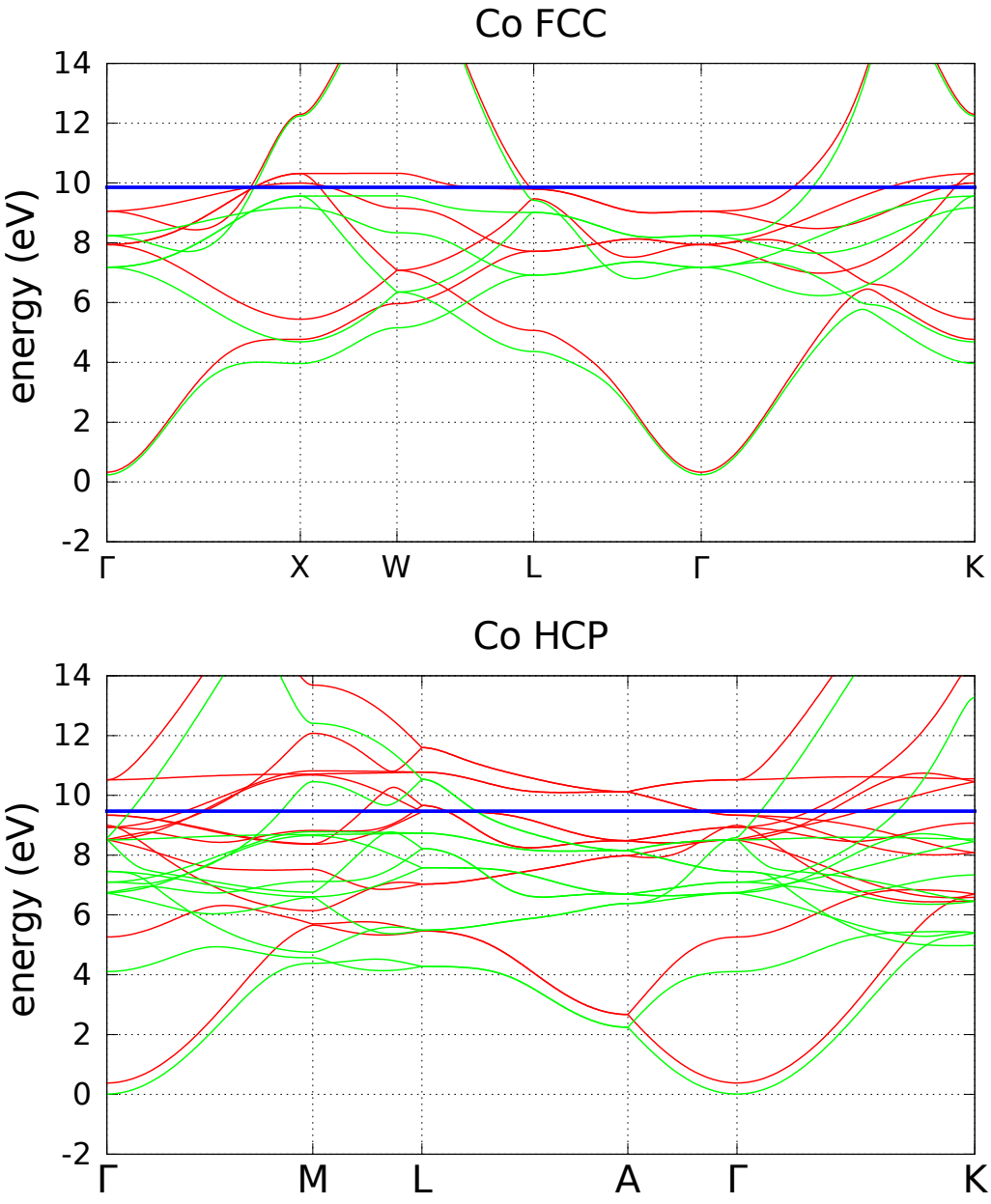

Figure 3.3: a), b), c) and d) represents the calculated spin polarized band structure for Fe BCC, Ni FCC, Co FCC and Co HCP respectively using the tight-binding method. Red and green lines represent the spin down and up respectively. Blue line represents the corresponding Fermi energy to each material. X-axis tics represent the high symetry points of the corresponding BZ of each lattice.

3.3.3 The density of states

Orbital and spin resolved density of states $n(E)_{\alpha S}$ can be easily calculated in terms of the green functions $G(z,\vec{k})$, which are obtained from the Hamiltonian $H(\vec{k})$ of the system by using eq. (3.6). The density of states $n(E)_{\alpha S}$ for each atomic orbital α as well as for each spin S is obtained from the diagonal values of the Green function $G_{\alpha S,\alpha S}(z,\vec{k})$, as it is described in eq. (3.8). The spin resolved density of states $n(E)_S$ is obtained from $Tr_\alpha G_{\alpha S,\alpha S}(z,\vec{k})$ and the total density of states $n(E)$ comes from $Tr_{\alpha S}G_{\alpha S,\alpha S}(z,\vec{k})$, where Tr_α is the trace of the Green function in the index α.

The integral in the reciprocal space written in eq. (3.8) is performed over all the first Brillouin zone of the corresponding atomic structure, however, it is not really needed because to calculate the density of states is enough to integrate over the irreducible zone of the BZ. The real reason to integrate over all the BZ is to calculate in the same loop of our code the green function in real space $G(z,\vec{r}_{ij})$, needed in the exchange parameters equation (eq. 3.19), which must be calculated in this way.

By integrating the density of states in energies we determine the Fermi level ε_F for each system. The Fermi level is defined as, the energy for which the number of free electrons, that the material has on its electronic configuration, is equal to value of the integral in energies of the total density of states. To be specific, the electronic configurations for Fe, Co and Ni are $[Ar]3d^64s^2$, $[Ar]3d^74s^2$, $[Ar]3d^84s^2$ respectively, therefore, the Fermi level for these materials is the energy for which the integral $N(\varepsilon_F) = \int_\infty^{\varepsilon_F} n(E)dE$ is equal to 8,9 and 10 respectively.

In our calculations, we have used $\epsilon = 10meV$ as the imaginary part of the complex energy z, the variable used in the green function $G(z,\vec{k})$. This value has been chosen because we are sweeping in energies E with a precision of $\Delta E = 5meV$. The integral over the first Brillouin zone of the DOS has been performed using 10^6 different values of $\vec{k}$ homogeneously distributed. In fig. 3.4 it is represented the density of states resolved in spins for the different materials considered in this chapter as well as the integral of the normalized density of states $(N(E))$ [1].

The mangetic moment is defined, in units of the Bohr's magneton μ_B, as the difference of the number of electrons with spin up with the number of electrons with spin down, $\mu = N(\varepsilon_F)^\uparrow - N(\varepsilon_F)^\downarrow$, both evaluated at Fermi level ε_F. The calculated magnetic moments for each material are presented in Table 3.2, together with different values found in the literature, showing a good agreement.

[1] We are considering orbitals $4s$ $4p$ $3d$ in our tight binding Hamiltonian, therefore, the maximun number of electrons that $N(E)$ could exhibit is $n = 18$ so $N(E)$ is normalized by n.

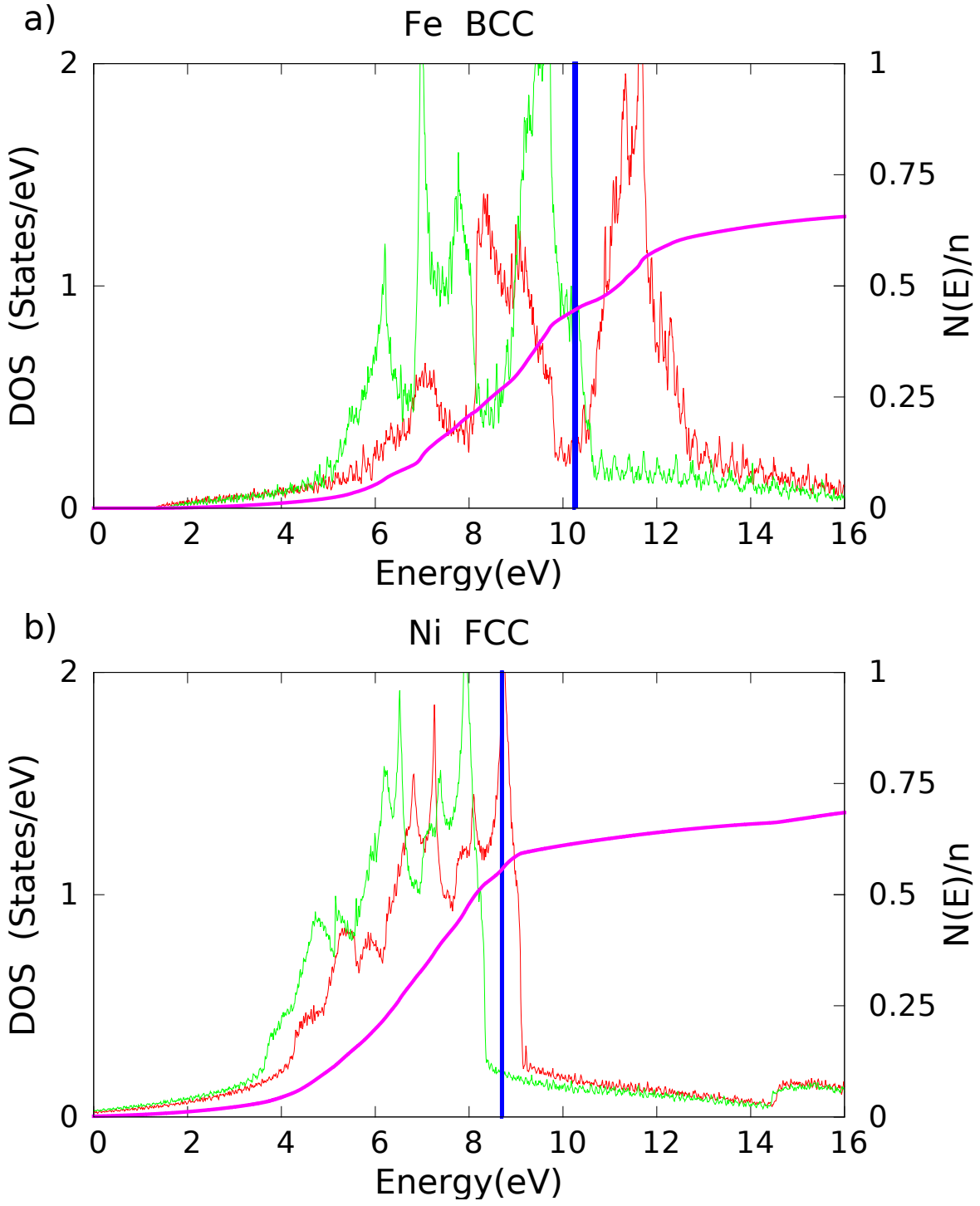
a)
Fe BCC
DOS (States/eV)
N(E)/n
Energy(eV)
b)
Ni FCC
DOS (States/eV)
N(E)/n
Energy(eV)

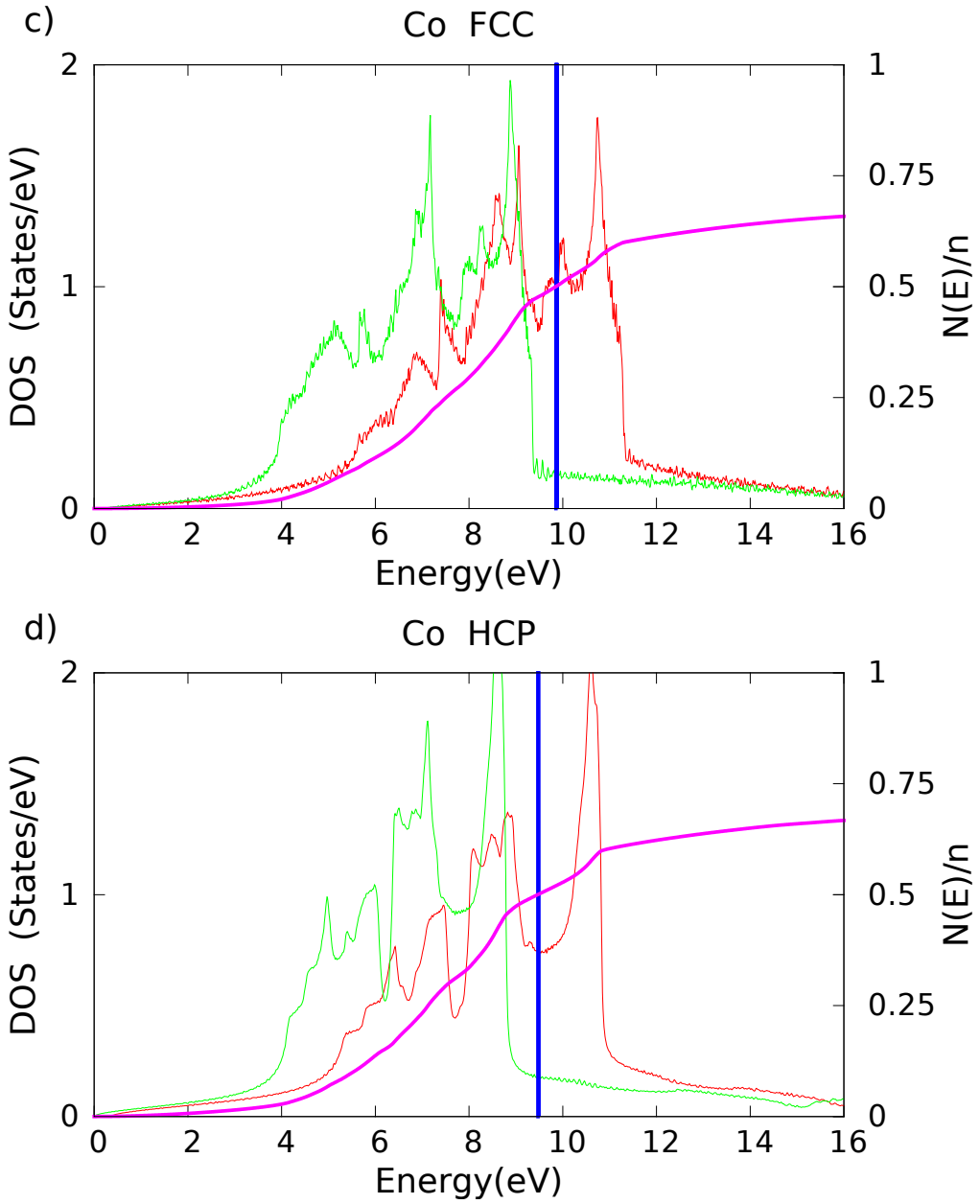

Figure 3.4: Calculated spin polarized DOS of the transition metals using the tight-binding method. Red and green lines represent the spin down and up respectively. Blue line represents the corresponding Fermi energy to each material. Pink curve represent the integral of the DOS ($N(E)$) normalized by $n = 18$ which is the maximun number of electrons that $N(E)$ could reach.

$\mu(\mu_B)$		
Atomic structure	Tight-binding	Experimental
Fe (BCC)	2.11	2.216 [149, 165]
Ni (FCC)	0.69	0.616 [149, 165]
Co (FCC)	1.51	1.75 [40, 97]
Co (HCP)	1.61	1.715 [149, 165]

Table 3.2: Calculated magnetic moments with the tight-binding method together with experimental values.

The density of states obtained from Green functions in a tight binding scheme show a good agreement with the previosuly calculated in [127], see other examples in [13]. In the case of the magnetic moments, we also see that the values we have obtained are also in good agreement with the other values, extracted from literature, presented in Table 3.2. Thus, we conclude that the Green functions in the reciprocal space are well calculated.

3.3.4 Exchange parameters.

Once the Green functions in the reciprocal space $G(z,\vec{k})$ have been calculated, obtaining from them the corresponding Green functions in real space $G(z,\vec{r}_{ij})$ for a given vector $\vec{r}_{ij}$ can be done easily by performing a Fourier transform, as it written in eq. (3.7). We stress again that to do a Fourier transform of the Green function it is needed to integrate over all the BZ. To be noted that, the vector $\vec{r}_{ij}$ for which the Fourier transform in done, corresponds to the vector that separates the two spins for which the exchange interaction J_{ij} is going to be calculated. Besides, if we want to calculate the exchange interaction for a given vector $\vec{r}_{ij}$ it must be taken into account that, for one spin, the Fourier transform is done for $\vec{r}_{ij}$, and for the other spin, for $-\vec{r}_{ij}$, see eq. (3.19). Both spins can be treated separately because we have not considered the spin-orbit coupling in the tight binding Hamiltonian, therefore, the Fourier transform for each spin can be done independently.

The onsite energy terms of the tight binding Hamiltonian, $H_{\uparrow ii}$ and $H_{\downarrow ii}$, appearing in eq. (3.19) have already been calculated in the tight binding Hamiltonian $H(\vec{k})$ construction. It corresponds to the term for which both wavefuntions and the potential of the Hamiltonian are placed in the same atom, see subsection 3.2.1. Thus, onsite energy term is obtained considering that one atom interacts only with itself. The way in which we have calculated this term is the following: we started constructing the Hamiltonian $H(\vec{k})$ with the onsite energy term, then

we saved this result for the calculus of the exchange parameters, after this, we finished constructing $H(\vec{k})$ by adding the hopping parameters. Another possibility, computationally more expensive, is to do the Fourier transform of $H(\vec{k})$ for $\vec{r}_{ij} = 0$. The onsite energy term is diagonal on spins and on angular moments for the structures considered in this chapter, except for HCP structure because it exists an onsite $p - d$ onsite term, see [112, 127].

Thus, using the Green functions in real space and the onsite energies, the exchange parameters J_{ij} can be calculated by integrating eq. (3.19) in energies up to the Fermi level. Fig 3.5 shows the calculated exchange parameters using the tight binding approach, for Fe BCC, Ni FCC, Co FCC and Co HCP, together with those we have found in the literature[1]. Exchange parameters are taking into account up to 6 shells. It is important to stress again that the exchange parameters presented in fig. 3.5 are valid for the spin Hamiltonian presented in eq. (2.1).

Except for the Fe BCC case, the exchange parameters calculated using the tight binding approach show a good agreement with the other different set of parameters presented in Fig. 3.5. All the parameters set calculated show typical RKKY oscilations, vanishing the magnitude of the exchange interactions as the distance increases. For Co FCC and HCP, we see that the first neighbor interaction is a little bit lower than for parameters published in [126, 156]. In the Ni FCC case, the results matches almost perfectly with results of [126]. However, for Fe BCC we see that neither the first neighbor exchange interaction nor the second one are similar to Pajda *et al* results [126], both are understimated. Besides, the first neighbor interaction is lower than the second one, which is completely unexpected.

The case of Co HCP is interesting because we see that exist different values of the exchange interactions for neighbors of the same distance, depending on the relative positions of the spins i and j. If they are placed in the same xy plane the have one value, if not they have a different one[2]. This result is confirmed with the results published by Turek *et al* [156]. This feature leads to the possibility of having different domain walls widths in Co HCP depending on the direction they are created. With the aim of studying this property, we began the work presented in chapter 4.

[1]For Co HCP we have found more recent parameters for Co HCP [94] but they are not represented in order to facilitate the understanding of fig. 3.5. However, next chapter deals with cobalt and all the exchange parametrizations we have found are presented in Table **??**.

[2]To be noted that we have assumed the c-axis of the HCP atomic structure parallel the z direction.

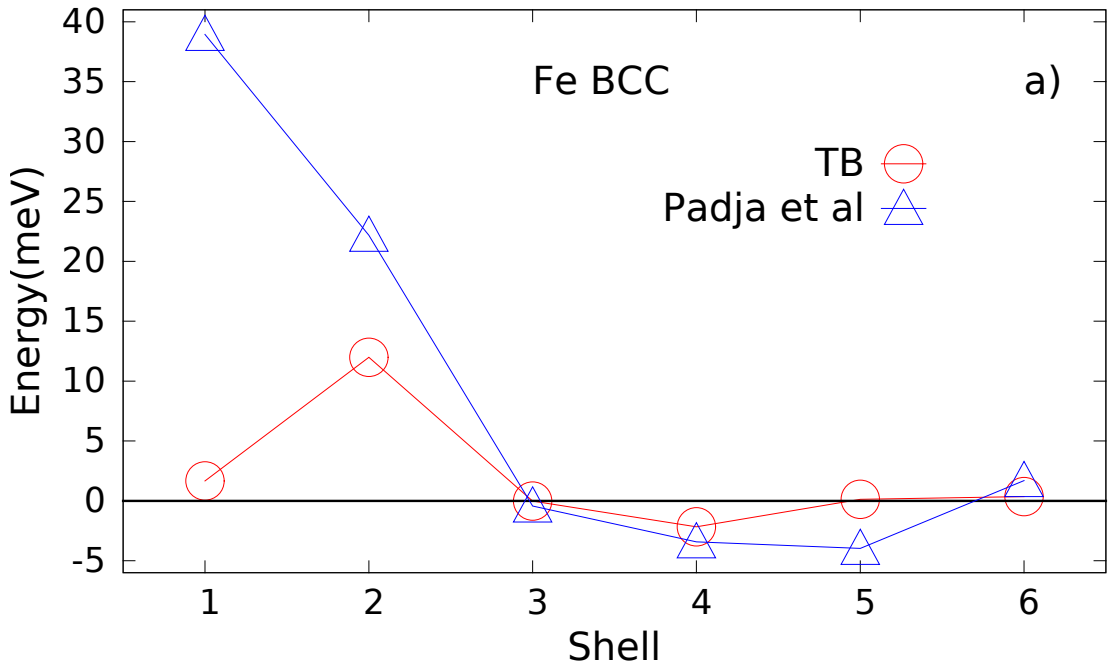
Fe BCC
a)
TB
Padja et al
Energy(meV)
Shell
40
35
30
25
20
15
10
5
0
-5
1
2
3
4
5
6

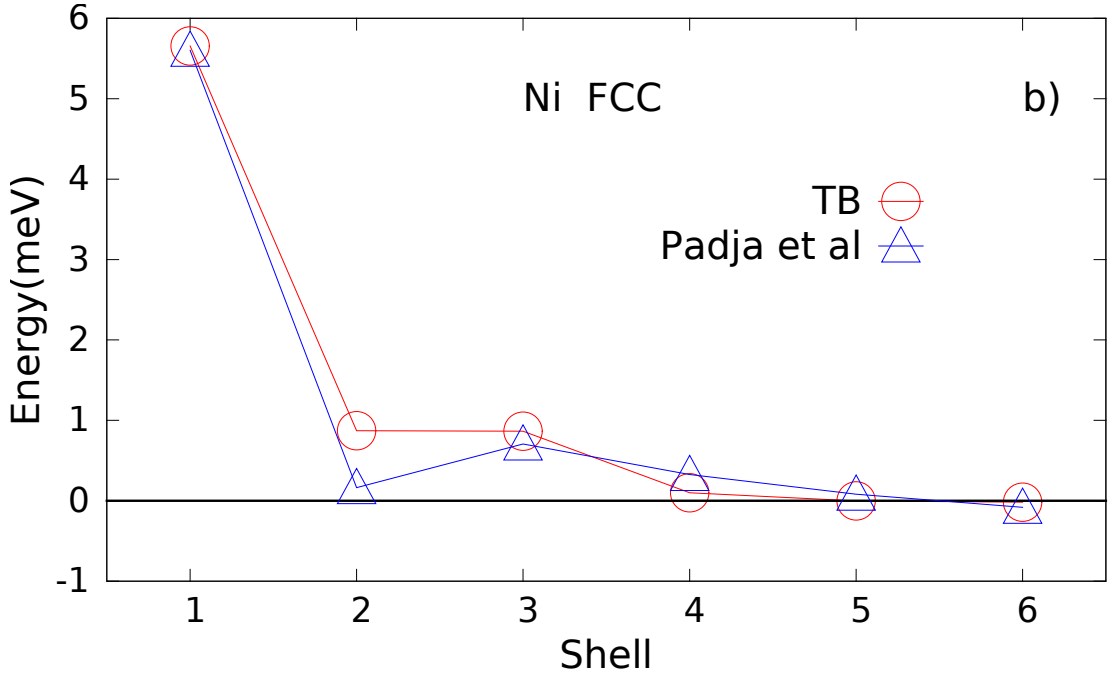
Ni FCC
b)
TB
Padja et al
Energy(meV)
Shell
6
5
4
3
2
1
0
-1
1
2
3
4
5
6

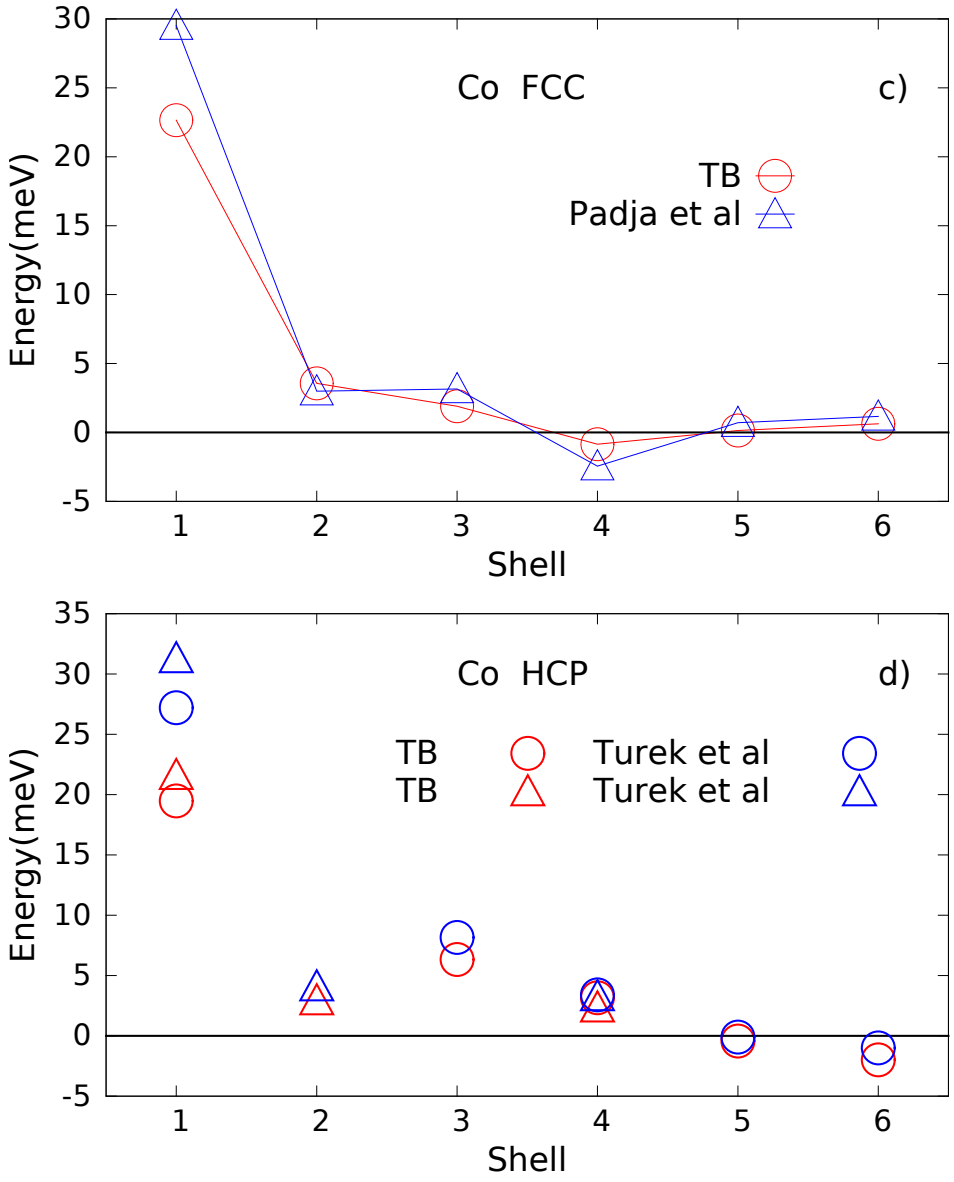

Figure 3.5: a), b) and c) represent the calculated exchange parameters using the tight binding approach (red circles), for Fe BCC, Ni FCC and Co FCC, for each shell or group of neighbors of the same distance. Blue triangles represents the exchange parameters calculated with more accurate methods by Pajda *et al* [126]. d) represents the calculated exchange parameters for Co HCP (red figures) together with the calculated by Turek *et al* [156] (blue figures). For Co HCP, circles represents the interactions between even planes and triangles between odd planes.

3.3.5 Temperature-dependent magnetisation and the Curie temperature.

Next, we calculate the magnetisation versus temperature curve for Ni FCC, Co FCC and Co HCP in order to determine its Curie temperature (T_C). Fe BCC magnetisation versus temperature curve is not presented due to the exchange coupling constants we have obtained are not correct. With this aim, we have used a public code from York university called Vampire in which Langevin dynamics is implemented [46].

For this kind of simulations, a big system must be simulated must be simulated in order to avoid fluctuations of the magnetisation at high temperatures, which difficult determining T_C. In the case of Co HCP we have used 20160 atoms, for Ni FCC and Co FCC 13500, which are not a really big system but enough to stimate the T_C. In figure 3.6, it is shown the calculated curves of magnetization versus temperature. Table 3.3 shows the resulting T_C as well as the experimental values and the values obtained from the exchange parameters extracted from Pajda [126].

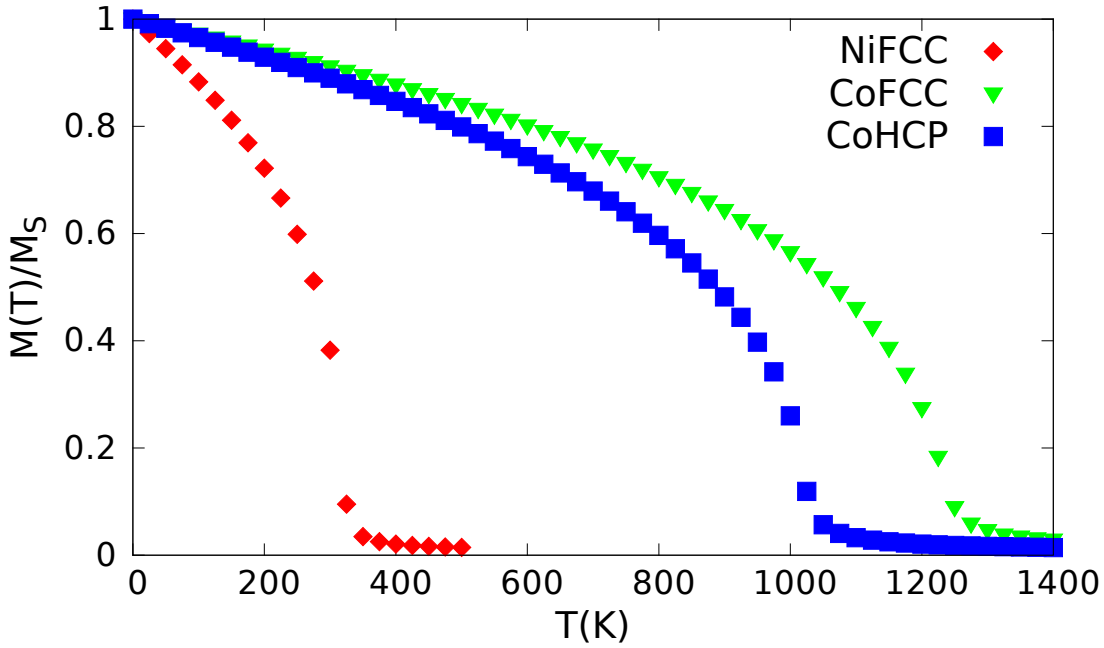

Figure 3.6: Normalized magnetization versus temperature for Ni FCC (red), Co FCC (green) and Co HCP (blue). Langevin dynamics has been perform using the atomistic exchange parameters calculated with the tight binding method. Atomistic simulations have been performed using the public code VAMPIRE [46].

	$T_C(K)$		
Atomic structure	Tight-binding	Experimental	*ab-initio*[a]
Fe BCC		1044-1045 [126]	800 [126]
Ni FCC	350	624-631 [126]	350 [126]
Co FCC	1100	1388-1398 [126], 1135 [39]	1450 [126]
Co HCP	1025		1480 [156]

Table 3.3: Results for the Curie temperature (T_C) extracted from the simulated magnetization versus temperature curve (figure 3.6). Experimental T_C values, as well as the T_C coming from Langevin dynamics simulations of ab-initio exchange parameters, are also considered

[a]These results correspond to Langevin dynamics simulations using the exchange coupling parameters published in the reference next to them

We see that for Ni FCC, the T_{C} value is the same than for the parameters found in [126] but the half of the experimetal T_{C}. This discrepance usually is attributed to the electronic configuration of nickel. As nickel has more electrons on its valence band than Fe or Co, it is expected that correlations effects in this material to be stronger . For this reason the different sets of exchange parameters calculated with different methods do not reproduce the experimental T_{C}.

In the case of Co FCC, we see that there two different values for the experimenal value of T_{C}. One of them is similar to the value we have obtained with the tight binding exchange parameters, the other one is similar to result of the exchange parameters published in [126]. For Co HCP we have calculated similar values but in this case we cannot compare with the experimental T_{C} because Co HCP transforms into Co FCC at 695 K [154].

3.4 Conclusions

In this chapter, we have calculated the band structure, the density of states, the magnetic moments and exchange coupling constants of the Heisenberg Hamiltonian for Fe BCC, Ni FCC, Co FCC and Co HCP. The exchange interactions obtained using the tight binding approach have been compared with the sets of parameters found in the literature obtained from more accurate methods. We also have performed atomistic spin simulations using the tight binding exchange interactions as well as with those obtained from literature.

To summarize the conclusions of this chapter:

- The tight binding exchange interactions (J_{ij}) are similar to those obtained with more accurate methods except for Fe BCC. Probably the two-center parametrization given in [127] is not good enough to calculate precisely exchange coupling parameters which are in the energy range of meV.
- The tight binding J_{ij} for Ni FCC are similar to those published in the literature, therefore, they are smaller than the needed to reproduce the experimental T_C. Probably, to calculate exchange parameters on Nickel it is needed to introduce correlation effects.
- For Co HCP we have found different values of the exchange interaction for neighbors of the same distance, depending on their relative positions. This is also reported in [156].
- The simulated T_C agrees well with the experimental one only for the case of Co FCC.

At this point, we decided to stop using the tight binding approach to parametrize the Heisenberg Hamiltonian. If for Fe BCC, which should be one of the simplest examples, the exchange parameters are so different from what they should be, probably the tight binding approach is not a good method to parametrize more complicated systems.

Nevertheless, this work has been useful because the difference of the exchange interactions for neighbors of the same distance for Co HCP was the seed of the work done in the next chapter, which has been published in Physica Review B [113].

4

Temperature-dependent exchange stiffness and domain wall width in Co

4.1 Introduction

For the correct use of micromagnetics the exchange stiffness, A, is one of the most important parameters since it defines the exchange correlation length, measuring the Bloch domain wall thickness $\delta_{DW} = \pi\sqrt{(A/K)}$, where K is the macroscopic anisotropy constant. However, the literature reveals a large discrepancy in the value of this parameter for Cobalt.

Hexagonal-close-packed (HCP) Cobalt is the classic high anisotropy magnetic material due to its high Curie temperature and large magneto-crystalline anisotropy in the bulk. Additives such as Pt and Sm enable HCP Co-based magnets to be used in current magnetic recording media and permanent magnets respectively. Yet, Co is not so simple. According to the measurements, HCP Co undergoes transition to the FCC phase [154] at temperatures around $T = 695K$ and at around the same temperature the magnetization easy axis turns perpendicular to the c-axis direction [151].

Micromagnetic simulations frequently assume values of the exchange stiffness in Co in two different ranges: $(1.3-1.5)\times10^{-11}$ J/m (e.g. [42, 129]) or $(2.2-3.3)\times 10^{-11}$ J/m (e.g. [41, 57, 99]). The experimental measurements on the exchange stiffness using Brillouin light scattering report values between 2.5×10^{-11} J/m [159] and 3.6×10^{-11} J/m [56]. At the same time old and forgotten neutron scattering data show higher values of 4.2×10^{-11} J/m [143]. The differences are normally attributed to non-homogeneous pinned structures due to grain boundaries in non-perfect samples [56].

Typically, the Bloch domain wall width in HCP Co is assumed to be between 10-15 nm, following classical books in magnetism (e.g. Refs. [86, 120]). We note here that the use of different exchange stiffness values may completely alter the result of a micromagnetic simulation since it defines the occurrence of different reversal modes, associated with different coercivities, as well as it may change the type of the reversal mode, for example from transverse to the vortex-like domain wall in HCP Co nanowires [67].

It is well known that both the anisotropy and the exchange stiffness in magnetic materials decrease with temperature. Since typically anisotropy decreases faster than the exchange stiffness, the domain wall width increases with temperature, which is widely observed experimentally (see, for example Ref.[160]). The correct temperature dependence of the exchange stiffness is important for applications since it may define the transition from incoherent to coherent reversal modes as well as change the domain wall velocity. Also, the change in the domain wall width with temperature has been determined as the key factor in its motion under thermal gradients [35] as well as for the ultra-fast magnetization dynamics response [131]. Thus accurately determining the rate of change of the domain wall width with temperature is very important from both fundamental and applied points of view.

In this chapter, starting with parametrizations of the Heisenberg Hamiltonian with *ab-initio* electronic structure calculations, we evaluate the exchange stiffness parameter and the domain wall width as a function of temperature. We determine the domain wall width at low temperatures as large as 24-29 nm, depending on the Heisenberg model parametrization. This value is larger than frequently assumed, and it increases with temperature. We also determine the scaling relation with magnetization of both the exchange stiffness parameter and the domain wall width.

4.2 Theoretical background

4.2.1 Definition of the exchange stiffness from atomistic exchange parameters.

The exchange stiffness parameter A, used in micromagnetics simulations, represents the strength coupling between macrospins. Its value, as explained in Aharoni's book [8], could be derived from atomistic exchange parameters J_{ij}, which in turn could be obtained from *ab-initio* methods.

Although the formulas needed to calculate the exchange stiffness parameter A from atomistic exchange parameters J_{ij} are presented in Aharoni's book [8] for

several atomic structures such as simple-cubic (SC), body-centered-cubic (BCC), face-centered-cubic (FCC) and hexagonal close packed (HCP), they only included the exchange interactions between first neighbors. However, the exchange interaction is known to be long-range, as shown in chapter 3. Thus, we extend Aharoni's formulas to include exchange interactions up to the desired number of neighbors. In this work we have taken into account up to the 6th neighbor, because this is the number of neighbors where typically the exchange interactions become negligible 3. In addition, the Heisenberg hamiltonian definition given in Aharoni's book [8] differs from the definition typically used in atomistic spin simulations (see subsection 2.2.3) by a factor 1/2. To be noted that although Aharoni's formulas differ from our formulas the result for A should be the same.

In order to obtain the relation between the exchange stiffness parameter A and the Heisenberg exchange parameters, we first consider the energy difference between the ground state of a ferromagnetic system at zero temperature (all the atomic spins are parallel) with a state in which the spins are not completely aligned.

$$E_{exc} = -\frac{1}{2}\sum_{i\neq j} J_{ij}\left(1 - \vec{s}_i\vec{s}_j\right) = -\frac{1}{2}|S|^2\sum_{i\neq j} J_{ij}\left(1 - cos\left(\theta_{ij}\right)\right) \tag{4.1}$$

where i and j represent the lattice sites, $\vec{s}_i$ and $\vec{s}_j$ are the spins vectors placed in the positions i and j respectively, θ_{ij} is the angle between vectors $\vec{s}_i$ and $\vec{s}_j$, $|S|$ is the module of the spin vectors, and J_{ij} represent the exchange energy between them. The rotations of the spins are supposed to be small, thus it is possible to expand $cos\left(\theta_{ij}\right)$ in eq 4.1 up to the first second power of Taylor series leading to

$$E_{exc} = \frac{1}{2}\sum_{i\neq j} J_{ij}\left(\frac{\theta_{ij}^2}{2}\right) \tag{4.2}$$

As the rotations of the spins are considered to be small and the spins are unitary vectors, thus

$$\left|S_i - S_j\right| = sin\left(\theta_{ij}\right) \approx \left(\theta_{ij}\right) \tag{4.3}$$

Substituing it in eq 4.2 we reach

$$E_{exc} = \frac{1}{4}\sum_{i\neq j} J_{ij}\left|S_i - S_j\right|^2 \tag{4.4}$$

The atomic spins in a ferromagnetic system are almost parallel, therefore the change of the direction of the spins between adjacent atoms should be small. This fact allows us to define a smooth continuous variable **m** equal to the spin direction

in each atomic site. Therefore, expanding $\mathbf{m}$ in its Taylor series, centered in atom i with direction $\vec{r}_{ij}$ where $\vec{r}_{ij}$ is a vector pointing from atom i to atom j

$$\mathbf{m(i)} = \mathbf{m(j)} + \mathbf{r_{ij}} \cdot \nabla \mathbf{m} \tag{4.5}$$

which leads to

$$E_{exc} = \frac{1}{4} \sum_{i \neq j} J_{ij} \left| \vec{r}_{ij} \cdot \nabla \mathbf{m} \right|^2 \tag{4.6}$$

As j index runs over all atoms except i it is possible to rewrite the last equation in terms of the neighbors groups[1].

$$E_{exc} = \frac{1}{4} \sum_{i} \left(\sum_{j \in N_{i1}} J_{ij} \left(\vec{r}_{ij} \cdot \nabla \mathbf{m} \right)^2 + \sum_{j \in N_{i2}} J_{ij} \left(\vec{r}_{ij} \cdot \nabla \mathbf{m} \right)^2 + \cdots \right) \tag{4.7}$$

where $N_{i1}, N_{i2}, etc.$, mean the first, second, etc. neighbors respect to atom i. Taking into account only the first neighbor group, Aharoni's formulas must arise just with the difference of a factor $1/2$ coming from the definition of the Heisenberg Hamiltonian. For the time being, all the neighbors are kept in the formula.

Considering a continous system instead a discrete one, we change the sumation over the atoms i to an integral over the space leading to a final equation valid for any number of neighbor groups and for every atomic structure, if the atomic structure is composed of only one atom type, as for the bulk cobalt.

$$E_{exc} = \frac{1}{4V_0} \sum_{j} J_{0j} \int \left[\left(r_{0jx} \nabla \mathbf{m_x} \right)^2 + \left(r_{0jy} \nabla \mathbf{m_y} \right)^2 + \left(r_{0jz} \nabla \mathbf{m_z} \right)^2 \right] dV \tag{4.8}$$

where V_0 is the atomic volume. Independently to which atom 0 is taken as a reference to introduce the distances $r_{0j\nu}$ ($\nu = x, y, x$) and the exchange paramters J_{0j} in eq 4.10, the result of A_ν will be the same. To be noted that if an atom j is selected, and the reference atom 0 is changed 1, then $r_{0j\nu}$ and $r_{1j\nu}$ will be probably different. However, if the product $J_{1j} \cdot r_{1jx}^2$ is non-zero, then there exits one j' for which $J_{1j} \cdot r_{1jx}^2 = J_{0j'} \cdot r_{0j'x}^2$ and therefore the result of A_ν will be the same[2]. Hence, the definition of the components of the exchange stiffness is

$$A_\nu = \sum_{j} \frac{J_{ij} r_{0j\nu}^2}{4V_0} \qquad \nu = x, y, z. \tag{4.9}$$

[1] A neighbor group or shell respect to an atom i is defined as the set of atoms j which are at the same distance respect to the atom i

[2] More complicated atomic structures than HCP such as Laves phases structures, which have more than one atom type, require a redifinition of V_0, see chapter 6.

and,

$$E_{exc} = \int \left[A_x \left(\nabla \mathbf{m_x} \right)^2 + A_y \left(\nabla \mathbf{m_y} \right)^2 + A_z \left(\nabla \mathbf{m_z} \right)^2 \right] dV \tag{4.10}$$

If ths system is cubic then the exchange stiffness becomes isotropic and reduces to the well-known exchange energy in micromagnetism.

$$E_{exc} = A \int \left[\left(\nabla \mathbf{m_x} \right)^2 + \left(\nabla \mathbf{m_y} \right)^2 + \left(\nabla \mathbf{m_z} \right)^2 \right] dV \tag{4.11}$$

Eq. 4.9 makes possible to calculate the exchange stiffness parameter A from an *ab-initio* given set of atomic exchange parameters, but strictly speaking, this value is only valid at zero temperature. Nevertheless, it is possible to calculate the temperature dependence of the exchange stiffness parameter A either numerically, via simulating the Bloch domain wall width or analitically, using the Classical Spin Density Method $CSDM$ [17, 30]. Next chapter introduces the basics of the Bloch domain walls.

4.2.2 Bloch domain wall

A magnetic system described with the exchange energy plus the uniaxial magnetic anisotropy energy (see eq. 2.1), in which a domain wall is forced to appear, gives as a result a Bloch domain wall if the system is long enough [76]. Firstly, the domain wall must be forced to appear either by applying anti-periodic boundary conditions or introducing an antiferromagnetic exchange interaction between the bounds of the domain wall. Secondly, the system must be long enough to fully contain the domain wall. Taking into account these two conditions, atomistic simulations at any temperature must give as a result a Bloch domain wall whose profile is described by

$$m_z(x,T) = m_e(T) \tanh(\pi(x - x_0)/\delta(T)_\nu) \tag{4.12}$$

where $\delta(T)_\nu$ is the domain wall width at temperature T along the direction $\nu = x, y, z$, x_0 is the position where the domain wall center and $m_e(T)$ is the equilibrium magnetization at temperature T.

The relation of the domain wall width $\delta(T)_\nu$ with the macroscopic exchange stiffness and the anisotropy constant is considered to be the same as at zero temperature, i.e. the following

$$\delta(T)_\nu = \pi \sqrt{\frac{A(T)_\nu}{K(T)}}, \tag{4.13}$$

where $A(T_\nu)$ is the exchange stiffness parameter in the direction ν and $K(T)$ is the magnetic anisotropy constant at any temperature T. This equation is the key for calculating the exchange stiffness temperature dependence from the domain wall width and the anisotropy. The domain wall width temperature dependence $\delta(T)_\nu$ could be calculated simulating Bloch domain walls at any temperature using Langevin Dynamics approach (see subchapter 2.2.3) and fitting the result to eq. (4.12). For the case of the temperature dependence of the anisotropy ($K(T)$), we use the Constrained MonteCarlo method (see subchapter 2.2.4) .

4.3 Modeling results

4.3.1 The Spin Hamiltonian parameterization.

The long-range pair-wise exchange parameters for Co are evaluated by mapping the electronic structure calculation into the Heisenberg model. In chapter 3, the Heisenberg Hamiltonian has been parameterized using the tight binding (TB) approach for Fe BCC, Ni FCC, Co FCC and Co HCP. More accurate parametrizations are based on *ab-initio* methods, see for Co HCP in [94, 156] and for Fe BCC, Ni FCC and Co FCC in [126]. For the case of Co HCP, all the parameter sets in the literature show typical RKKY oscillating behaviour and the exchange anisotropy, i.e. the exchange parameters (J_{ij}), apart from depending on the distance of the spins placed in sites i and j, depend on the relative position of the spins i and j with respect to the c-axis of the HCP atomic structure. In other words, although the distance between spins i and j is the same, J_{ij} values are different if the spins are placed in the same plane or not, which agrees with the results obtained in chapter 3. In our simulations for Cobalt we used the parameters from the references above, see Table 4.1. Since in the literature two contradictory sets of parameters: the older one by Turek *et al* [156] and the very recent one by Kvashnin *et al* [94] have been found, our co-author Serguej Khmelevskiy from the Vienna University of Technology has calculated another parameter set, also showing the exchange anisotropy.

The technique used by S. Khmelevskyi is based on the Local Spin-Density Approximation and bulk Korringa-Kohn-Rostokker (KKR) method in the Atomic Sphere Approximation (ASA) [6, 136]. The partial waves in the KKR-ASA calculations have been expanded up to the orbital $l_{max} = 3$ (*spdf* basis) inside the atomic spheres, for all non-equivalent atomic sites. The exchange parameters have been calculated using the magnetic force theorem [100]. The exchange constants were estimated in ferromagnetic ground state at $T = 0$ K, which give a reasonable estimation also at non-zero temperatures for both FCC and HCP Co.

The method of the exchange constants calculation is essentially the same as that of Pajda *et al* [126] or Turek *et al* [156] for Co FCC and Co HCP respectively. However, S.Khmelevskiy used a more extended basis for partial wave expansion (l_{max} = 3) than Turek *et al* who used l_{max} = 2. Because of that, the exchange constants are closer to Kvashnin *et al* [94], who used a full potential methodology. Previously, the application of this approach has allowed a successful description of magnetism in various transition metal systems [77, 78].

Co (HCP)						
			TB	Khmelevskiy	Kvashnin *et al* [94]	Turek *et al* [156]
J_{ij} label	R_{0j}	N_s	$J_{0j}(meV)$			
J_{1a}	(100)	6	19.478	24.126	21.769	27.2
J_{1b}	$(\frac{1}{2}\frac{1}{2\sqrt{3}}\sqrt{\frac{2}{3}})$	6	21.602	28.27	24.762	31.28
J_{2b}	$(1\frac{-1}{\sqrt{3}}\sqrt{\frac{2}{3}})$	6	2.918	3.755	2.72	4.08
J_{3a}	$(00\sqrt{\frac{8}{3}})$	2	6.325	6.61	5.44	8.16
J_{4a}	$(0\sqrt{3}0)$	6	3.163	2.83	2.18	3.4
J_{4b}	$(1\frac{2}{\sqrt{3}}\sqrt{\frac{2}{3}})$	12	2.334	2.42	2.18	3.26
J_{5a}	$(10\sqrt{\frac{8}{3}})$	12	-0.433	-0.81	-0.68	-0.1
J_{6a}	(200)	6	-1.992	-2.095	-1.36	-1.00

Table 4.1: Calculated exchange parameters in chapter 3, S.Khmelevskiy's exchange parametrization as well as the different parameters sets found in literature for HCP cobalt up to the first 6 shells. R_{0j} is the shell position in units of lattice constant, N_s is the number of equivalent sites in the shell and J_{ij} label is name given to each exchange interaction where $i \in [1,6]$ refers to the neighbor number and $j \in [a,b]$ refers to even or odd planes respect to the reference atom.

In Table 4.1 Table 4.2 we present the different exchange parameter sets for Co HCP and Co FCC extracted from literature, the results obtained in section

Co (FCC)					
			TB	Serguej	Pajda *et al* [156]
J_{ij} label	R_{0j}	N_s	$J_{0j}(meV)$		
J_1	$(\frac{1}{2}\frac{1}{2}0)$	12	22.65	25.463	29.524
J_2	(100)	6	3.56	2.22	2.99
J_3	$(1\frac{1}{2}\frac{1}{2})$	24	3.16	2.90	3.16
J_4	(110)	12	-0.85	-3.16	-2.45
J_5	$(\frac{3}{2}\frac{1}{2}0)$	24	0.13	0.76	0.71
J_6	(111)	8	0.63	1.27	1.17

Table 4.2: Calculated exchange parameters from chapter 3, S.Khmelevskiy's exchange parametrization as well as the different parameters sets found in for FCC cobalt up to the first 6 shells. R_{0j} is the shell position in units of lattice constant, N_s is the number of equivalent sites in the shell and J_i label is name given to each exchange interaction where $i \in [1, 6]$ refers to the neighbor number.

3 using the TB approach as well as the parameters calculated by S. Khmelevskyi [1]. The exchange parameters show dominant ferromagnetic interactions up to the third nearest neighbours and the typical RKKY oscillating asymptote. In what follows we only included the exchange interactions up to 6 nearest neighbours. The different sets of exchange parameters presented are calculated in the same conditions of the S. Khmelevskiy's set, for $T = 0K$ and in the ferromagnetic state. A big variation of the exchange parameters with temperature is not expected, therefore, simulating with zero-temperature exchange constants is a good approximation [28]. Thus, in our simulations, no temperature dependence of the exchange parameters is considered. Apart from the ferromagnetic (Fm) state, the exchange parameters can be calculated using the disordered local moment (DLM) approach [146] (see also section 6).

Finally, the value of the magnetic moment which is going to be used in Langevin dynamics (see section 2.2.3) for Co HCP, is the value calculated in the previous chapter, which is shown in Table 3.2 and corresponds to the value

[1] Original Serguej's, Kvashnin's, Pajda's and Turek's sets of exchange parameters are presented in mRy and they are calculated for the Hamiltonian $H = -\sum_{ij} J_{ij}\vec{s}_i\vec{s}_j$.

published in [127]. Althought magnetic moments are explicity shown in eq. (2.1), they appear in the Zeeman energy term, but in this chapter, we are not considering any external magnetic field. However, they are needed to calculate the effective magnetic fields that interacts with each atomic spins, see eq. (2.4), therefore, they are always needed for atomistic simulations 2.2. In any case, it is not expected that δ_{DW} value depends on the magnetic moments μ itself, but μ value will determine the dynamics of the system during the domain wall forming process. The sizes of magnetic fluctuations are also dependent on it.

4.3.2 Temperature-dependent magnetisation and the Curie temperature.

To evaluate temperature dependent magnetisation we use the classical Langevin dynamics simulations based on the integration of a set of stochastic Landau-Lifshitz-Gilbert (LLG) equations [46] with internal fields defined by the Hamiltonian written in eq. (2.1) and additional random fields, as described in section 2.2.3.

Firstly, the magnetization curves versus temperature have been calculated, see Fig. 4.1. The resulting Curie temperatures are summarized in Table 4.3 (HCP Co) and 4.4 (FCC Co) for the different sets of parameters.

The T_C = 1480K value, which we calculate here by the Langevin dynamics approach with the parameters of Turek *et al* is close to the most frequently cited experimental value for Co T_{C} = 1385K (e.g. the book [120]) measured in [38, 117]). Because of that agreement, this parametrization gives a suitable for magnetisation dynamics modeling curve $M(T)$ and we still use values from Turek *et al* [156] in our calculations. S. Kmelevskiy's parameters set also gives as a result a Curie temperature close to the experimental one for both HCP (T_C = 1250 K) and FCC (T_C = 1300 K) phases, although they are now below it. At the same time the calculations by Kvashnin *et al* [94]) give a smaller Curie temperature T_C = 1100 K but in agreement with the value of 1131 K cited in the book by Cullity [39]. The TB parameters and its corresponding Curie temperature T_C = 1025 K are close to the ones from Kvashnin *et al*.

We note that our estimations of T_C do not include the effects of longitudinal spin fluctuations at high temperatures and renormalization of the exchange constants due to the spin disorder in a paramagnetic state [136]. Thus the obtained T_C values cannot be considered as a test of the exchange constants quality which are calculated from the low temperature ferromagnetic reference state. However, namely the exchange constants calculated in the ferromagnetic ground state must

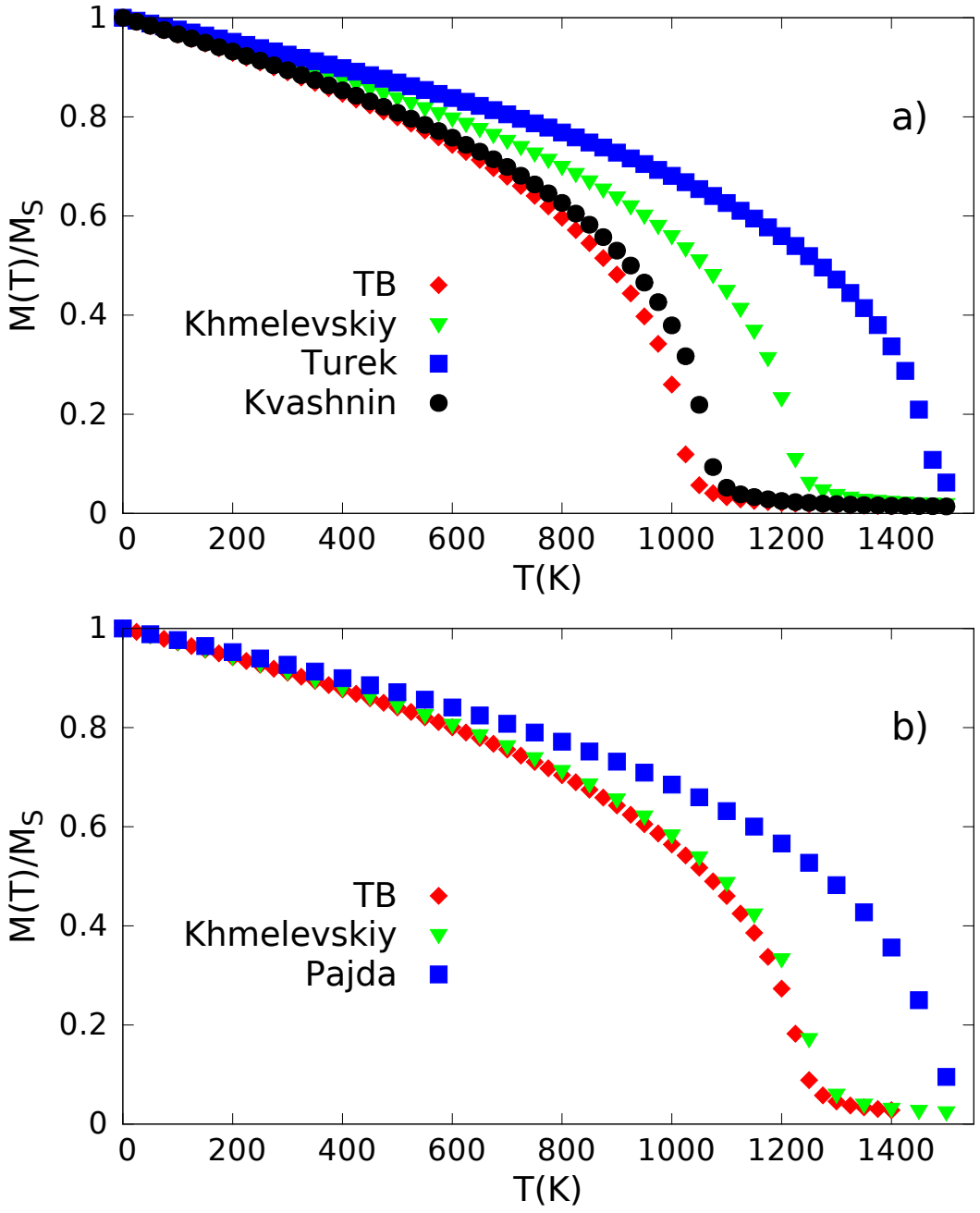

Figure 4.1: Figures a) and b) represent the magnetisation versus temperature curves for cobalt HCP and FCC respectively. Each curve corresponds to a different set of exchange parameters, which are presented in Table 4.1 and Table 4.2 for cobalt HCP and FCC respectively.

be used at the temperatures lower than experimental magnetic ordering temperature. Note also that within the disordered local moment approach the dependence of the Heisenberg exchange coupling constants for HCP Co has been found to be very weak [28] in the considered here range of temperatures.

4.3.3 Evaluation of the temperature dependence of magnetic anisotropy

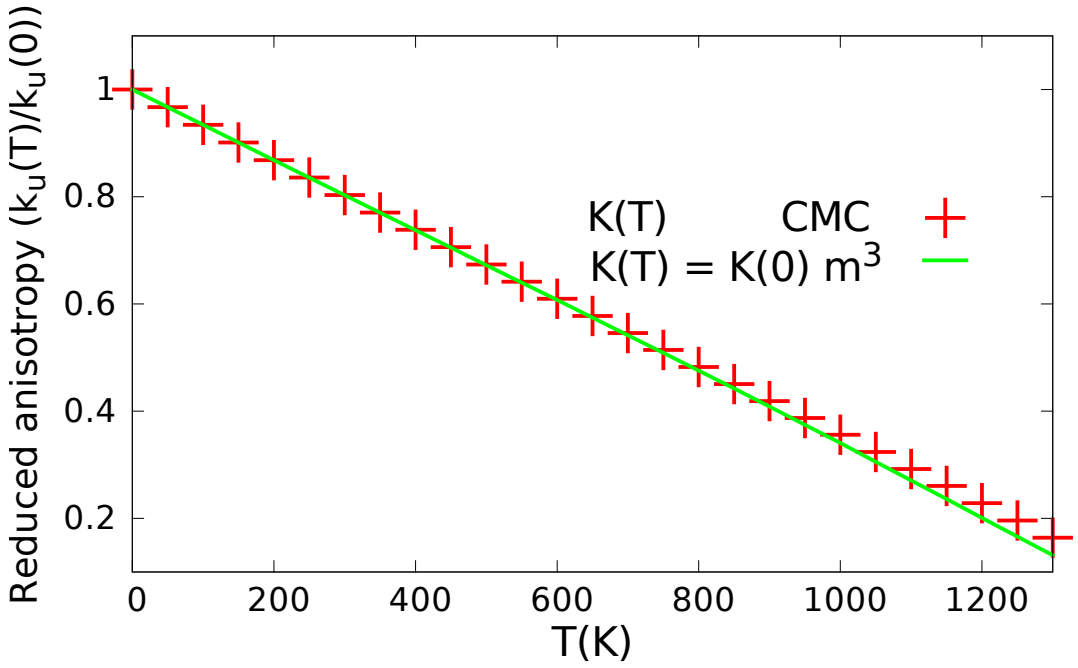

Figure 4.2: Red crosses represent the anisotropy temperature dependence calculated with Constrained Monte Carlo method (see subsection 2.2.4) using Vampire code [5, 46]. Green line represents the Callen-Callen scaling law ($K(T) \sim K(0)m^3$) [29].

The domain wall width depends on the macrosopic anisotropy value K as it is written in 4.13, therefore we need to evaluate its temperature dependence. The value of the atomic uniaxial magnetic anisotropy in the spin Hamiltonian, eq. (2.1), has been taken from literature due to the fact that an *ab-initio* estimation of this value is difficult and not too much reliable. Therefore with the aim of calculating a realistic value of the δ_{DW} we take a experimental value for Co HCP $k_u = 5.83 \cdot 10^{-11} J/atom$ which corresponds to the macroscopic value $K = 0.53 \times 10^6$ J/m^3 [70]. The relation between the microscopic and macroscopic anisotropy constants is obviously given by the atomic volume $V_{at} = 1.1 \cdot 10^{-29} m^3$ which is

calculated from the experimental lattice constant $a = 2.50 \cdot 10\mathring{A}$ [127]. For Co HCP the atomic volume reads

$$V_{at} = \frac{a^3}{\sqrt{2}} \tag{4.14}$$

and,

$$k_{\mathrm{u}} = K \cdot V_{at} \tag{4.15}$$

Note that a constant atomic anisotropy value gives a temperature-dependent macroscopic anisotropy. There may be an additional temperature dependence of the on-site anisotropy which is difficult to estimate. Specifically, the intrinsic change of anisotropy happens via the temperature-induced transformation from HCP to FCC structure. However, we note that a different anisotropy value changes the domain wall width but is not important for the determination of the temperature dependence of the exchange stiffness parameter.

The magnetic anisotropy temperature dependence of Co HCP is well-known to follow Callen-Callen scaling law ($K(T) \sim m^3$) [29]. The Constrained Monte Carlo method (CMC), which is described in section 2.2.4, has been demonstrated to reproduce the Callen-Callen scaling law for anisotropy, in particular, the macrosopic anisotropy of HCP structures is demonstrated to follow $K(T) \sim m^3$ [14]. Our calculations reproduces this result using Vampire code [5, 46], which has this method implemented, see Fig. 4.2. Computational work was done setting for a given temperature the HCP c-axis parallel to z direction and fixing the magnetization direction to the angle θ which was varied from $\theta = 0$ to $\theta = 2\pi$ and extracting the torque for each value. Fitting this torque to eq. (2.10) the corresponding value of the anisotropy for each given temperature is extracted. This process is repeated in the temperature range of $T \in [0, 1300]$. Results are presented in Fig 4.2 together with corresponding Callen-Callen scaling law for uniaxial anisotropy showing a good agreement up to 1200 K.

4.3.4 Low temperature exchange stiffness and the domain wall width

The different sets of atomistic exchange parameters (J_{ij}) shown in Tables 4.1 and 4.2 for Co HCP and Co FCC respectively are going to be used as inputs to calculate the zero temperature exchange stiffness (A), using the extension of Aharoni's formulas [8] to include long-range exchange parameters, which is derived in section 4.2.1. Recalling that Co HCP shows an anisotropy in exchange interactions, the exchange stiffness in xy plane and in c-axis must be calculated

separately. To be specific, the explicit equations used to calculate A_ν (for Co HCP), with $\nu = x, y, z$, and A (for Co FCC), taking into account up to 6 nearest neighbours, are the following:

$$A_{x(y)} = \frac{a^2}{4V_{0_{HCP}}}\left[3 \cdot J_{1a} + J_{1b} + 4 \cdot J_{2b} + 9 \cdot J_{4a} + 14 \cdot J_{4b} + 6 \cdot J_{5a} + 12 \cdot J_{6a}\right], \quad (4.16)$$

$$A_z = \frac{a^2}{4V_{0_{HCP}}}\left[4 \cdot J_{1b} + 4 \cdot J_{2b} + \frac{16}{3} \cdot J_{3a} + 8 \cdot J_{4b} + 32 \cdot J_{5a}\right]. \quad (4.17)$$

$$A_{FCC} = \frac{a^2}{4V_{0_{FCC}}}\left[2 \cdot J_1 + 2 \cdot J_2 + 12 \cdot J_3 + 8 \cdot J_4 + 20 \cdot J_5 + 8 \cdot J_6\right] \quad (4.18)$$

where a is the lattice parameter, $V_{0_{HCP}}$ is the atomic volume corresponding to HCP structure given by eq. (4.14), $V_{0_{FCC}} = a^3/4$ is the atomic volume corresponding to FCC structure and J_{ij} are the exchange constants and they are labeled as in Table 4.1. The resulting exchange stiffness for each parameters set are summarized in Table 4.3 and Table 4.4 for Co HCP and Co FCC respectively.

	TB	Serguej	Kvashnin *et al* [94]	Turek *et al* [156]
Exchange stiffness				
Plane xy (10^{-11} J/m)	2.97	3.33	2.95	4.38
c-axis (10^{-11} J/m)	3.26	3.62	3.02	4.73
Domain wall width		$T = 0\ K$		
Plane xy(nm)	23.51	24.88	23.42	28.49
c-axis (nm)	24.64	25.96	23.70	29.60
$CSDM$				
ϵ	0.242	0.207	0.208	0.186
	$A \sim m^{1.76}$	$A \sim m^{1.79}$	$A \sim m^{1.79}$	$A \sim m^{1.81}$
$T_C(K)$	1025	1250	1100	1480

Table 4.3: Results for different Co HCP parameterizations.

Firstly, it is interesting to remark that the calculated exchange stiffness for HCP Co and for FCC Co have similar values. If the exchange parameters set for both atomic structures are calculated with the same *ab-initio* method, then the resulting exchange stiffness values are similar for both cases.

	TB	Serguej	Pajda *et al* [156]
Exchange stiffness (10^{-11} J/m)	3.22	3.62	4.41
$CSDM$	$\varepsilon \sim 0.310$	$\varepsilon \sim 0.180$	$\varepsilon \sim 0.177$
	$A \sim m^{1.69}$	$A \sim m^{1.82}$	$A \sim m^{1.82}$
$Tc(K)$	1250	1300	1550

Table 4.4: Results for different Co FCC parameterizations.

Secondly, it seems that the value of A for HCP Co in micromagnetism has been systematically underestimated due to the fact that for all the parameters sets which we used here, the exchange stiffness value is similar to the upper bound or larger than typically used in micromagnetic simulations, frequently by a factor of 2 times. The different A values shown in Table 4.1 match on its lower bound with the largest value used in micromagnetics simulations [1] as well as with the data reported with Brillouin light scattering experiments. On its upper bound, they agree with the neutron scattering measurements [143].

Thirdly, there is a slight anisotropy in the exchange stiffness arising from the atomic exchange parameters for HCP Co. We should remark that the Co HCP exchange stiffness A appears in Ref. [8] as isotropic, because only isotropic first neighbors interactions were considered. Taking into account the second neighbors without any exchange anisotropy, A remains isotropic (see eq 4.16, 4.18), but with more neighbors or the exchange anisotropy, A becomes anisotropic. In any case, this anisotropy is small and may be probably disregarded.

Using the exchange stiffness results shown in Table 4.3 for HCP, the microscopic anisotropy value presented at the end of the previous chapter ($K = 0.53 J/m^3$) and eq. (4.13) we calculate the domain wall widths (δ_{DW}) corresponding to each parameters set at $T = 0$. Results are shown in Table 4.3. As the exchange stiffness values are larger than the typically assumed values, the domain wall widths also are. In fact, δ_{DW} is determined to be in the range $[24 - 29nm]$, which is larger than the 15 nm reported in classical books such as [120]. The exchange anisotropy gives different domain wall widths parallel to the c-axis and in xy-plane but this difference results to be very small, less that $1nm$ in all cases.

To mutually validate theoretical and modeling results, we perform Langevin dynamics atomistic simulations for Co HCP with the aim to create a Bloch domain wall, fit its profile to eq. (4.12) and extract its domain wall width.[1]. For this purpose, Turek's parameter set has been selected as an example because it has the largest T_C well in agreement with the experimental one. The atomistic

[1]To be noted that it is only possible with our code to simulate HCP Co domain walls because the anisotropy is larger than FCC Co anisotropy and the corresponding domain wall is smaller.

simulation codes which has been used are: our home-made one as well as the publicly available VAMPIRE code [5, 46]. The system size has been set 80 nm of length and with a cross-sectional area of 250 nm^2 in order to fully contain the domain wall. The domain wall is constrained in the system by applying anti-periodic boundary conditions. We calculated both c-axis and in-plane xy domain walls. First the temperature used in Langevin dynamics was $T = 3K$, to be close to the zero-temperature theoretical domain wall width value which is calculated for $T = 0K$ [1].

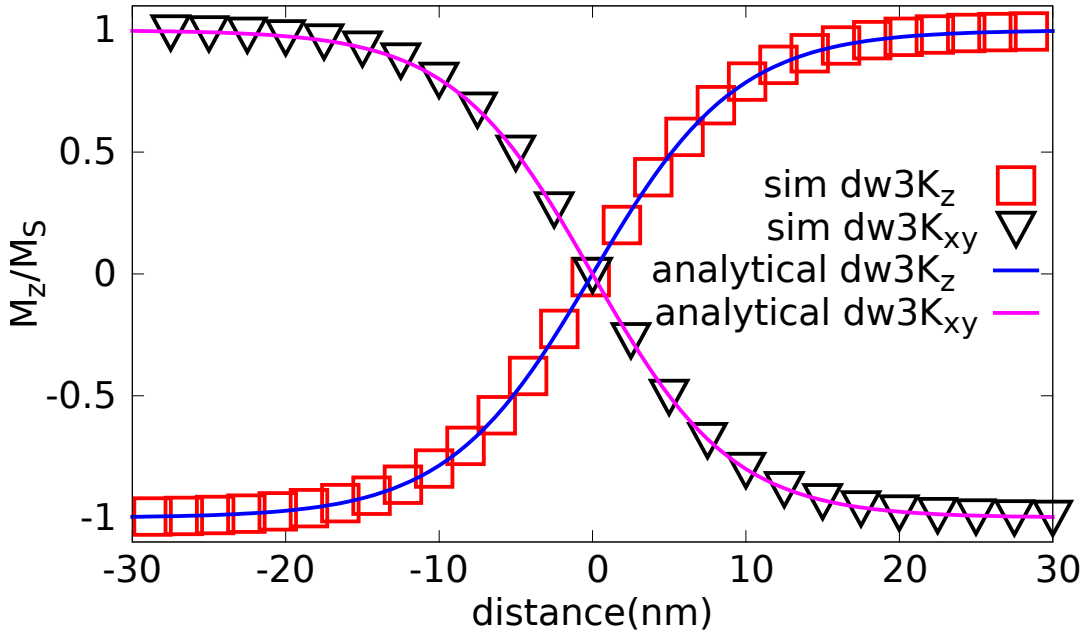

Figure 4.3: Red squares and black triangles crosses represent the simulated domain wall profiles for temperature $T = 3$ K, using the exchange values of Turek *et al* [126] along the c-axis and inside xy plane respectively. The difference between their domain wall width values is small, so to distinguish them, xy plain DW has been represented with oppsosite sign of c-axis.

As it is shown in Fig 4.3 both theoretical and simulated domain walls are in very good agreement. Even more, the small theoretical difference in the domain wall widths between c-axis and xy-plane is well reproduced. Theoretical values obtained for low temperatures are $\delta^x_{DW} = 28.49$ nm and $\delta^z_{DW} = 29.60$ nm which are presented in Table 4.3; $\delta^x_{DW} = 28.50$ nm, $\delta^z_{DW} = 29.59$ nm with our program and $\delta^x_{DW} = 28.50$ nm, $\delta^z_{DW} = 29.57$ nm with VAMPIRE.

[1] A non-zero temperature close to $T = 0K$ has been selected in order to allow thermal fluctuations in Langevin dynamics without loosing precision in the domain wall width result.

4.3.5 Theoretical estimation of the low temperature scaling of the exchange stiffness and the domain wall width

The temperature dependence of the exchange stiffness can be expressed in terms of a scaling law with the magnetization $A(T) = A(0)m(T)^{\alpha}$, where α is some parameter to determine. As the temperature dependence of the magnetisation has been determined in section 4.3.2, α is the only unknown parameter to calculate $A(T)$. To determine the theoretical exchange stiffness scaling with magnetization (i.e. temperature), we employ the classical spectral density method (CSDM) for spinwaves [17, 30], previously shown to have a good agreement with the Langevin simulations in simple cubic lattice materials and FePt [17, 22].

The classical spectral density method (CSDM) for spinwaves [17, 30] is a method based on the use of Green's functions in reciprocal space which first leads to an infinite set of coupled equations for thermally averaged moments of all orders. The spectral density is assumed to be a delta-function. The following decoupling scheme which leaves the equations for the first two moments only (found to be sufficient for the exchange interactions [17, 30]) is then assumed

$$\langle S^z_{\mathbf{k}} S^z_{-\mathbf{k}} \rangle \cong \langle S^z_{\mathbf{k}} \rangle \langle S^z_{-\mathbf{k}} \rangle - \frac{1}{2}(1-m^2)\langle S^+_{\mathbf{k}} S^-_{-\mathbf{k}} \rangle, \tag{4.19}$$

where m is the average magnetization, $S^{\pm}_{\mathbf{k}}$ is the Fourier transform of $S^{\pm}_i = S^x_i \pm S^y_i$ variables and $S^z_{\mathbf{k}}$ of S^z_i variable. The Fourier transform of the exchange parameters is defined in terms of the variable

$$\gamma_{\mathbf{q}} = \frac{J(\mathbf{q})}{J(0)} = \sum_j \frac{J_{0j}}{J(0)} \cdot e^{-i\mathbf{q}\cdot(\mathbf{r}_0 - \mathbf{r}_j)}, \tag{4.20}$$

where $J(0)$ is the is the zero wave-vector component $J(0) = z_1 \cdot J_{01} + z_2 \cdot J_{02} + \ldots$, z_{0j} is the number of neighbors with the same J_{0j} interaction, $\vec{r}_0$ and $\vec{r}_j$ are position vectors of the atoms 0 and j respectively. The decoupled equations give the following dispersion relation [17]

$$\omega_{\mathbf{q}} = J_0 m Q(m)(1-\gamma_{\mathbf{q}}), \tag{4.21}$$

where at low temperatures the function $Q(m)$ scales with magnetization m as $Q(m) \propto m^{-\varepsilon}$ and the scaling parameter ε is defined by the ratio of the sums $\varepsilon = G/W$:

$$W = \sum_{\mathbf{q}} \frac{1}{1-\gamma_{\mathbf{q}}}, \quad G = \sum_{\mathbf{q}} \frac{\gamma_{\mathbf{q}}}{1-\gamma_{\mathbf{q}}}, \tag{4.22}$$

The spinwave dispersion relation (4.21) is directly related to the exchange stiffness parameter leading to the scaling relation $A(T) = A(0) \cdot m^{2-\epsilon}$. The difference with the mean-field exponent $\varepsilon = 2$ comes from spin-spin correlations [17].

Equations 4.22 were numerically evaluated over the first Brillouin zone giving $\varepsilon \approx 0.19$ for parameters of Turek *et al* [156] and $\varepsilon \approx 0.21$ for the rest of parameters sets. They also have been evaluated for Co FCC parameters with $\varepsilon \approx 0.18$ as a result. Therefore the exchange stiffness scales with magnetization with $A \sim A(0)m^{1.8}$ for all cases (see Table 4.3 and Table 4.4 for more precise values). This result is compared in Fig. 4.7 with direct estimations of the exchange stiffness parameter via the temperature-dependent domain wall width simulations (see below), showing good agreement up to very high temperatures. To reconcile different approaches we have presented normalized values $A(T)/A(0)$ as a function of normalized temperature T/T_C. A very similar scaling exponent ensures that for normalized values the results are almost the same for all models.

To finish this section, it is important to remark that the exchange stiffness value for Co FCC and HCP are similar and its scaling with the magnetization too. Besides, all the exchange stiffness scaling laws have almost the same exponent. Hence, in next sections, in which the temperature dependence of exchange stiffness parameter $A(T)$ is calculated numerically , we are going to take into account only Turek's parameter set [156] as a test to check if the CSDM prediction an Langevin dynamics simulations match and to find the temperature dependent in the whole temperature range.

4.3.6 Modeling of the temperature-dependent domain wall width

To evaluate the HCP Co exchange stiffness temperature dependence numerically in the whole temperature range we first determine the temperature dependence of the domain wall width using the Langevin dynamics simulations. We use the temperature dependence of the anisotropy from Fig 4.2 and extract the temperature-dependent exchange stiffness via the formula $\delta_{DW}(T) = \pi\sqrt{A(T)/K(T)}$

The domain wall width does not have any known scaling behaviour as the anisotropy's Callen-Callen laws. However, it can be calculated easily with the same procedure as it has been done in the subsection 4.3.4 for $T = 3K$. Using the same system size as before, which seemed to be big enough to fully contain domain walls at high temperatures, the results of the simulations are fitted to eq.(4.12) extracting the domain wall widths for each temperature. The resulting domain wall profile for two temperatures is presented in Fig. 4.4, based on the

parameters of Turek *et al* [156]. The results clearly show an increase in the domain wall width with temperature.

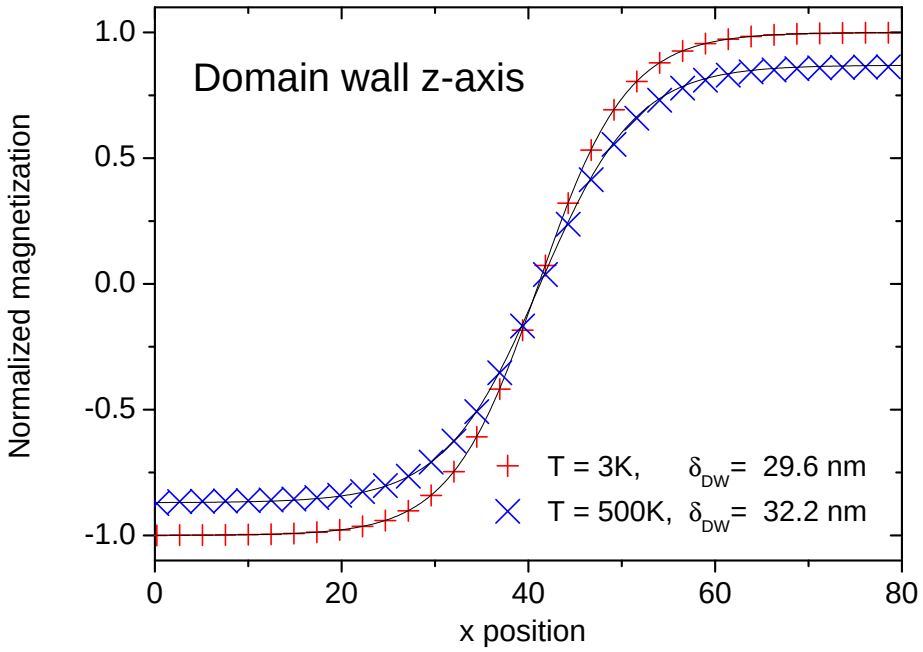

Figure 4.4: Simulated domain wall profiles (crosses) for temperatures T = 3 K and T = 500 K, using the exchange values of Turek *et al* [156] showing a reduction in the equilibrium magnetization at elevated temperature and an increase in the domain wall width from 29.6 nm to 32.3 nm. The lines shows the fitting to the domain wall profile, eq.(4.12).

Next, the resulting domain wall width temperature dependence is shown in Fig. 4.6 , demonstrating a clear increase of the domain wall width with temperature. At not too high temperatures, where the convergence of the averaged values is better, the logarithm of the domain wall width can be fitted to a power law as a function of magnetization. This way we obtained the low-temperature scaling behavior $\delta_{DW} \sim m^{-0.59}$ in both x and z directions which is shown in Fig. 4.5. The comparison of this scaling law with the domain wall width extracted from the direct simulations, shows that it correctly describes the behavior up to temperatures around 800 K, see Fig. 4.6. We stress again that we have not taken into account here the transition to FCC structure which would further increase the domain wall width with temperature.

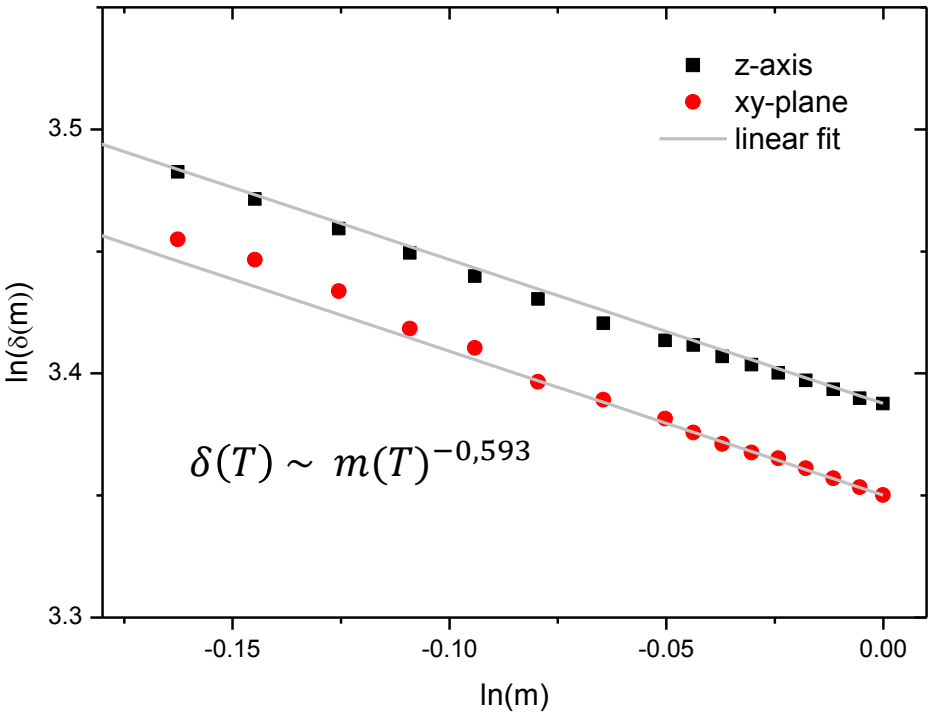

Figure 4.5: Low temperature linear fitting of the logarithm of the domain wall widths for domain walls created both in the xy plane and in z direction.

4.3.7 The temperature-dependent exchange stiffness

Once the anisotropy and domain wall width temperature dependence have been calculated it is possible to derive directly the exchange stiffness temperature dependence via the formula $\delta_{DW} = \pi\sqrt{A/K}$. The resulting exchange stiffness temperature dependence is presented in Fig. 4.7. At the same time, using the analytical scaling laws for the anisotropy and the domain wall width it is easy to calculate that the corresponding scaling law for the exchange stiffness is $A \sim A^{1.81}$ which clearly agrees with the analytical results from CSDM (section 4.3.5), shown in Table 4.3. This scaling law is depicted in Fig. 4.7 demonstrating a good agreement up to very high temperatures.

Langevin dynamics simulations 2.2.3 allows to calculate Bloch domain walls at any temperature, even close to the Curie temperature T_C. It should be remarked, however, that experimentally Co HCP has been reported to undergo a transition to the FCC structure[154] at temperatures around $T = 695K$. The dependence of

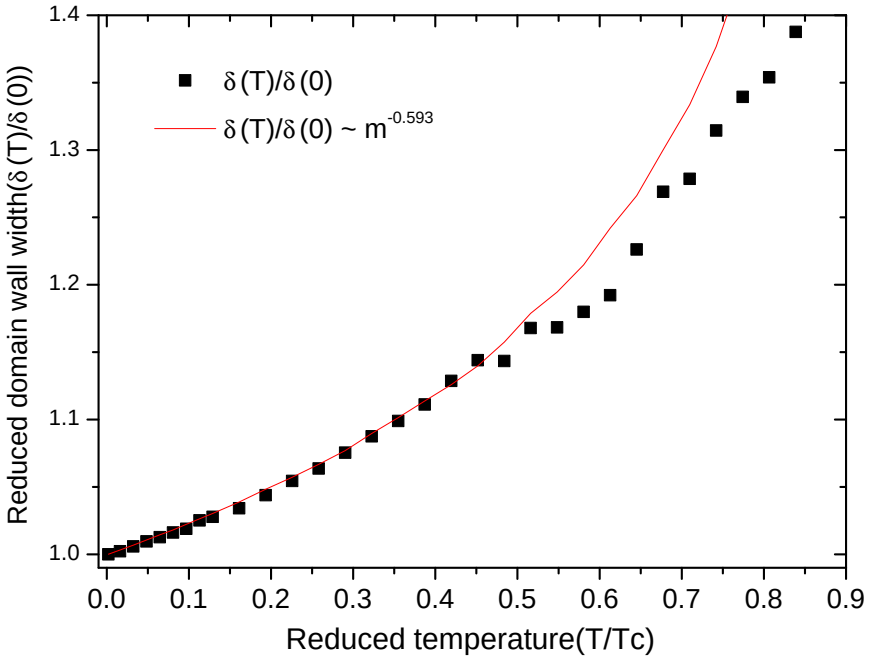

Figure 4.6: Temperature dependence of the domain wall width (normalized to T = 0 K value. The symbols indicate the data extracted from direct simulations while the line shows a low temperature scaling law with magnetization $\delta_{DW} \sim m^{-0.59}$.

the Curie temperature on the structure is expected to be small, and therefore this transition could be disregarded in relation to the exchange stiffness evaluation.

Finally, we recall that the classical Heisenberg model leads to a temperature-dependent magnetization $m(T)$ described by the Langevin function. This functional form typically is not in agreement with the experimentally measured one, particularly for HCP Co [93], which is known to be better described by the Brillouin function with S = 1/2 [39]. Thus the low and high temperature experimental and our asymptotes for $m(T)$ are significantly different. For example, at low temperatures the Langevin function gives a linear dependence on temperature, while the Brillouin function gives the well-known $1 - const(T/T_C)^{3/2}$ Bloch law. Note that in terms of the magnetization (and not temperature) the classical and quantum cases give similar behaviour [22]. To overcome the problem of the incorrect temperature dependence of the magnetization in the simulation and to make our results more useful for comparison with experiments, we a ssume that the experimentally measured magnetization obeys the Curie-Bloch relation

$m(T) = \left(1 - (T/T_C)^{\alpha}\right)^{\beta}$ with $\beta = 0.34$ and $\alpha = 2.369$ for Co [46]. We then apply temperature rescaling as suggested in Ref. [46] with the function

$$\frac{T}{T_C} = \left(\frac{T_{\text{res}}}{T_C}\right)^{\alpha} \tag{4.23}$$

where T_{res} is a new (experimental) temperature. The resulting temperature dependence of the stiffness parameter is shown in Fig. 4.7(b) taking into account the correct temperature dependence of the magnetization fluctuations.

4.4 Conclusions

In conclusion, using a multi-scale approach we have estimated the temperature dependent domain wall width and the exchange stiffness parameter in Co. We have used several parametrizations of the Heisenberg Hamiltonian available in the literature as well as our own parameterization and the parameterization of our co-worker S. Khmelevskiy.

To summarize the conclusiones extracted from this chapter:

- The low temperature values for the exchange stiffness parameter appear to be larger than the widely used ones and more consistent with upper estimation by the Brillouin scattering method [56] and even with old neutron measurements [143]
- The analytical values of the exchange stiffness A calculated from atomistic exchange parameters both for FCC and HCP are very similar if the parameter set used for each crystal structure is calculated with the same *ab-initio* method.
- The Bloch domain wall widths in xy plane and c-axis have been simulated employing the Turek's parameter set and using Langevin dynamics obtaining results in good agreement with analytical estimations of the domain wall width.
- Analytical domain wall width for HCP Co at low temperatures was found to be in the interval 24-29 nm with a slight difference between domain walls in xy plane and $c-axis$.
- By means of the theoretical CSDM and direct Langevin dynamics simulations we have found the magnetization scaling exponents for both domain wall width ($\delta_{DW} \sim m^{-0.6}$, HCP Co) and the exchange stiffness ($A \sim m^{1.8}$) parameters.

- These exponents are almost the same for different parametrizations and also for FCC and HCP Co. The agreement between direct estimations from the domain wall width and the classical spectral density method gives us confidence in our results.

These results form basis for multi-scale approach for simualting large-scale dynamics at high temperatures, based on the LLB micromagnetics. Our findings are important for both zero and high-temperature micromagnetics, as they may change the boundaries between the occurrence of different reversal modes. They could lead to markedly different results for simulations of the ultra-fast dynamics, the spin-Seebeck effect or high temperature domain wall dynamics. We stress that the multiscale approach, is essentially parameter free since all input parameters to the atomistic spin model are determined from *ab-initio* calculations. We suggest that, although our estimates of exchange stiffness are at the upper end of the spectrum of experimental values, our model calculations provide an important benchmark for the fundamental magnetic properties of Co.

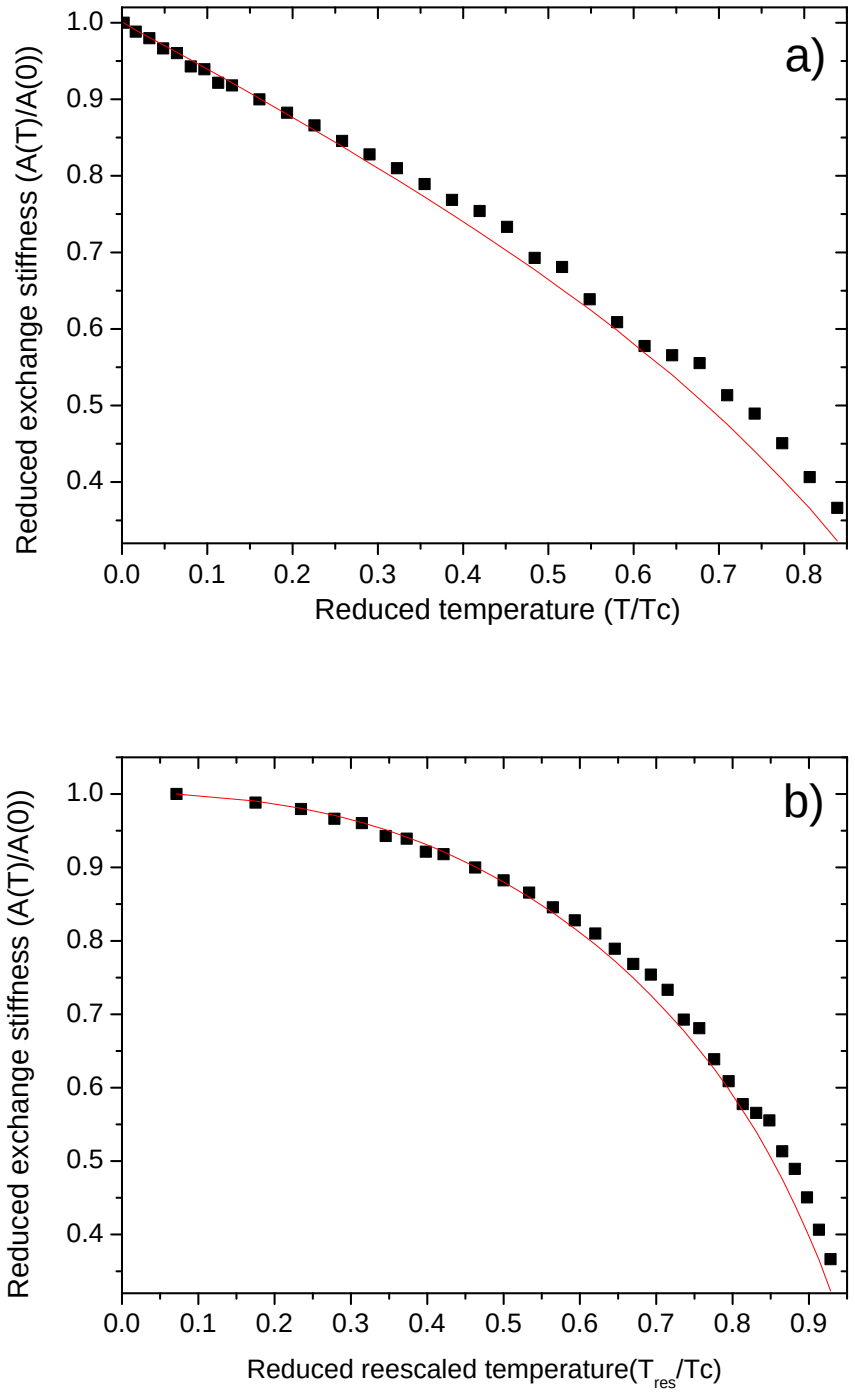

Figure 4.7: Temperature dependence of the exchange stiffness parameter from atomistic simulations and theory. The symbols indicate the data extracted from direct evaluation of the domain wall profile. The line plots the scaling relation $A(T) = A(0)m^{1.8}$. The upper panel a) represents the data obtained via the direct estimation in the classical Heisenberg model while the panel b) represents the re-scaled data according to eq. 4.23.

5

On the conditions for thermally-induced all-optical switching in ferrimagnetic alloys: modeling of TbCo.

In the last chapter, it has been presented the methodology needed to extract the temperature dependence of the micromagnetic parameters from the zero temperature atomistic magnetic parameters, and it has been applied both for Co HCP and FCC. The obtained scaling laws are inputs needed to perform LLB simulations of high temperature processes in Co based materials, such as the ultrafast magnetic response to laser heating.

However, the most interesting materials for ultrafast laser heating are ferrimagnetic materials for which all optical swichting *AOS* have been observed. For these materials is more difficult to obtain *ab-initio* exchange parameters J_{ij} due they are composed of two different materials instead of one: transition metal TM and rare earth RE. To reproduce thermal properties in these materials it is needed to calculate at least 3 atomistic exchange parameters: both ferromagnetic exchange parameters inside each sublattice and the antiferromagnetic exchange between sublattices which characterizes ferrimagnetic materials.

Usually, the ferrimagnetic materials used for *AOS* are disordered alloys which complicates the *ab-initio* calculation of atomistic exchange parameters J_{ij}. Another difficulty on the calculation of J_{ij} is the nature of rare earth RE elements, because it is needed to take into account the f electronic band on the *ab-initio* calculations. For these reasons mainly, the atomistic exchange parameters J_{ij} used in atomistic simulations for ferrimagnetic materials are fitted to reproduce experimental results.

5. ON THE CONDITIONS FOR THERMALLY-INDUCED ALL-OPTICAL SWITCHING IN FERRIMAGNETIC ALLOYS: MODELING OF TBCO.

In this chapter, it is presented an atomistic modeling of heat-assisted, all-optical switching *AOS* of disordered ferrimagnetic TbCo alloys, which is one of the most promising material for *AOS*, varying the Tb concentration, laser pulse fluence and its duration. To reproduce TbCo magnetic properties, the atomistic exchange parameters are fitted to repoduce experimental results. Our results indicate that deterministic heat-assisted AOS occurs in a wide range of Tb concentrations and at large laser fluences with pulse duration 50 fs. We furthermore demonstrate that the occurrence of the transient ferromagnetic-like state is not a sufficient condition for the heat-assisted AOS. The presence of a magnetisation compensation point or going through it is also shown not be required. With the increase of the laser pulse duration the heat-assisted AOS becomes stochastic so that for 1 ps laser pulse the deterministic heat-assisted AOS does not exist.

5.1 Introduction

In 2007 Stanciu *et al* reported that in GdFeCo disordered alloys it is was possible, not only to change, but also to reverse magnetization using circularly polarized femtosecond laser pulses [145]. This observation lead to a debate as to the origin of the helicity dependent switching. The inverse Faraday effect was originally proposed as the key driving mechanism for the reversal [11, 82, 145], however, subsequent studies have found that this type of switching requires a large number of repeated pulses, suggesting that such an effect is likely to be relatively small [44]. Furthermore, the cumulative heating effect is likely to contribute to the reversal process here where the system is driven close to the phase transition temperature.

A further complication to the debate on all-optical switching (AOS) was presented in 2012 by Ostler *et al.* where single 50fs laser pulses were shown to drive deterministic magnetization reversal for both left, right and linearly polarised light [123]. This has been verified experimentally [79, 123] in this material leading us to conclude that there are indeed two mechanisms for AOS; one that requires multiple pulses and is helicity dependent; and another that is purely thermally driven (dubbed thermally induced magnetization switching or TIMS) and requires only a single, femtosecond laser pulse.

A large amount of work in the area of AOS has been investigated in the prototypical disordered ferrimagnetic alloy GdFeCo of various compositions, using laser pulses in the regime of 10's of femtoseconds. However, there have also been a number of demonstrations of AOS in; other ferrimagnetss [10, 103]; ferromagnets [96]; and multilayer combination [48, 103, 167]. In some material systems

a *single* pulse mechanism has been demonstrated [123], whilst in others multiple pulses have been shown to be required [44]. In Refs. [123, 135] it was empirically demonstrated that a number of requirements for TIMS must be satisfied to observe the phenomena. These include; (i) two or more magnetic species with antiferromagnetic exchange; (ii) different demagnetization times; (iii) the presence or traversal of the magnetic compensation point, T_M; and (iv) ultrashort laser pulses. As well as these requirements, it was also shown in Ref. [135] that the switching in GdFeCo proceeded through a temporary alignment of the Fe and Gd sublattices, though it is not clear if the existence of this *transient* state is a requirement or merely a side effect of the switching.

In the single sub-ps pulse mechanism the first two requirements have so far been unambiguously demonstrated. More recently, however, rather long laser pulses have been used (with a single shot) to drive ultra-fast magnetisation reversal, up to 10ps [55], raising fundamental questions about the intrinsic or limiting time-scales of the underlying processes.

While GdFeCo is well studied in this respect, both experimentally [79, 98, 123, 135, 145] and theoretically [21, 123, 135, 150], TbCo has been so far mostly investigated experimentally[9, 10], motivating the need for a theoretical investigation of switching. Apart from experimental reports on AOS, TbFe has also been modelled, though mostly from the point of view of static magnetisation [69] . At the same time, both TbFe and TbCo present larger anisotropy than GdFe and thus potentially are more relevant for applications. Most of the experimental studies in TbCo have subject to switching through the use of circularly polarised laser pulses [10, 44, 103] that firmly confirmed the occurrence of AOS in TbCo, but mainly the inverse-Faraday effect has been speculated as the mechanism. In a recent experiment on TbCo [9] with a single laser pulse, TIMS has not been confirmed, and only thermal demagnetisation with subsequent formation of domains has been reported. Due to the fact that different experiments are performed in different conditions, i.e. different pulse lengths, fluences, static vs time-resolved probing, single-shot vs multiple shot laser pulses *et al*, they cannot be considered as conclusive at this point and the possibility of TIMS in TbCo is an open question. Thus, addressing this problem theoretically and finding the region of parameters for which TIMS exists, if it does, is important to guide future experiments.

In order to investigate and clarify some of the aforementioned aspects of TIMS, such as; the requirement of the presence (or traversal of) T_M; the transient ferromagnetic-like state; and the importance of the laser pulse duration, a computational study of the magnetization dynamics for $TbCo$ disordered alloys excited with ultrashort laser pulses is presented in this chapter. TbCo has

been selected here (many ferrimagnetic rare compound with RE and TM metals could exhibit TIMS) for several main reasons; firstly, it has been demonstrated experimentally that AOS can be produced with different laser pulse durations [10, 44, 103]; secondly, it is an interesting material for ultra-high density data store information [10]; and finally, the conditions for its switching under TIMS has not been investigated theoretically so far.

Specifically, here we investigate the influence of the Tb concentration x in the sample Tb_xCo_{1-x} (this will lead to an analysis of the importance of T_M point), heated by laser pulses with different durations (50fs, 400fs, 1ps, 10ps) and fluences, and seek the occurrence of subpicosecond magnetisation reversal without any external stimulus (as a magnetic field or spin polarized current). For this purpose, atomistic spin simulations of TbCo have been performed.

5.2 Theoretical background

5.2.1 Mean-field model as a fitting tool for exchange parameters.

The mean-field approximation (MFA) [149] allows calculating atomistic exchange parameters J_{ij} for ferromagnetic materials, from its experimental Curie temperature (T_C) and its atomic structure, what is very useful to model a material if an *ab-initio* parameterization is not available. Thus, the calculated J_{ij} can be used in Langevin dynamics to perform atomistic simulations for that material, such as, calculating the hysteresis loop the ultrafast demagnetization with laser pulses or the magnetization versus temperature curve.

Nevertheless, the calculated exchange parameters with mean-field cannot be used directly in Langevin dynamics (section 2.2.3) or Constrained Monte Carlo method (section 2.2.4) because they must corrected by a factor ϵ. For example, using directly these parameters in Langevin dynamics gives a slight difference in T_C, which means that the system is not modeled correctly. This factor depends on the atomic structure and on the exchange interaction term considered in the model[1]. It comes from spin wave correlations effects its derivation as well as the different values corresponding to each case are presented in [50]. The explicit case for ferromagnets in atomistic spin dynamics simulations is summarized in [46].

Besides, the mean-field approximation only calculates first neighbour exchange parameters, but it is well known that the exchange interaction is long range. Mean-field approach renormalize the exchange interaction to first neighbours.

[1]In this thesis, it is always considered a three dimensional Heisenberg Hamiltonian with $S = \infty$ (see ref. [50])

Strictly speaking, using only first neighbor exchange interactions in Langevin dynamics is not correct, because lot of long range effects are not taken into account, and these long range effects could influence the magnetization dynamics of the system. However, in the absence of a *ab-initio* parameterization, exchange parameters fitted with the mean-field approach are the best solution to model a material.

In practice, given a T_C value and an atomic structure, the corresponding exchange parameters for a ferromagnetic material, valid for atomistic spin simulations[1], are calculated with the following equation

$$J_{ij} = \frac{3k_B T_C}{z\epsilon} \tag{5.1}$$

Where J_{ij} are the first neighbor atomistic exchange parameters, k_B is the Boltzmann constant, T_C is the Curie temperature of the material, z is the coordination number of the atomic structure[2] and ϵ is the spin-wave correction needed reconcile mean-field and Langevin dynamics estimations of T_C.

In the case of ferrimagnetic materials, this approximation is no longer helpful. Firstly, because there are two sublattices which magnetization vanishes at the same T_C. Assuming the same atomic structure for both sublattices (equal z), what is normally done in atomistic spin simulations, implies that the atomistic exchange parameters calculated via eq. 5.1 are the same. However, it is well known that they have different exchange parameters for several reasons, for example, the existence of a compensation point (T_M) in some ferrimagnetic materials or the different demagnetization times observed in AOS experiments. Secondly, the commom value of T_C for both sublattices arises from the antiferromagnetic coupling between the transition metal (TM) and the rare earth (RE) sublattices, which characterized ferrimagnetic materials. This antiferromangetic interaction cannot be determined using the previous mean-field version.

To get equations useful to model ferrimagnetic materials it should be taken into account in MFA the existence of two sublattices coupled antiferromagnetically [15, 105, 106, 124]. This leads to a system of coupled Curie-Weiss equations which describes the magnetization of both sublattices.

$$m_{RE} = B(\xi_{RE}); \qquad m_{TM} = B(\xi_{TM}) \tag{5.2}$$

Where $B(\xi_i) = coth(\xi_i) - 1/\xi_i$ is the Langevin function with $i = TM, RE$. The normalized magnetization of the sublattice i is m_i, and $\xi_i = \mu_i H_i^{MFA}/k_B T$ with the corresponding effective fields (H_i^{MFA}) written as

[1] These exchange parameters have been already corrected with ϵ

[2] Is the number of first neighbors of any atom.

5. ON THE CONDITIONS FOR THERMALLY-INDUCED ALL-OPTICAL SWITCHING IN FERRIMAGNETIC ALLOYS: MODELING OF TBCO.

$$\begin{aligned} H_{TM}^{MFA} &= \left(xJ_{0,TM-RE}m_{RE} + qJ_{0,TM-TM}m_{TM}\right)/\mu_{TM} \\ H_{RE}^{MFA} &= \left(xJ_{0,RE-RE}m_{RE} + qJ_{0,RE-TM}m_{RE}\right)/\mu_{RE} \end{aligned} \tag{5.3}$$

Where x is the RE concentration, $q = 1 - x$ is the TM concentration, k_B is the Boltzmann constant, $J_{0,TM-TM}$ is the total[1] exchange interaction of the TM sublattice, $J_{0,RE-RE}$ is the total exchange interaction of the RE sublattice and $J_{0,RE-TM} = J_{0,TM-RE}$ is the total exchange interaction between the RE and TM sublattices.

To calculate the T_C from eq. 5.2 it must be pointed out that at temperatures close to T_C, ξ tends to zero. Thus, the Langevin function is expanded as $B(\xi) \approx \xi/3$ and the Langevin function reads

$$\begin{aligned} T_C(x)^{MFA} &= \frac{2a}{3k_B b}\frac{1}{\sqrt{1 + 4a/b^2} - 1} \\ &= \frac{b}{6k_B}\left(1 + \sqrt{1 + \frac{4a}{b^2}}\right) \end{aligned} \tag{5.4}$$

with

$$a = qx\left(J_{0,TM-RE}^2 - J_{0,RE-RE}J_{0,TM-TM}\right),$$

$$b = qJ_{0,TM-TM} + xJ_{0,RE-RE}$$

$J_{0,TM-TM}$ and $J_{0,RE-RE}$ are calculated from eq. 5.1 for each corresponding ferromagnetic bulk T_C . This ensures that eq. 5.4 gives the correct values of T_C in the extremes $x = 0$ and $x = 1$[2]. For this reason, $J_{0,TM-TM}$ and $J_{0,RE-RE}$ are renamed as $J_{0,TM-TM}^{bulk}$ and $J_{0,RE-RE}^{bulk}$ respectively. Using the calculated $J_{0,TM-TM}^{bulk}$ and $J_{0,RE-RE}^{bulk}$ parameters, the antiferromagnetic exchange $J_{0,RE-TM}$ is fitted matching the experimental data of the compensation point dependence on the rare earth concentration ($T_m(x)$) with the compensation point that eq. 5.2 give as a solution.

In principle, with these three exchange constants fitted, it is possible to model a ferrimagnetic material, but sometimes it is observed that experimental T_C values for intermediates compositions are smaller than the calculated with the mean-field model exchange parameters. This discrepance is attributed to the fact that mean-field approach only calculate first neighbors exchange paramaters. Because of the exchange parameters for the TM are obtained from its bulk T_C, it is not taken

[1] To be noted that total means that $J_{0,TM-TM}/z = J_{ij}$

[2] At low concentrations of Rare earth elements eq. 5.1 is recovered.

into account that in ferrimagnetic materials it could exist an antiferromagnetic exchange between the TM sublattice due the presence of RE elements [9, 59, 105, 152]. To model this effect, another exchange interactions is included in the mean-field approach which only appears in the presence of RE ($J_{0,TM-Re-TM}$). The way this interaction is included in MFA is substituing the total bulk exchange interactions for the transition metal by an effective one ($qJ^{eff}_{0,TM-TM}$) which reads.

$$qJ^{eff}_{0,TM-TM} = qJ^{bulk}_{0,TM-TM} - xJ_{0,TM-Re-TM} \tag{5.5}$$

5.3 Modelng results

5.3.1 The Spin Hamiltonian parameterization

In order to investigate the spin dynamics of Tb_xCo_{1-x} [1] under the influence of ultrafast laser heating, proper materials parameters must be determined both for Langevin Dynamics (section 2.2.3) and for the two temperature model (section 2.4). This section deals with parameterization of the atomistic hamiltonian of Langevin dynamics.

The material parameters used for modeling Tb_xCo_{1-x} are presented in Table 5.1, with exception of the exchange parameters which must be calculated from the experimental data of both Curie temperature and compensation point. A different anisotropy constant was used for Co and Tb in order to mimic the change of anisotropy as a function of Tb concentration, reported in Ref.[10] although we stress that the anisotropy does not play any role in the ultra-fast switching. These values have similar magnitudes as published in Ref.[10]. The value of damping was chosen to give the magnetisation quenching magnitudes similar to observed in Ref.[9]. The magnetic moments and the gyromangetic factor are taken from literature.

gyromagnetic factor ($\frac{rad}{T \cdot s}$)	γ	$1.76 \cdot 10^{11}$ [162]
Damping constant	λ_{Co}	0.05
	λ_{Tb}	0.05
Magnetic moment(μ_B)	μ_{Co}	1.61 [149, 165]
	μ_{Tb}	9.34 [43]
Anisotrpy constant($J/atom$)	$k_{\mathrm{u}}(Co)$	$3.73 \cdot 10^{-23}$
	$k_{\mathrm{u}}(Tb)$	$2.16 \cdot 10^{-22}$

Table 5.1: Modeling parameters used in atomistic spin simulations for $TbCo$

[1] In this work, it is considered a disordered alloy, with Tb concentration x

5. ON THE CONDITIONS FOR THERMALLY-INDUCED ALL-OPTICAL SWITCHING IN FERRIMAGNETIC ALLOYS: MODELING OF TBCO.

As it was done for $GdFeCo$ in [124], the exchange parameters for Tb_xCo_{1-x} are fitted from the experimental values of the Curie T_c and magnetization compensation T_M temperatures presented in [10], using the mean-field approximation (section 5.6). As a first step, the bulk exchange parameters for Co ($J^{\text{bulk}}_{\text{Co–Co}}$) and Tb ($J^{\text{bulk}}_{\text{Tb–Tb}}$) corresponding to each bulk Tc (1385K [120] and 237K [153], respectively) [1] have been calculated using eq. 5.1 .

Using $J^{\text{bulk}}_{\text{Co–Co}}$ and $J^{\text{bulk}}_{\text{Tb–Tb}}$, the antiferromagnetic interaction ($J^{\text{bulk}}_{\text{Co–Tb}}$) is fitted, matching the compensation point results obtained of solving eq. 5.2, with the experimental data, for different concentrations available in [10].

However the obtained Curie temperatures for the different concentrations of Tb (x), are much higher than those measured experimentally measured. Therefore, to reduce the calculated value of T_C, it is needed to consider an extra antiferromagnetic interaction in Co sublattice, that appears in the presence of Tb ($J_{\text{Co–Tb–Co}}$). The way in which this interaction is introduced in eq. 5.2 is substituing $J^{\text{bulk}}_{\text{Co–Co}}$ for an effective one $J^{\text{eff}}_{\text{Co–Co}}$ that depends on $J^{\text{bulk}}_{\text{Co–Co}}$, $J_{\text{Co–Tb–Co}}$ and x. Thus, the effective exchange parameter on the Co site reads ($x < 0.5$)

$$J^{\text{eff}}_{\text{Co–Co}} = J^{\text{bulk}}_{\text{Co–Co}} + J_{\text{Co–Tb–Co}} \cdot \frac{x}{1-x} \tag{5.6}$$

By systematic variation of the two parameters, $J_{\text{Co–Tb}}$ and $J_{\text{Co–Tb–Co}}$, we can reproduce the experimental dependence of $T_M(x)$ and $T_C(x)$ for all x, see Fig. 5.1 and Fig. 5.2. The corresponding exchange interaction parameters are used in the atomistic code and are presented in Table I.

Exchange interaction type	Energy (Joules)
$J^{\text{bulk}}_{\text{Co–Co}}$	$5.9 \cdot 10^{-21} J$
$J^{\text{bulk}}_{\text{Tb–Tb}}$	$8.2 \cdot 10^{-22} J$
$J_{\text{Co–Tb}}$	$-1.0 \cdot 10^{-21} J$
$J_{\text{Co–Tb–Co}}$	$-4.4 \cdot 10^{-21} J$

Table 5.2: Exchange parameters for $TbCo$, extracted by systematic variation of the Co-Tb and Co-Tb-Co parameters and comparing the T_C and T_M values with experimental measurements as a function of the concentration of Tb, x in the Tb_xCo_{1-x} alloy.

As discussed in Ref. [10], there exist three different regions for the position of T_{M} relative to room temperature $T_{\text{room}} = 300K$. The first one corresponds to

[1] Although we are dealing with a disordered allow, Tb_xCo_{1-x} has been supposed to have a FCC atomic structure, with a x concentration of Tb atoms ramdonly distributed. Thus, $z = 12$ and $\epsilon = 0.79$ in eq. 5.1.

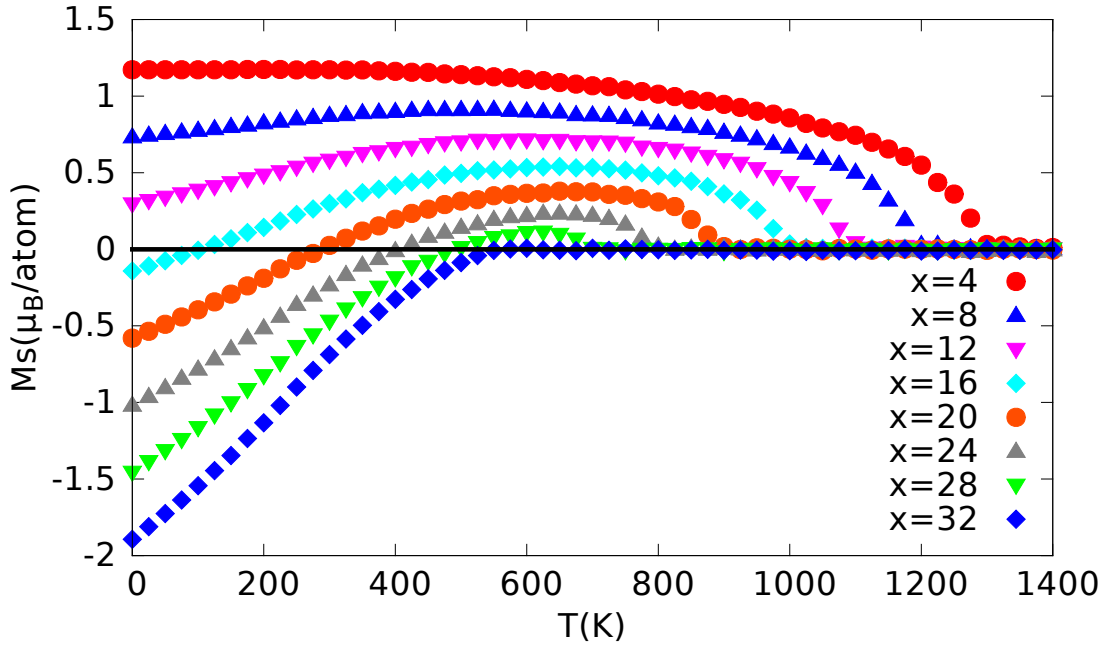

Figure 5.1: Total magnetization of Tb_xCo_{1-x} for different concentrations x of Tb. It has been calculated with Langevin dynamics (2.2.3), using as input, the fitted exchange parameters via MFA, shown in Table 5.2.

concentrations in the region from $x = 0.04$ to $x = 0.2$ where T_{M} is below T_{room} or does not exist due to the shortage of Tb. Thus the transient temperature of the electronic bath will not cross T_{M} upon laser heating. The second one ranges from $x = 0.2$ to $x = 0.3$ and T_{M} is above T_{room} so that the electronic temperature may cross T_{M} upon application of the laser pulse, depending on the fluence. The third region begins at the Tb composition $x = 0.3$ where the compensation temperature T_{M} does not exist due to an excess of Tb. Considering this distinction, the role of T_{M} in the occurrence of AOS will be determined in the following.

5.3.2 Two temperature model parameterization.

In order to model the laser heating of the sample and the electronic temperature dynamics, the two-temperature model (2TM) is used. The pump energy is described using an exponential profile in time that allows us to vary the pulse duration of the laser. The 2TM reads:

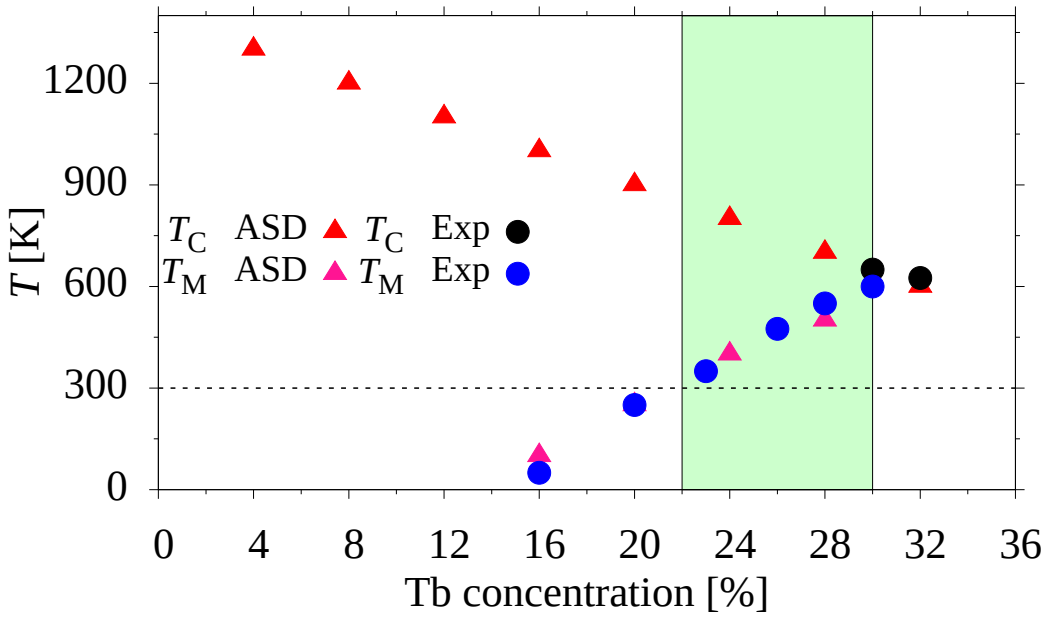

Figure 5.2: Curie temperature, T_{C}, and the compensation temperature, T_{M}, as a function of Tb concentration, x. Triangular points (▲/▲) symbols represent the results from atomistic spin dynamics (ASD) simulations with the parameters from Table I. Circles (●/●) represent the experimental values extracted from Ref. alebrand. As the simulations begin at room temperature the white background is the concentration region where T_{M} is not reachable with the laser heating.

$$\begin{aligned} C_e \frac{dT(t)_e}{dt} &= -G[T(t)_e - T(t)_{ph}] + P(t) \\ C_p \frac{dT(t)_p}{dt} &= G[T(t)_e - T(t)_{ph}] \\ P(t) &= (I_0 \cdot F) e^{(-t/\tau_p)^2} \end{aligned} \tag{5.7}$$

Here $T_e(t)$ is the electronic temperature, $T_{ph}(t)$ is the phononic temperature, $C_e = \gamma T_e$ and C_p are the heat capacities for electrons and phonons and G is a coupling parameter between these systems. In the simulations we have used the following parameters taken from Ref [123] for $GdFeCo$: $\gamma = 7.00 \cdot 10^2 Jm^{-3}K^{-2}$, $C_p = 3.0 \cdot 10^6 Jm^{-3}K^{-1}$ and $G = 17 \cdot 10^{17} Wm^{-3}K^{-1}$. P(t) is assumed to be the absorbed pump laser energy received by the electronic system, I_0 describes the amount of laser energy absorbed by the sample, F is the laser fluence and τ_p described the laser pulse duration. More specifically, the atomistic simulations use the value $(I_0 \cdot F)$ characterising the input energy (units of $J/(m^3 \cdot s)$), where

F is the laser fluence while the experimental papers report the values in terms of F (units J/m^2). The estimation of I_0 is non-trivial and the result of the simulations are strongly dependent on F. I_0 can be estimated from theory or experimental reflectivity, and has the units of $1/m \cdot s$. In this paper and because the experimental data are not available, its value has been taken from literature for FePt ($I_0 = 3 \cdot 10^{19} 1/m \cdot s$) [108] giving the laser pulse fluency in agreement with the experimental data on TbCo. We note that the results, whilst dependent on I_0, will be simply re-scaled should a different value be used. This shows that this value although arbitrary is close to the real one for ultra-thin metallic films. In the present work the simulations always start at room temperature, $T_{\text{room}} = 300K$.

5.4 Results

Fig. 5.3 presents an example of simulated magnetisation dynamics, in this case for $Tb_{32}Co_{68}$ and laser pulse duration τ_p = 50 fs. Note that this material does not have a magnetisation compensation point. Our modeling qualitatively reproduces the experimental forms of the magnetisation quenching/recovery and switching curves [9]. As expected, for small laser fluence (Fig. 5.3a) magnetisation quenching and subsequent recovery takes place. For laser fluencies above ca. $F = 18.5 mJ/cm^2$ the magnetisation of the sublattices switches going through a small transient ferromagnetic-like state (Fig. 5.3c). We have investigated the fluence limit for which the switching starts to appear (see Fig. 5.4) finding that near the threshold value the magnetization can reach the transient ferrimagnetic state and temporarily switch, however the backward switching to the initial directions of the sublattices occurs, see Fig. 5.3b. This indicates that the occurrence of the transient ferromagnetic-like state is not a sufficient condition for switching. This form of the curve is similar to the experimentally measured for TbCo[9] and TbFe[80]. High laser power simply demagnetises the sample as shown in Fig. 5.3d.

In Fig. 5.4 we present quantitatively the degree of magnetisation quenching for the z-component of the Co sublattice magnetization after 10ps, for different durations of the pulse (50fs, 400fs, 1ps), and various compositions. In this figure, 100% quenching corresponds to demagnetization. Switching is represented as a magnetisation quenching larger than 100%. The green shaded region represents deterministic switching (see below). A similar representation was used in Ref. [9]. The choice of compositions corresponds to $Tb_{16}Co_{84}$ (▲) with $T_M < T_{\text{room}}$, $Tb_{24}Co_{76}$ with $T_M > T_{\text{room}}$ (■) and $Tb_{32}Co_{68}$ (●) without a compensation point. The pump fluence in Fig. 5.4 has very different energy scales due to the fact that as the laser pulse duration is increased, the total energy absorbed in the

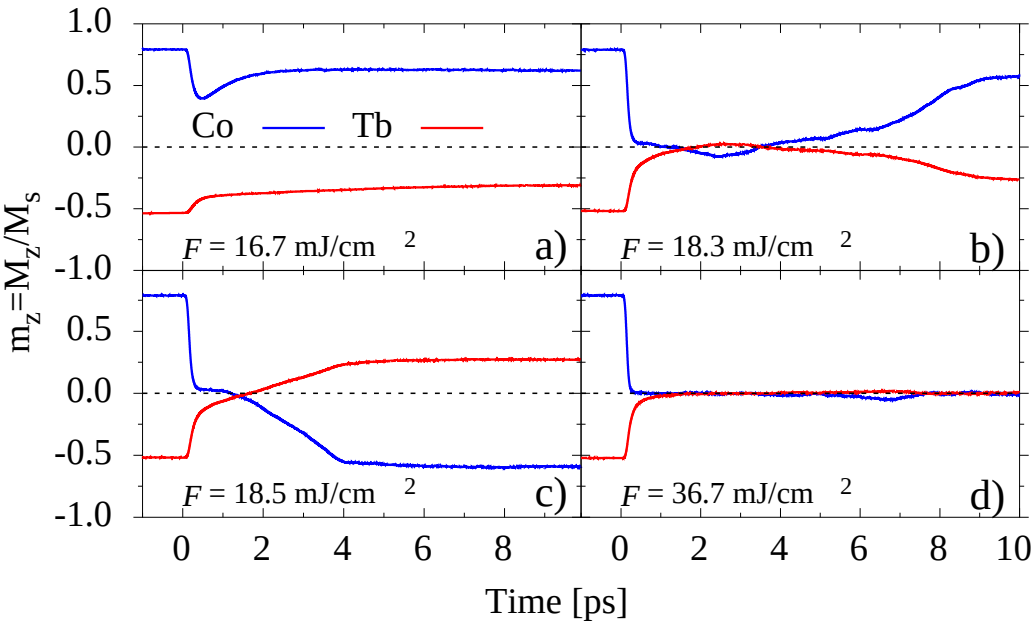

Figure 5.3: Different magnetization dynamics curves corresponding to various pump fluences for $Tb_{32}Co_{68}$ and a pulse duration of 50 fs. The reduced magnetization $m_z=M_z/M_s$, is the magnetization of the individual sublattice divided by the value of that sublattice if all spins were ordered (the zero K case).

system is also increased and thus less laser fluence is necessary to produce the same demagnetization. We can also see that as the Tb concentration increases, the degree of quenching is reduced. Simulations show TIMS existence for all temporal widths of laser pulse, though it can be seen from Fig. 5.4 that as the pulse becomes shorter, the range of compositions and laser fluences with TIMS becomes larger.

We should point out explicitly that for a laser pulse duration of 50fs, all compositions shown in Fig. 5.4 switch. Since the composition $Tb_{32}Co_{68}$ does not have a magnetisation compensation point, this demonstrates that the occurrence of the compensation temperature is not a necessary condition for TIMS. Our simulations show that the composition $Tb_{12}Co_{88}$, also without the compensation temperature, presents TIMS as well. Furthermore, for the 50fs laser pulse duration, the range for TIMS also includes $Tb_{16}Co_{84}$, for which T_M is below T_{room}. Thus, going through this point is also not a necessary condition for the AOS. However, whilst we have demonstrated that T_M is not an essential criteria for switching, the results so far do not confirm that it is an irrelevant parameter in the occurrence of AOS. In fact, since we clearly observe that the composition

$Tb_{16}Co_{84}$ required more laser energy to switch, the presence of T_M influences the switching process. Furthermore the composition with a compensation temperature higher than room temperature (crossed by the electronic temperature under the action of the laser pulse), i.e. $Tb_{24}Co_{76}$, is the only one that undergoes switching for all laser pulse durations.

Finally, for $Tb_{32}Co_{68}$ and a laser pulse with a 400 fs duration (Fig. 5.4b), TIMS takes place in a small window of pump fluence, ending with a simple demagnetization at large fluences. There is also a random event of switching at small laser pulse fluency (4 mJ/cm^2). This indicates a possible stochasticity of the switching in this case which we will investigate in the following. To this end, in Fig. 5.5, we show the reversal probability as a function of laser pulse fluence, with the averaging of many realizations with different seeds for the random number generator that is used for the fluctuating stochastic field. The data are shown for various Tb concentrations and for 50fs and 400fs laser pulses. The figure shows that for 50 fs laser pulses, deterministic TIMS in a wide range of Tb concentrations (x) is possible, with stochastic switching taking place around this region. The deterministic region is very small for the 400fs laser pulse duration and does not exist for 1 ps laser pulses (not shown). This confirms that a fully deterministic TIMS only happens when the laser pulse duration is of the order of the characteristic time of the exchange interactions. For 50 fs laser pulses the deterministic region includes Tb concentrations above 30% for which T_M does not exist. The same is true for Tb concentrations $x < 0.2$ for which T_M is below T_{room} and thus it is not crossed during the heating process. Note that both the stochastic switching and complete demagnetization lead on larger timescale to the formation of magnetic domains, see previous modeling [119]. In the case of the stochastic switching parts of the system switch and others do not, leading to the formation of domains. In the case of the complete demagnetization, the system recovers by means of creation of such domains. The domain sizes in the latter case are smaller than in the former case which can be larger than the laser spot as is discussed in Ref [44].

We should note that for GdFeCo, pulses, longer than 1ps, have been used to induce switching [55, 158]. Though, in the work of Gorchon *et al.* [55] an electical stimulus rather than an optical one was used and it remains an open and interesting question as to whether the same thermally induced stimulus is at work here. Using similar modeling as presented here, switching in GdFeCo via TIMS can be induced using laser pulses up to 1ps [122], though the main reason for the difference with the present work is that in GdFeCo the damping constant is lower, which has the effect of *slowing down* the dynamics. The low damping constant is the result of the fact that the orbital angular momentum quantum

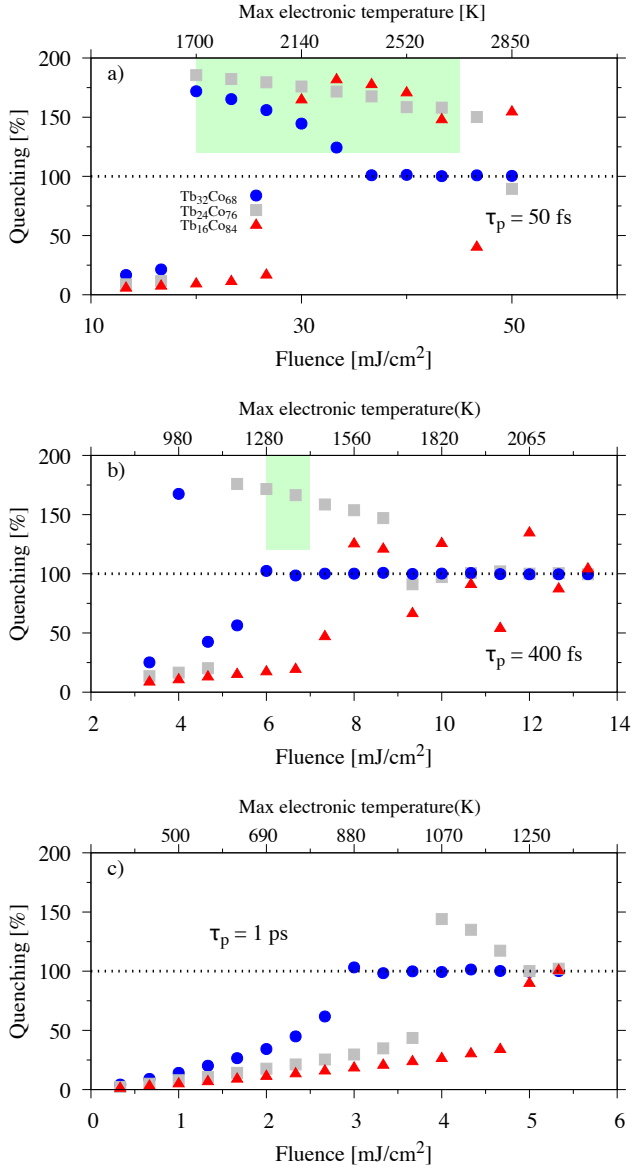

Figure 5.4: Degree of magnetisation quenching (z component) of the reduced magnetization (m_z) of Co 10ps after the pulse for different compositions of TbCo, pump fluences, and laser pulse durations a) 50 fs b) 400fs c) 1 ps. The green color indicates approximately the region with deterministic reversal.The numbers in the upper horizontal axis indicate maximum electronic temperature achieved in the integration of the $2T$ model.

number $L = 0$ for Gd f-electrons which constitutes the main difference between Gd-based and Tb-based alloys.

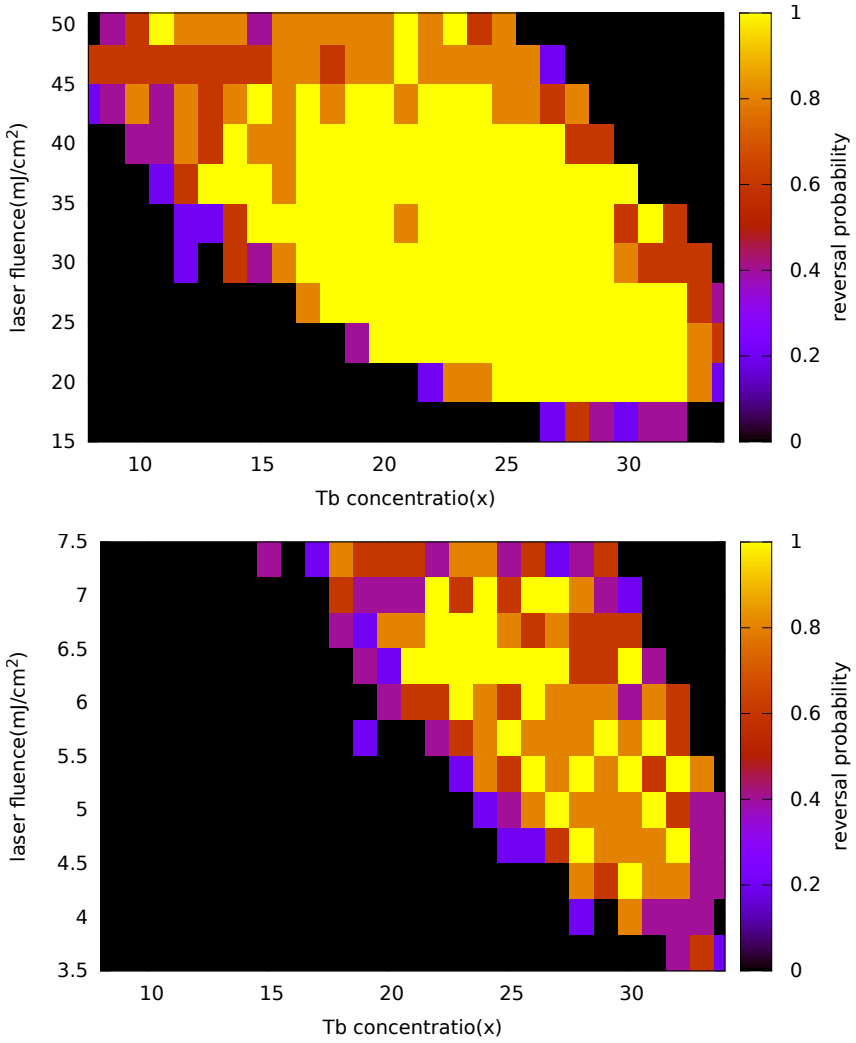

Figure 5.5: Reversal probability for Tb_xCo_{1-x} alloys heated with different laser pump fluences. The color legend indicates the reversal probability with yellow and black pixels reflecting the cases where magnetization always reverse or always not, respectively. Clearly, the intermediate colors reveal regions with stochastic reversal. Upper and lower panels correspond to 50fs and 400fs laser pulse durations, respectively.

5.5 Conclusions

In conlusion, we have modeled the ultra-fast magnetisation dynamics in Tb_xCo_{1-x} ferrimagnets varying the Tb concentration, laser pulse fluence and laser pulse duration. In this procedure, we have found the region of parameters for which TbCo switches, shedding light on previously believed *rules* for TIMS.

5. ON THE CONDITIONS FOR THERMALLY-INDUCED ALL-OPTICAL SWITCHING IN FERRIMAGNETIC ALLOYS: MODELING OF TBCO.

To summarize the conclusions extracted from this chapter:

- The inclusion of additional antiferromagnetic exchange on Co sites, with the strength proportional to Tb (consistent with the assumption of the previous works [9, 59, 105, 152]) concentration has allowed us to reproduce the experimental Curie temperatures and the magnetization compensation points, the key factor for comparison with the experiment.

- Our results indicate that the deterministic TIMS occurs for the 50fs laser pulse duration in a range of Tb concentrations and high laser pump fluences. At the boundaries for this switching TIMS is stochastic.

- Our results show that the regions for TIMS decrease with the increase of laser pulse duration and the TIMS becomes a stochastic phenomenon. Thus, the TIMS in the sense found in GdFeCo in Ref.[123, 135] occurs for laser pulses with durations on the timescale of the exchange interactions.

- We believe that the AOS found in Refs.[9, 44] with 400 fs and 10 ps laser pulses most probably does not have a complete heating origin.

- We have observed that the occurrence of the transient ferromagnetic-like state is a necessary but not a sufficient condition for the switching since with the laser power at the switching boundary, we present examples where this state occurs but the system switches back.

- We also confirm that the existence of the magnetisation compensation point is not necessary for switching, nor is it necessary to go through it during the laser pulse heating, since for both cases we have presented counter-examples. These results are in agreement with the experiments on TbFe [80].

In our view, in this case, similar to FePt [96], the inverse Faraday or MCD effect produces an asymmetry in the nucleation of TIMS and stabilize the stochastic reversal producing a deterministic AOS with many laser pulses. The reason that the TIMS has not been found so far in TbCo with a single fs laser pulse may reside in the fact that it requires high laser intensities. Indeed, comparing with the results of Ref.[44], our threshold values are at the boarder of the largest experimental ones.

Finally, we note that the complete set of conditions for the TIMS is still elusive, probably because too many parameters play a role at the same time. We believe that in the present work we have made a step forward in this respect

by establishing that (i) different demagnetising rates of the materials and (ii) femtosecond laser pulse durations are necessary conditions. At the same time (i) the presence of the magnetisation compensation point or heating through it is not a necessary condition for switching and (ii) the transient ferromagnetic-like state is not a sufficient condition.

Acknowledgement

This work was supported by the Spanish Ministry of Economy and Competitiveness under the grants MAT2013-47078-C2-2-P and by the European Community's Seventh Framework Programme (FP7/2007-2013) under grant agreement No. 281043, FEMTOSPIN. T. A. Ostler acknowledges the Marie Curie incoming BeIPD-COFUND fellowship program at the University of Liège.

5. ON THE CONDITIONS FOR THERMALLY-INDUCED ALL-OPTICAL SWITCHING IN FERRIMAGNETIC ALLOYS: MODELING OF TBCO.

6

Heat-induced spin dynamics simulation on Laves phases

6.1 Introduction

Although all optical swichting (AOS) has been also observed in ferromagnetic compounds such as $FePt$ [108] or $CoPt$ [96], it seems to be clear that ferrimagnets are still the main candidates for investigating new materials. The known materials which show AOS are, in general, ferrimagnetic disordered alloys such as $GdFeCo$ [123] or $TbCo$ [10], however, for the case of $TbFe$ disordered alloys, AOS has not been observed yet [80]. In addition, AOS has been also found in ordered structures such as antiferromagnetically coupled multilayers [103]. For the AOS specific case of producing magnetisation reversal with only one laser shot, which is dubbed thermally induced magnetisation swichting ($TIMS$), only disordered ferrimagnetic materials such as Gd_xFeCo_{1-x} [55, 123, 158, 164] have shown this effect both theoretically and experimentally.

In the previous chapter, we have investigated, using atomistic spin dynamics simulations ASD, Tb_xCo_{1-x} instead of Gd_xFeCo_{1-x}. Although for Tb_xCo_{1-x} disordered alloy, the AOS helicity dependent effect has been demonstrated experimentally using multiple laser pulses [10], $TIMS$ has not been observed yet [9]. However, the results of the atomistic spin simulations performed in chapter 5, show that the possibility of finding $TIMS$ exits, for some fluence range. In addition, the ultrafast magnetisation reversal has been obtained, apart from the typical RE concentrations around $x = 0.24$, even for very high Tb concentrations of $x = 0.33$ for which the material does not have a compensation point. In the case of Gd_xFeCo_{1-x}, $TIMS$ has been also demonstrated for high Gd concentrations [21].

6. HEAT-INDUCED SPIN DYNAMICS SIMULATION ON LAVES PHASES

Ferrimagnetic materials with the composition ($ReTm_2$)[1] crystallize in a LAVES PHASE C15 atomic structure [49]. This leads to the possibility of studying the ultrafast laser heating effect on ferrimagnetic crystalline structures, with a RE concentration of x = 0.33, which is a feasible concentration to produce $TIMS$ both in Gd_xFeCo_{1-x} and Tb_xCo_{1-x} disordered alloys.

In disordered alloys, the exchange field that affects each atomic spin is different, because the number of neighbors of the same specie for each atom is random[2]. Thus, the magnitude of the atomic exchange field may vary widely from spin to spin, and this feature might influence the ocurrence of $TIMS$. In crystalline structures, the number of neighbors of each specie is fixed as the total number of the neighbors is. Therefore, the atomic exchange field will not vary widely, and just rotations of the atomic spins could make the difference between the exchange fields that affect each spin.

In the present chapter the exchange parameters are not fitted from any experimental Curie temperature (T_C) and compensation point (T_M) as it was done in the previous chapter. Instead of this, *ab-initio* methods offer the possibility to evaluate properly exchange interactions for the LAVES PHASE C15. In this chapter, we have used an *ab-initio* long range exchange parameterization of the Heisenberg hamiltonian obtained by our co-worker S. Khmelevskyi for Laves C15 phases of two different materials: $GdFe_2$ and $TbFe_2$.

Since *ab-initio* parametrization did not produce materials which exhibit AOS, next we decided to consider variable exchange parameters up to first neighbors. This parameterization, in principle, does not represent any real $ReTm_2$ material although we stress that a large number of these compounds could exist [49]. Nevertheless, considering the exchange interactions as variables, allows us to study the influence of the exchange interactions on the ocurrence of $TIMS$ which is valuable for design of materials exibiting AOS (TIMS).

Atomistic spin simulations of $GdFe_2$ with a LAVES PHASE C15 atomic structure has been already studied by Wienholdt *et al* [163], showing the possibility of producing thermally driven swichting. The exchange parameters were evaluated by ab-initio although the antiferromagnetic exchange parameter was finally used as a fitting parameter to reproduce experimental magnetisation compensation point of disordered alloys. A spin resolved Hamiltonian used in this work included a separate treatment of $4f$ and $5d$ electrons putting a localized spin on each of subsystems. It was concluded that an exchange interation between $4f$ and $5d$ spins in Gd is sufficient condition to produce magnetisation reversal.

[1] Re = rare-earth, Tm = transition material.

[2] The total number of neighbors is the same, but the number of RE or Tm neighbors is random

We remark that all our experience as well as many of the previous simulational works [123, 135, 167] show that a separate treatment of $4f$ and $5d$ system is not necessary to observe the TIMS. There is also a large recent controversy in the literature cite related to the possibility of $4f$ and $5d$ spin systems of Re metal to have a different dynamics at the ultrafast timescale. The main differences with our work, apart from that we also calculate $TbFe_2$, is that we do not consider an intra-exchange interaction in Gd, we focus in the importance of the exchange interaction values on different atomic sites with the aim to observe $TIMS$.

This chapter starts with a brief explanation of the Laves phase C15 atomic structure because this structure is more complex than typically used in atomistic spin simulations. After this short introduction of the atomic structure, we discuss the *ab-initio* exchange parameterization and the corresponding modeling results for ultrafast dynamics. Since no TIMS is observed we proceed with the material engineering by varying the exchange parameters on Laves phases.

6.2 Theoretical backgorund

6.2.1 C15 Laves phase

The Laves phase C15 atomic structure has a composition AB_2 with A atoms disposed in diamond structure and B forming tetrahedras around A atoms. Thus, Laves phase C15 presents a 33% composition of A atoms and the corresponding 66% of B atoms[1]. It is a cubic structure which has 24 atoms per unit cell and its space group is Fd3m (labeled 227). Fig. 6.1 shows a Laves phase C15 unit cell in which A and B atoms are represented as white and blue spheres respectively.

In the Laves phase C15 unit cell represented in Fig. 6.1 there are more than 24 atoms because some of then correspond to the adjayacent unit cells. The 16 blue spheres (B atoms) belong to the unit cell, also the 4 white spheres (A atoms) inside the unit cell and finally, 3 of the atoms placed in the sides and 1 in the corner (like in a FCC unit cell) complete the 24 atoms. Setting the origin of the coordinates axes in the atom labeled as 1 in fig 6.1, the 24 atomic positions of the atoms belonging to the unit cell are presented in Table 6.1 in units of the lattice parameter a.

As the Laves phase C15 unit cell is cubic, to create a bulk system, it is only needed to replicate the unit cell over the lattice vectors of a simple cubic (SC) Bravais lattice. Thus, if it is done properly, the number of neighbors of each atom

[1]To be noted that, for a ferrimagnetic material with a Laves phase C15 atomic structure, A (white) and B (blue) atoms correspond to Re and Tm atoms respectively

specie and the distance between them, must coincide with the presented in Table 6.2.

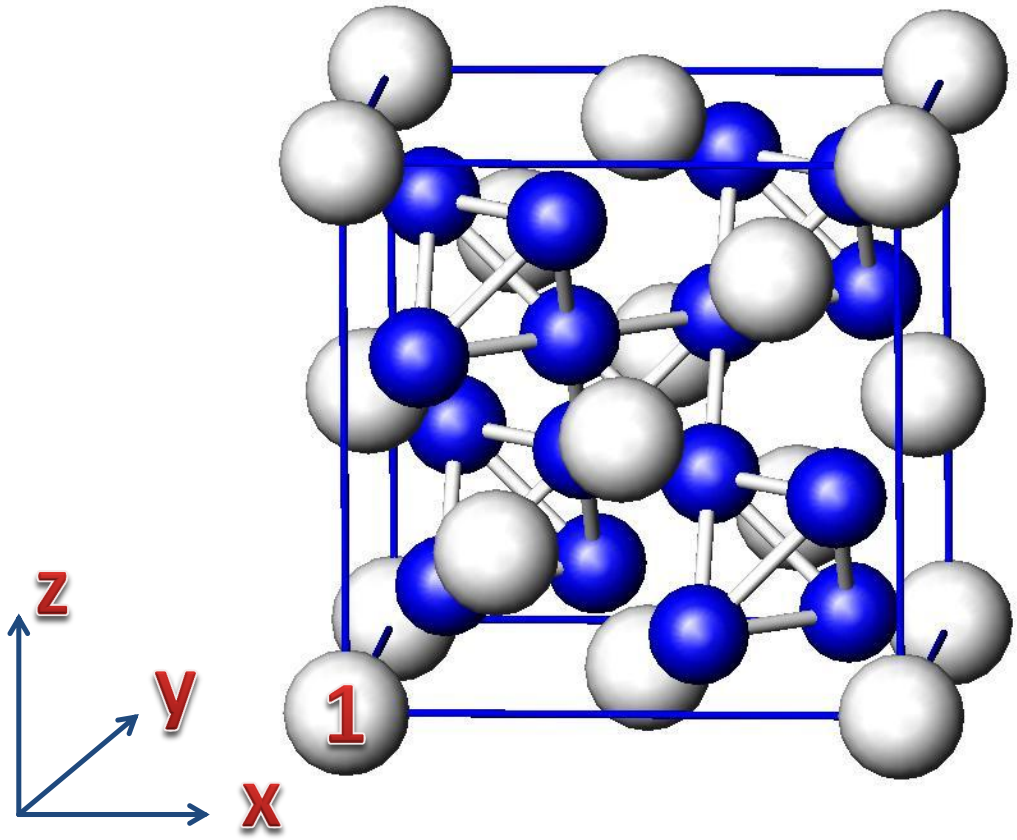

Figure 6.1: Schematic representation of a LAVES PHASE C15 unit cell. White and blue atoms represent A (Re) and B (Tm) atoms respectively. This image has been taken from [4].

We want to finish remarking that LAVES PHASE C15 atomic structure is not only important for ferrimagnets because there are several interesting materials that present this crystalline structure such as Mg_2Cu [4], $BaRh_2$ or $BaPd_2$ [168].

atom label	$r_{1j}(a)$			atom type	atom label	$r_{1j}(a)$			atom type
1	0	0	0	1	13	0.125	0.625	0.125	2
2	0.5	0.5	0	1	14	0.375	0.875	0.125	2
3	0.5	0	0.5	1	15	0.125	0.875	0.375	2
4	0	0.5	0.5	1	16	0.375	0.625	0.375	2
5	0.25	0.25	0.25	1	17	0.125	0.125	0.625	2
6	0.75	0.75	0.25	1	18	0.375	0.375	0.625	2
7	0.25	0.75	0.75	1	19	0.125	0.375	0.875	2
8	0.75	0.25	0.75	1	20	0.375	0.125	0.875	2
9	0.625	0.125	0.125	2	21	0.625	0.625	0.625	2
10	0.875	0.375	0.125	2	22	0.875	0.875	0.625	2
11	0.875	0.125	0.375	2	23	0.625	0.875	0.875	2
12	0.625	0.375	0.375	2	24	0.875	0.625	0.875	2

Table 6.1: Positions of the 24 atoms belonging to the LAVES PHASE C15 unit cell file in units of the lattice parameter a. Atom label is a number that identifies the 24 atoms inside the unit cell, $r_{1j}(a)$ is the position of the atom labeled as j respect to the atom labeled as 1 and atom type distinguishes the specie of the atom: 1 and 2 mean A (white) and B (blue) respectively.

Re		Tm		distance (a)
Number of interactions	atoms-type	Number of interactions	atoms-type	
		6	Tm-Tm	$\frac{\sqrt{2}}{4}$
12	Re-Tm	6	Tm-Re	$\frac{\sqrt{11}}{8}$
4	Re-Re			$\frac{\sqrt{3}}{4}$
		12	Tm-Tm	$\frac{\sqrt{6}}{4}$
16	Re-Tm	8	Tm-Re	$\frac{3\cdot\sqrt{3}}{8}$
12	Re-Re	12	Tm-Tm	$\frac{1}{\sqrt{2}}$

Table 6.2: Number of neighbors for both rare-earth (RE) and transition metal (TM) atoms for a bulk LAVES PHASE C15 atomic structure, with the corresponding distance between neighbors as a function of the lattice parameter a. Atom-type represents the species of the atoms at the corresponding distance.

6.3 Modeling $GdFe_2$ and $TbFe_2$ Laves phase compounds

6.3.1 The Spin Hamiltonian parameterisation from *ab-initio* methods

As it has been done in the previous chapters (4.3.1, 5.3.1), the starting point to investigate the magnetic properties of a material using atomistic spin dynamics simulations is to parametrize the Spin Hamiltonian described in eq. (2.1). In this chapter, the spin Hamiltonians we want to parametrize corresponds to ferrimagnetic compounds with a 33% composition of rare-earth and 66% of transition metal elements ($ReTm_2$), because ferrimagnetic materials with this composition crystallize in a Laves a phase C15 atomic structure if the transition metal is iron, nickel or cobalt [49].

The materials selected to be simulated are $GdFe_2$ and $TbFe_2$. The first one has been choosen because $GdFe_2$ has been shown to exhibit $TIMS$ on its disordered atomic structure for concentrations close to $x = 0.33$ [21], which is the Laves phase C15 concentration. On the other hand, Tb based ferrimagnetic materials have a stronger anisotropy than Gd based [10], which is a requirement for data storage devices.

The Heisenberg hamiltonian, presented in eq. (2.1), is parametrized both for $GdFe_2$ and $TbFe_2$, using the *ab-initio* long range exchange interactions that our co-worker S. Khmelevskyi has calculated using the previuosly method described in chapter 4.3.1. The *ab-initio* method used by S. Khmelevskyi has been described briefly in section 4.3.1 for the case of parameterizating Co HCP. For each material, the exchange parameters are calculated using two different methods: the ferrimagnetic ground state (FM)[73, 100] and the disordered local moment approach DLM [146]. Ferrimagnetic ground state takes into account the energy difference between a system with the spins alinged antiferromagnetically and a system in which two spins are rotated to calculate the exchange parameters. The disordered local moment considered that each magnetic spin could rotate independently to each other. We need to consult M. Carmen if this description is correct. The different exchange parameter sets are presented Table 6.3 up to the first 6 shells.

The exchange interactions are shown up to the first 6 shells only for the Fe interactions and for the RE material up to the first 5 shells. The atoms that interact with the RE elements on its 6th shell are Fe atoms, therefore if we consider this interaction, we need to take into account another interaction more in Fe. Thus, we decided to cut exchange interactions at this distance.

R_{ij}	N_s	J_{ij} label	$J_{0j}(meV)$			
			$GdFe_2$		$TbFe_2$	
			Fm	DLM	Fm	DLM
$(\frac{1}{8}\frac{1}{8}\frac{3}{8})$	12	$J_{Re-Tm,1}$	-20.10	-13.44	16.44	-9.49
$(\frac{1}{4}\frac{1}{4}\frac{1}{4})$	4	$J_{Re-Re,1}$	12.58	4.56	8.69	2.99
$(\frac{1}{8}\frac{5}{8}\frac{1}{8})$	12	$J_{Re-Tm,2}$	-1.05	-1.21	-1.58	-0.88
$(\frac{3}{8}\frac{3}{8}\frac{3}{8})$	4	$J_{Re-Tm,3}$	-2.54	-2.15	-3.28	-1.79
$(\frac{1}{2}\frac{1}{2}0)$	12	$J_{Re-Re,2}$	0.99	0.47	0.75	0.29
$(0\frac{1}{4}\frac{1}{4})$	6	$J_{Tm-Tm,1}$	42.06	44.48	31.43	40.82
$(\frac{1}{8}\frac{-3}{8}\frac{1}{8})$	6	$J_{Tm-Re,1}$	-20.10	-13.44	16.44	-9.49
$(\frac{1}{2}\frac{1}{4}\frac{1}{4})$	12	$J_{Tm-Tm,2}$	-2.88	-0.49	-1.08	-0.78
$(\frac{1}{8}\frac{1}{8}\frac{5}{8})$	6	$J_{Tm-Re,2}$	-1.05	-1.21	-1.58	-0.88
$(\frac{3}{8}\frac{3}{8}\frac{3}{8})$	2	$J_{Tm-Re,3}$	-2.54	-2.15	-3.28	-1.79
$(\frac{-1}{2}\frac{1}{2}0)$	12	$J_{Tm-Tm,3}$	3.17	3.77	5.88	6.46

Table 6.3: The values of the exchange parameters obtained from *ab-initio* calculations by S. Khmelevskiy for $TbFe_2$ and $GdFe_2$, in a LAVES PHASE C15 atomic structure. Two different *ab-initio* methods have been used: the ferrimagnetic (FM) ground state and the disordered local moment (DLM). Exchange parameters are shown up to the first 6 shells. R_{0j} is the shell position in units of lattice constant, N_s is the number of equivalent sites in the shell. $(a-b)$ label in J_{a-b} denotes the type of the interacting atoms with $a = Re, Tm$ and $b = Re, Tm$. $i = 1, 2, 3$ denotes the numbering for interactions.

Comparing Table 6.2 with Table 6.3, we realise the existence of an anisotropic exchange interactions between neighbors of the same distance as in Co HCP.

The values of magnetic moments obtained from the *ab-initio* calculation are presented in Table 6.4 together with the experimental values for bulk materials found in the literature. It is shown that the values of the magnetic moments for the LAVES PHASE C15 alloys do not differ too much from the experimental values for bulk materials. This makes sense with the results presented in [59], where it is explained that magnetic moments change in alloys with respect to pure elements. In any case, we do not expect that these slight differences between the magnetic moment values could change our results, therefore, in the absence of correct magnetic moments values for the alloys, using their values for pure materials is a good approximation as it has been done in chapter 5.

An extra set of exchange parameters was calculated by S. Khmelevskyi for $GdFe_2$ fixing the magnetic moments to the experimental values. However, this extra set of parameters is not presented in this chapter because the results it gives are similar to those shown in the following.

	Ab-initio				*Experimental*		
	$GdFe_2$		$TbFe_2$		Fe [165]	Gd [45]	Tb [61]
	Fm	DLM	Fm	DLM			
$\mu(Tm)$	2.32	2.15	2.10	1.84	2.21	7.12	9.34
$\mu(Re)$	7.91	7.27	9.78	9.21			

Table 6.4: *Ab-initio* mangetic moments, in Bohr's magneton units (μ_B), in ferrimagnetic $TbFe_2$ and $GdFe_2$, with a LAVES PHASE C15 atomic structure, calculated with the ferromagnetic state and with DLM method. Experimental values for pure Fe, Gd and Tb are also presented for comparison.

The gyromagnetic factor, the damping constant and the anisopropies values which we have used for Langevin dynamics simulations of $ReTm_2$ are presented in Table 6.5. The value of the damping constant was taken for simplicity the same for both materials and it has been extracted from [163]. The gyromagntic ratio is also the same for both materials. The magnetic anisotropy for all the LAVES PHASE C15 systems considered in this chapter is uniaxial, pointing parallel to the [001] direction (z-axis), see fig. 6.1. The atomistic anisotropy value shown in Table 6.5 corresponds to the macroscopic value for Co HCP ($K = 0.53 \times 10^6$ J/m^3 [70]), however, as we are not considering a HCP atomic structure but a LAVES PHASE C15, the corresponding macroscopic anisotropy is in this case $K = 3.6 \times 10^5$ J/m^3. See details in section 6.3.3.

It must be pointed out that experimentally $GdFe_2$ really shows an uniaxial anisotropy parallel to [001] direction [116], arising from the distorsion on its Laves phase C15 atomic structure. For $GdFe_2$, the cubic Laves phase C15 atomic structure transforms into tetragonal one, leading to the uniaxial anisotropy parallel to [001] direction commented before, by slightly reducing its lattice parameter on the [001] direction, due to magnetostrictions effects [116]. For the case of $TbFe_2$, it is also true that magnetic anisotropy is uniaxial, however, in this case, the magnetostrictions effects deforms the cubic Laves phase C15 atomic structure into a rhombohedral one, leading an uniaxial anisotropy parallel to [111] direction [116]. In any case, it is well-known that the magnetic anisotropy does not play a relevant role in the ocurrence of ultrafast magnetisation switching.

gyromagnetic factor ($\frac{rad}{T \cdot s}$)	γ	$1.76 \cdot 10^{11}$ [162]
Damping constant	λ_{Co}	0.02 [163]
	λ_{Tb}	0.02 [163]
Anisotrpy constant($J/atom$)	$k_{\mathrm{u}}(Co)$	$5.85 \cdot 10^{-24}$
	$k_{\mathrm{u}}(Tb)$	$5.85 \cdot 10^{-24}$

Table 6.5: Modeling parameters used in atomistic spin simulations for $ReTm$ Laves phase C15 systems. The parameters are the same for both $GdFe_2$ and $TbFe_2$ with their corresponding Fm and DLM approaches.

6.3.2 Temperature-dependent magnetisation

Using these parameters, Langevin dynamics simulations have been performed for each material obtaining the magnetisation versus temperature curves. In Fig 6.2, we present the temperature dependent of the total magnetisation together with the corresponding sublattice resolved magnetisation.

The results of Fig 6.2 show that for all the parameter sets, the Curie temperature (T_C) values are higher than $1000K$. The extracted values are presented in Table 6.6 together with the known experimental one. The obtained T_C values are higher than the experimental value in any case. The overestimation of the T_C could arise from the magnetostriction effects that occurs in Laves phase C15 atomic structures [116]. The magnetostriction effects are specially important at high temperatures, however, the exchange parameters calculated by S. Khmelevskyi are calculated without taking into account this effects, therefore, it is possible that the exchange parameters are not completely correct for high temperatures simulations. Additionally, our $M(T)$ curves do not have magnetisation

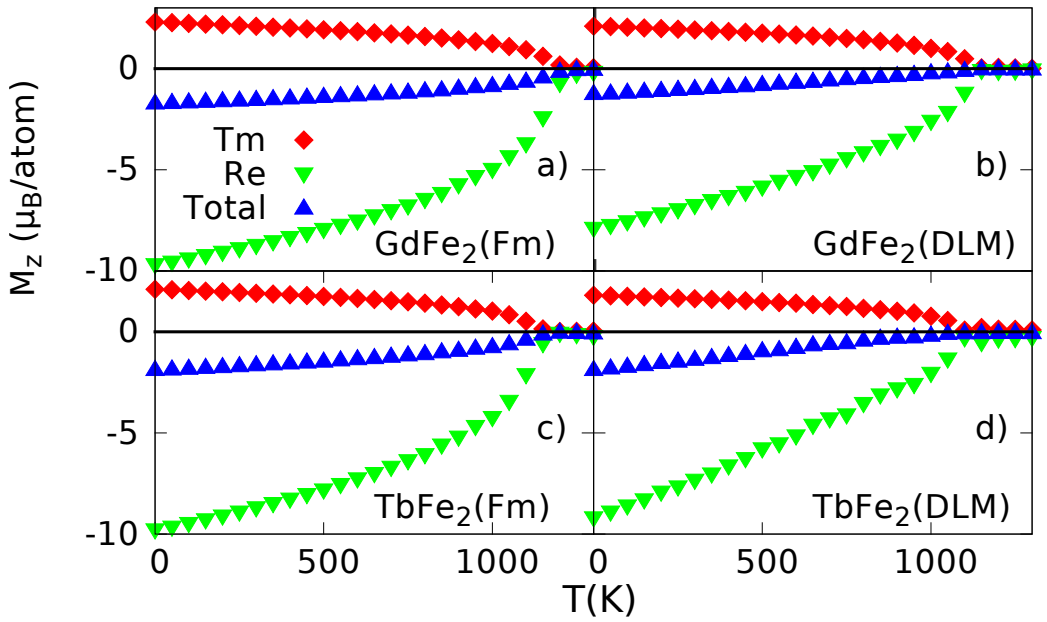

Figure 6.2: Calculated magnetisation versus temperature for all the *ab-initio* sets of parameters presented in Table 6.3. Red diamonds represents Fe, green triangules RE and blue triangules the total magnetisation.

compensation point, which is consistent with the experimental results we have found in literature dealing with $GdFe_2$ [104, 116] and $TbFe_2$ [95, 116].

$T_C(K)$					
Atomistic simulations				Experimental values	
$GdFe_2$		$TbFe_2$		$GdFe_2$	$TbFe_2$
FM	DLM	FM	DLM		
1200	1150	1150	1100	793 [104, 116]	653 [95, 116]

Table 6.6: Calculated Curie temperatures using Langevin dynamics simulations for $GdFe_2$ and $TbFe_2$. For each material, T_C has been calculated using the exchange parameters coming from two different *ab-initio* methods: ferromagnetic gound state and disordered local moment. Experimental values for T_C are also presented for comparison.

6.3.3 Evaluation of long-range exchange parameters

The exchange stiffness A for $GdFe_2$ and $TbFe_2$ can be calculated using eq. (4.9) for each set of exchange interactions presented in Table 6.3, as it was done in chapter 3 for Co HCP. However, obtaining the exchange stiffness for LAVES PHASE C15 atomic structures is more challenging than for the HCP case, because of the existence of two different types of atoms, the Re and the Tm. Thus, have calculated A, from eq. (4.9), for each atom of the 24 belonging to the unit cell, see subsection 6.2.1. All the Re atoms shows the same exchange stiffness value A_{Re} as well as all the Tm atoms shows the same A_{Tm}. In Table 6.7, A_{Re}, A_{Tm} as well as the average exchange stiffness $A = 0.33 \cdot A_{Re} + 0.66 \cdot A_{Tm}$ values are presented.

In this chapter we have considered the same atomistic magnetic anisotropy, $d = 5.85 \cdot 10^{-24} J/atom$, than for Co HCP, which corresponds to the macroscopic magnetic anisotropy $K = 0.53 \cdot 10^6 J/m^3$, as it has been shown in subsection 4.3.3. Nevertheless, as we are dealing with a LAVES PHASE C15 atomic structure instead of HCP, therefore, the atomic volumen is different and the macroscopic magnetic anisotropy is calculated as follows,

$$K = \frac{d}{V_{at}} = \frac{24 \cdot d}{V_{uc}} = \frac{24 \cdot d}{a^3}, \tag{6.1}$$

where V_{at} is the atomic volumen, defined as the volumen of the unit cell V_{uc} divided by the number of atoms inside it $n = 24$, see section 6.2.1. The volumen of the unit cell is defined as $V_{uc} = a^3$, with $a = 7.3\mathring{A}$ for both $GdFe_2$ and $TbFe_2$, being the lattice parameter for all the LAVES PHASE C15 materials considered

in this chapter [116]. Thus, the obtained macroscopic magnetic anisotropy is $K = 3.6 \cdot 10^5$.

Using the different values of the exchange stiffness shown in Table 6.7, the macroscopic anisotropy constant (K) and eq. (4.13) the domain wall width (δ_{DW}) is calculated for each set of exchange interactions. However, we have presented 3 different values of the exchange stiffness: A_{Re}, A_{Tm} and A. Thus, 3 different values of the domain wall width (δ_{Re}, δ_{Tm} and δ_{DW}) can be calculated for each set of exchange interactions. Nevertheless, as the antiferromagnetic exchange coupling between the Re and Tm sublattices is strongh for all the sets of parameters, it is expected that both domain walls, one for each sublattice, have a domain wall width similar to δ_{DW}, which is obtained from the average exchange stiffness A. The different values of δ_{DW} for each set of exchange interactions are presented in Table 6.7.

Atomistic spin dynamics simulations were performed with the aim of determining numerically the domain wall width for the ferrimagnets considered in this chapter. The length of the simulated system is 180 nm, which is long enough to fully contain a domain wall, and the cross section is 20 nm. The domain wall is constrained by applying anti-periodic boundary conditions. As a result, we have observed for all the cases that, both domain wall widths (δ_{sim}), for the Tm sublattice and for the Re one, are equal and corresponds to the domain wall width value (δ_{DW}) obtained using A in eq. 4.13. In Table 6.7, the simulated domain walls width δ_{sim} are presented. Fig. 6.3 shows the simulated domain wall profile for both sublattices of the $TbFe_2(DLM)$ set of exchange interactions, as well as its corresponding analitycal profile from eq. (4.12) using its δ_{DW} value.

	$GdFe_2$		$TbFe_2$	
	FM	DLM	FM	DLM
$A_{Re}(J/m \cdot 10^{-11})$	2.91	1.92	2.56	1.36
$A_{Tm}(J/m \cdot 10^{-11})$	2.77	3.18	3.40	3.48
$A(J/m \cdot 10^{-11})$	2.82	2.76	3.12	2.78
$\delta_{DW}(nm)$	27.8	27.5	29.2	27.6
$\delta_{sim}(nm)$	27.7	27.4	29.1	27.5

Table 6.7: Analitycal exchange stiffness for the different set of exchange parameters (DLM and FM) of $GdFe_2$ and $TbFe_2$ as well as the analitycal domain wall width and the simulated one.

It is shown in Table 6.7 that the simulated domain wall width values δ_{sim} matches with the analitycal value δ_{DW} obtained from the average exchange stiffness A. However, as it has been commented before, it happens because the anti-

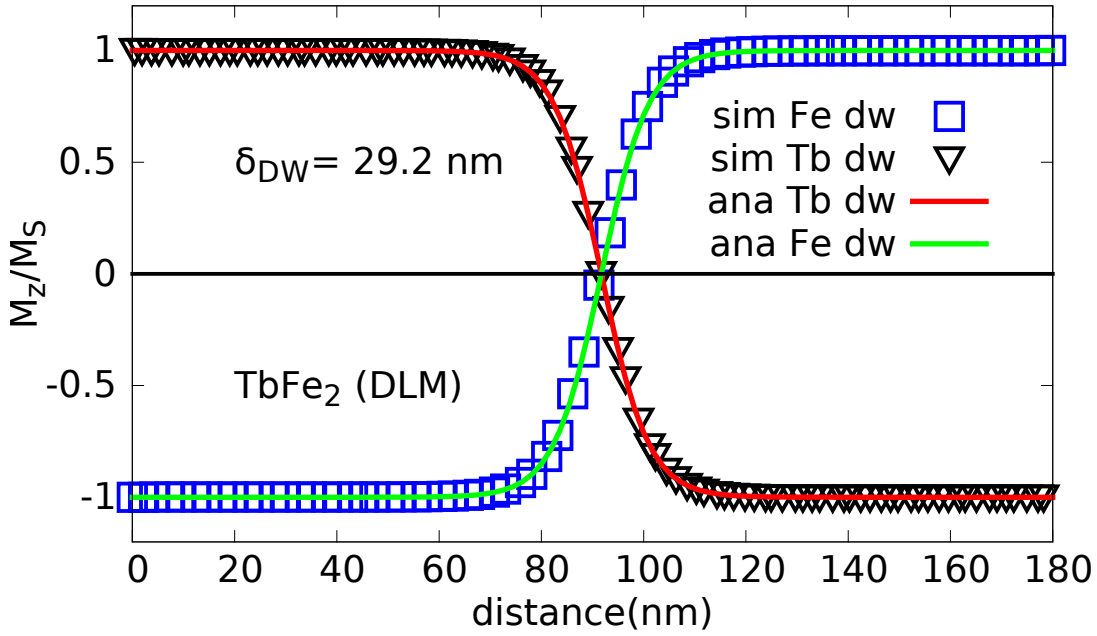

Figure 6.3: Sublattice resolved domain walls for the $TbFe_2(DLM)$ set of exchange interactions. M_z/Ms is the sublattice resolved z component of the magnetisation divided by its corresponding saturation magnetisation M_s. Blue squares and black triangles represent the simulated domain walls for Fe and Tb respectively. Green and red lines represent the analitycal domain wall profile from eq. 4.12 using the corresponding analitycal domain wall width from Table 6.7.

ferromagnetic exchange interaction is strongh, for lower values, it might happen that the domain walls have different domain wall widths as they have different exchange stiffness. In any case, is this small subchapter, we provide values of the exchange stiffness for $GdFe_2$ and $TbFe_2$ valid for micromagnetic simulations. Besides, for future work, the same systems can be simulated with temperature, which will allow to study the domain wall dynamics under ultrafast laser heating or temperature gradients.

6.3.4 Modeling of laser-induced magnetisation dynamics.

2TM parameters, used for simulations of the laser heat-assisted spin dynamics are presented in Table 6.8. For $GdFe_2$ we used the same set of parameters as for disordered $GdFeCo$ alloys in Ref. [21]. The parameters for $TbFe_2$ have been extracted from [60, 81] [1] also for $TbFe$ disordered alloys. Thus, we use these parameters sets with the idea that they could be a good approximation to the real parameters needed for $ReTm_2$ Laves phase C15 materials.

	$Cv_{ph}(J/Km^3)$	$\gamma_e(J/K^2m^3)$	$G_{el}(J/sKm^3)$
$GdFe_2$	$3 \cdot 10^6$	700	$1.7 \cdot 10^{18}$
$TbFe_2$	$2.3 \cdot 10^6$	220	$6.6 \cdot 10^{17}$

Table 6.8: Two temperature model parameters used in our simulations. Parameters for $GdFe_2$ and $TbFe_2$ has been taken from Refs. [21] and [60, 81] respectively. The same parameters are used for both FM and DLM parameter sets.

The response of the magnetisation to the laser heating excitation has been simulated using Langevin dynamics simulations for the four systems that have been considered in this chapter. The system created has 12^3 unit cells, which is equivalent to 41472 atoms. The lattice parameters for the ferrimagnetic Laves phase C15 materials are a = 7.341$\mathring{A}$ and a = 7.390 for $GdFe_2$ and $TbFe_2$ respectively [116], which leads to a system volume of $V \approx 6.7 \cdot 10^2 nm^3$. Firstly, the systems are thermalized at $300K$ until they reach equilibrium, after this, the laser pulse heats the systems. The laser pulse has a duration of $50fs$ and the simulated time after the thermalization is $10ps$.

We define the magnetisation quenching in the system after the action of the laser pulse as

$$Quenching\,[\%]_{Fe} = \frac{m_z^{Fe}(0ps) - m_z^{Fe}(10ps)}{m_z^{Fe}(0ps)} \cdot 100 \tag{6.2}$$

[1] To be noted that the TTM paramters presented in [60] have an mistake in $G_{el}(J/sKm^3)$ but they are extracted from [81] where the parameters are written correctly.

A queching value below 100% will characterize the final magnetisation for the system which did not switch. Values over 100% will mean that the final state has opposite direction than the initial one, thus, the system has swichted [1]. Note that values around 100% do not definitely define that the system magnetisation has reversed or not because in this case both situations with longer simulated time are possible. It must be pointed out that values around 100% may correspond to different possibilities: the first one is that the laser heating has demagnetized the system and it requires longer time to recover the magnetisation than 10 ps; the second one corresponds to the possibility that magnetisation has not vanished but it has rotated, pointing a different direction than z-axis at the end of the simulation. Both cases can be distinguished: if the quenching is around 100% for a large interval of fluencies, then, the system is demagnetized; if the quenching is around 100% at some fluencies only, then, the reversal is stochastic and the final Fe magnetisation may be pointing in xy plane. In any cases in both situations the switching is stochastic because we cannot predict in which direction the system is going to be recovered or if it will form domains during the recovery. However, domains nucleation in the simulations we are performing is not possible due to the small system size we are considering. The domain wall widths have been calculated in the previous section, giving for all the cases a domain wall width value around $28nm$, see Table 6.7 for exact values. Thus, as the sizes of system ($l \approx 9nm$) are smaller than δ_{DW} the domain wall cannot be nucleated.

The laser fluencies used for simulations range from values for which the systems cannot reverse magnetisation to those demagnetize the system. For all the systems studied in this chapter, we can distinguish three different types of magnetisation dynamics in terms of the laser fluence: (i) for low laser fluencies the decreases and recovers and does not reverse in any case (ii) for intermediated laser fluencies the magnetisation might reverse depending on the laser fluence; (iii) for higher fluencies the systems get demagnetized. We determine that for the intermediated fluencies, the magnetisation reversal is stochastic, because it swiches randomly in terms of fluences values. Some examples of the magnetisation dynamics for $TbFe_2(DLM)$ are shown in Fig. 6.4.

The values of *quenching* parameters obtained for several runs with different laser fluencies are presented in Fig. 6.5 for all the materials considered in this chapter.

The results presented in Fig. 6.5 show there is no laser fluence values for deterministic magnetisation swichting occurs. No deterministic magnetisation reveral has been found for these materials. However we were expecting to find

[1] To be noted that we are only considering z-axis component of the magnetisation for $Quenching\,[\%]_{Fe}$, thus in xy plane the magnesitation may be in any state.

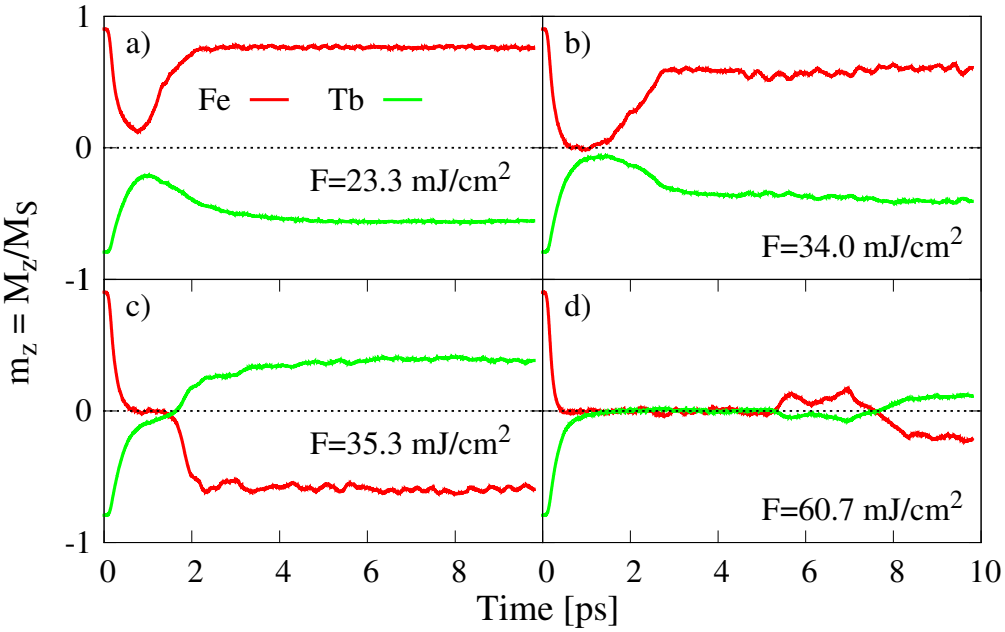

Figure 6.4: Example of the magnetisation dynamics of $TbFe_2(DLM)$ excited with different laser fluencies.

$TIMS$ at some fluence region for the following reasons: Firstly, we are dealing with ferrimagnetic materials with a Re material concentration of 33%. For the $TbCo$ case (see chapter 5) it has been shown that a laser pulse duration of $50fs$ is enough stimulus to reverse magnetisation. Of course, they are not the same systems but similars. The main differences between $ReTm$ LAVES PHASE C15 materials and the disordered $TbCo$ alloys presented in chapter 5, that might play an important a role in $TIMS$ in atomistic spin simulations are the following:

- The LAVES PHASE C15 atomic structure could play an important role because the atomic exchange field varies slightly from atom to atom because each atom of the same specie has the same neighbors of the same specie.

- Introducing exchange interactions up to the $6th$ shell might lead to a more chaotic behaviour in mangetisation dynamics (Stochastic region). Thus, it could be interesting to investigate only first neighbors interactions in order to compare with the many neighbors case.

- Finally, the exchange parameters values are probably the most important feature for the ocurrence of $TIMS$. For example, it is well known the necessity of an antiferromagnetic interaction between sublattices.

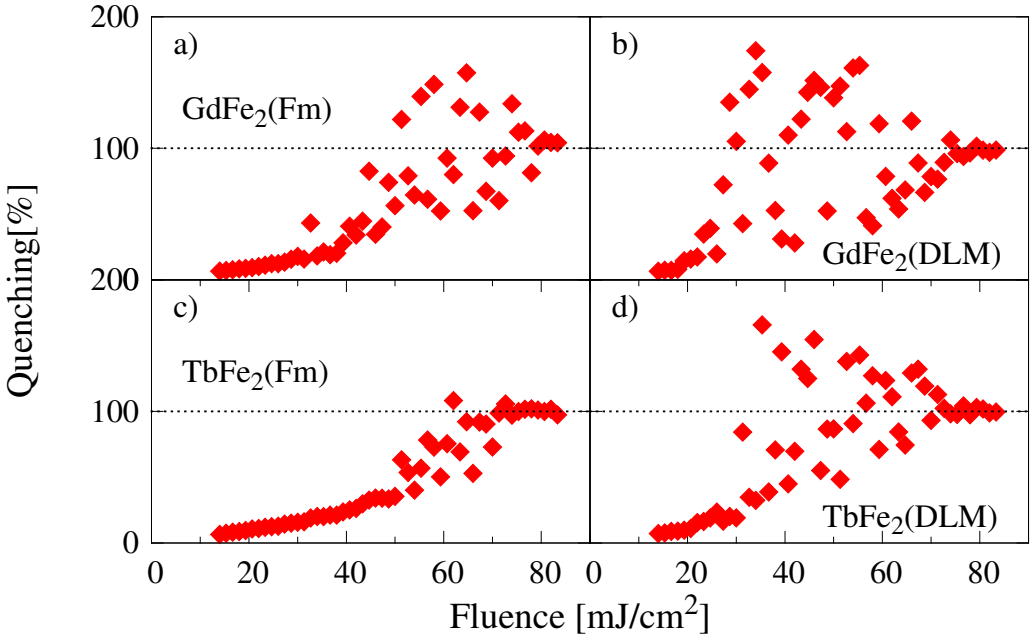

Figure 6.5: Calculated values for the quenching parameter for Fe m_z component in Laves phases as a function of the laser fluences and extracted from several runs. Figures a, b, c and d correspond to $GdFe_2(Fm)$, $GdFe_2(DLM)$, $TbFe_2(Fm)$ and $TbFe_2(DLM)$ respectively. In all simulated cases only stochastic AOS exists.

To clarify this situation, we first decided to investigate the relation of the long range exchange interaction and the stochastic reversal presented in Fig. 6.5. Thus, we restrict exchange interactions up to first neighbors. Nevertheless, we do not take only the first neighbor exchange values and disregard the others, the first neighbor exchange parameters which are taken into account are a renormalization of the long range exchange interaction in a mean-field sense,

$$
\begin{aligned}
\mathrm{J}_{Tm\text{–}Tm} &= \tfrac{1}{6}\left(6 \cdot J_{Tm\text{–}Tm,1} + 12 \cdot J_{Tm\text{–}Tm,2} + 12 \cdot J_{Tm\text{–}Tm,3}\right) \\
\mathrm{J}_{Re\text{–}Re} &= \tfrac{1}{4}\left(4 \cdot J_{Re\text{–}Re,1} + 12 \cdot J_{Re\text{–}Tm,2}\right) \\
\mathrm{J}_{Re\text{–}Tm} &= \tfrac{1}{6}\left(6 \cdot J_{Re\text{–}Tm,1} + 6 \cdot J_{Re\text{–}Tm,2} + 2 \cdot J_{Re\text{–}Tm,3}\right) \\
\mathrm{J}_{Tm\text{–}Re} &= \tfrac{1}{12}\left(12 \cdot J_{Tm\text{–}Re,1} + 12 \cdot J_{Tm\text{–}Re,2} + 4 \cdot J_{Tm\text{–}Re,3}\right)
\end{aligned}
\tag{6.3}
$$

in order keep as constant as possible materials features such as T_C of our old systems. Basically, we sum over all the interactions and divide by the number of first neighbors. The obtained exchange parameters are presented in Table 6.9.

With these new sets of exchange parameters, new atomistic spin simlations of laser heating have been performed. The rest of parameters used for each material are the same as for the longe range exchange case. The resulting quenching is shown in Fig. 6.6.

It is observed that the stochastic reversal region has vanished for Tb based materials, and reduced for Gd based. With these results it is possible to conclude that, the inclusion of long range exchange interactions might modify the range of fluencies in which stochastic reversal occurs, but it seems they are not responsible of the existence of deterministic swichting.

Therefore, it has been decided to stop calculating using *ab-initio* exchange parameters, treating them as variables, in order to investigate if the magnitude of the exchange interactions is the responsible of producing $TIMS$ or maybe is the fact that we are dealing with a LAVES PHASE C15 atomic structure instead of a disordered one.

R_{ij}	N_s	J_{ij} label	$J_{0j}(meV)$			
			$GdFe_2$		$TbFe_2$	
			Fm	DLM	Fm	DLM
$(\frac{1}{8}\frac{1}{8}\frac{3}{8})$	12	J_{Re-Tm}	-21.98	-15.37	-19.10	-10.94
$(\frac{1}{8}\frac{1}{8}\frac{1}{8})$	4	J_{Re-Re}	15.54	5.96	10.95	3.877
$(0\frac{1}{4}\frac{1}{4})$	6	J_{Tm-Tm}	42.61	51.00	41.00	52.19
$(\frac{1}{8}\frac{-3}{8}\frac{1}{8})$	6	J_{Tm-Re}	-21.98	-1.130	-19.10	-10.94

Table 6.9: Effective first neighbor exchange parameters for ferrimagnetic $TbFe_2$ and $GdFe_2$, from the *ab-initio* exchange parameters shown in Table 6.3 using eq. 6.3.4. R_{ij} is the shell position in units of lattice constant, N_s is the number of equivalent sites in the shell. J_{ij} label is the name we give to each interaction.

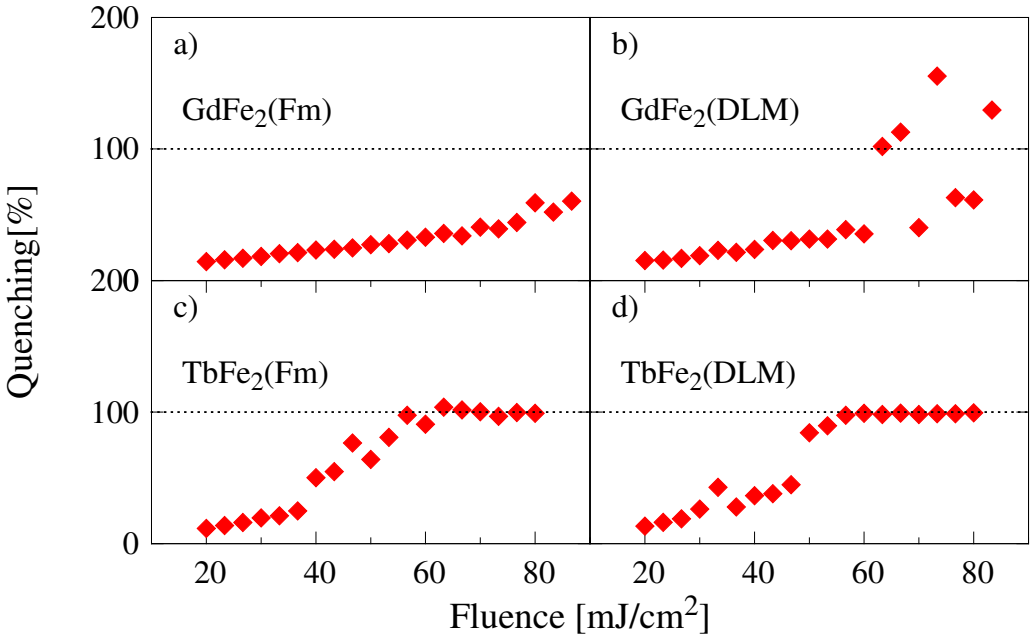

Figure 6.6: Calculated quenchin for Fe m_z component using the resulting first neighbour exchange interactions of renormalizing the complete set of exchange parameters. It is shown that as the number of neighbors taken into account reduces the stochastic region reduce too. Figures a, b, c and d correspond to $GdFe_2(Fm)$, $GdFe_2(DLM)$, $TbFe_2(Fm)$ and $TbFe_2(DLM)$ respectively.

6.4 $TbFe_2$ exchange parameters treated as variables.

Taking into account the materials presented in this chapter, $TbFe_2$ has been taken as a example, in order to investigate the effect of the exchange interactions magnitude in the ocurrence of ultrafast magnetisation reversal for a LAVES PHASE C15 ordered system. Therefore, to modelize $TbFe_2$ in atomistic spin simulations, all the parameters presented for $TbFe_2(DLM)$ in the present chapter have been used (see Table 6.5), except the exchange parameters, which are considered as free parameters. Note that the only difference between $TbFe_2(DLM)$ and $TbFe_2(Fm)$, without considering exchange parameters, is the value of the magnetic moments (see Table 6.4), but the they have similar values and do not play any relevant role in the ocurrence of AOS, so in the following we will refer our toy material $TbFe_2(DLM)$ as $TbFe_2$. The two temperature model parameters used in these simulations are the presented in Table 6.8 for the $TbFe_2$ case.

Considering just first neighbors exchange interactions to simplify the calculations, only three exchange parameters are needed for atomistic spin simulations: J_{Fe-Fe}, J_{Fe-Tb} and J_{Tb-Tb}. The last exchange interaction (J_{Tb-Tb}) is selected to have a fixed value (J_{Tb-Tb} = $8meV$) while the other two(J_{Fe-Fe} and J_{Fe-Tb}) are going to be varied in order to determine the role the exchange parameters play in the ocurrence of $TIMS$. J_{Tb-Tb} value has been selected for two main reasons: firstly it is a realistic first neighbor exchange interaction for bulk RE elements [163]; secondly this value is similar to the *ab-initio* value calculated by Serguej Khmelevskyi for $TbFe_2(DLM)$ presented in table 6.3. J_{Fe-Fe} is varied from $16meV$ to $50meV$ which ranges from a very small exchange interaction to a big value compared with the *ab-initio* first neighbor exchange obtained for bulk Fe BCC [126], or the first neighbor exchange fitted from the experimental T_C [46]. Finally, J_{Fe-Tb} ranges from $0meV$ to $14meV$ which means that we start with a system with two separate sublattices that converts progressively in a strongly coupled one. The $14meV$ top bound has been selected because this value has been considered for $GdCoFe$ in [21]. The exchange parameters are varied in steps of $1meV$. As a first step, the Curie temperature (T_C) and the compensation point (Tm) have been calculated for each case using Langevin dynamics. The obtained results are presented in Fig. 6.7.

In Fig. 6.7a it shown that the Curie temperature ranges from $T_C \approx 300K$ to $T_C \approx 1200K$. For each J_{Fe-Fe} value, the T_C value corresponding to the uncoupled sublattices case (J_{Fe-Tb} = 0), increases with J_{Fe-Tb} up to a T_C value for J_{Fe-Tb} = $14meV$ that almost doubles its initial value.

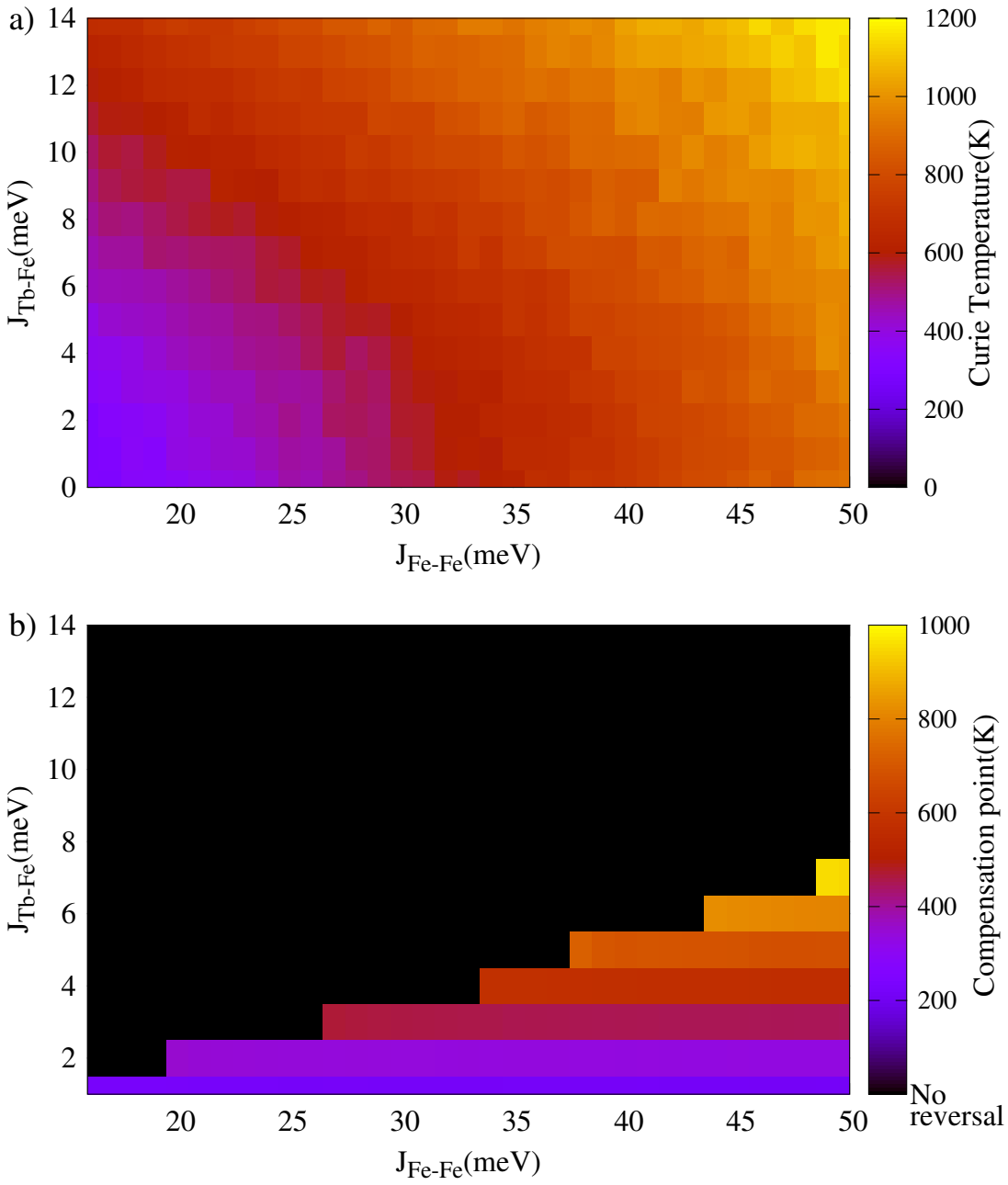

Figure 6.7: Calculated Curie temperature (figure a) and compensation point (figure b) in terms of the transition metal first neighbor interaction (J_{Fe-Fe}) and the antiferromagnetic interaction between sublattices (J_{Fe-Tb}). Black background in figure b means there is no compensation point (clabel indicate T=0K what is not correct).

From Fig. 6.7b we conclude that the compensation point only appears for low J_{Fe-Tb} values. However, as the J_{Fe-Fe} exchange increases, the J_{Fe-Tb} range for which exists a compensation point becomes wider. Compensation point ranges from T_M = 220K to T_M = 950K. The compensation point for a given J_{Fe-Tb} remains almost constant with changing the J_{Fe-Fe} exchange interaction. T_M value decreases very slow with increasing J_{Fe-Fe}. This feature observed numerically for this toy material, was used in the previous chapter (see section 5.3.1) to fit the exchange parameters of Tb_xCo_{1-x}. First, bulk exchange parameters were fitted to experimental T_C data, and after this, the antiferromagnetic exchange was used to fit experimental T_M data.

Before the laser heats the material, the system is thermalized at room temperature (T_{room} = 300K). Note that, at T_{room} there exists some exchange parameters cases for which magnetisation is vanished or it is so weak due to its corresponding T_C value is small (see Fig. 6.7). Consequently, we have skipped from laser simulations all the cases with $J_{Fe-Fe} < 25meV$.

To determine for which regions of exchange parameters the magnetisation reversal is deterministic, stochastic or does not exists, we also have varied the random number seed which creates thermal fluctuations in Langevin dynamics, with the aim of obtaining different magnetisation dynamics for each case. This number has been varied 15 times.

Fluence has been also varied from 10.66mJ/cm^2 to 16.66mJ/cm^2 in steps of 2mJ/cm^2. Again, as it was discussed in the previous chapter (see 5.3.2) the value of I_0 has been taken from literature for FePt (I_0 = $3 \cdot 10^{19} 1/m \cdot s$) [108]. Thus, the values of the fluence are not realistic but they can be reescaled to right one if the correct value of I_0 is determined. Only four cases of fluencies has been considered in order to save time in simulations, however each value is able to demagnetize a different region of exchange parameters. In fig. 6.8 it is represented the corresponding reversal probability for each set of exchange interactions to each fluence case.

From fig. 6.8 we can extract that $TIMS$ occurs in ferrimagnetic LAVES PHASE C15 materials. This feature means that, the variation of the atomic exchange field in disordered alloys from atom to atom due the different number of neighbors of the same specie (disordered alloys) does not have any influence the ocurrence of $TIMS$, because we have found this effect in the system we are studying, where the number of neighbors of the same specie does not change (ordered structure).

Therefore, we conclude that only relevant factor in the ocurrence of $TIMS$ is the exchange interaction. This was expected because as it was shown in the previous chapter, it is easier to find $TIMS$ if the laser pulse has a duration of fs, which is the time scale associated with exchange interactions, rather than ps,. In

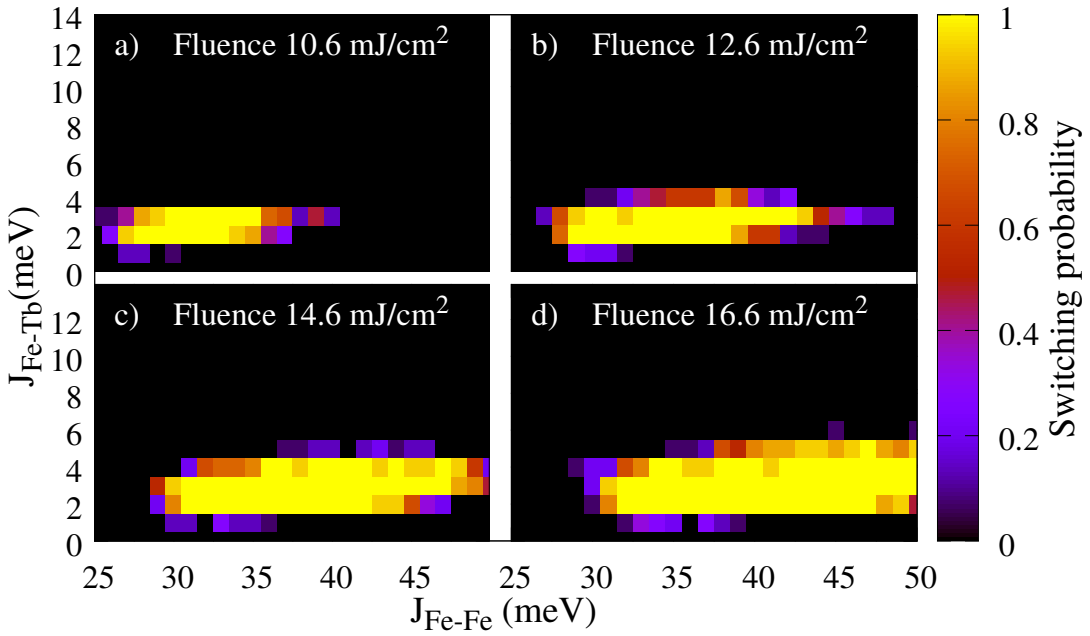

Figure 6.8: Magnetisation reversal probability of a LAVES PHASE C15 ferrimagnet as a function of the first neighbors exchange parameters J_{Fe-Fe} and J_{Fe-Tb}. Bulk exchange parameter of Tb is fixed ($J_{Tb-Tb\sim 8meV}$). Fluencies $10.66mJ/cm^2$, $12.66mJ/cm^2$, $14.66mJ/cm^2$, and $16.66mJ/cm^2$ are represented in Fig. a, b, c and d respectively.

addition, it is demostrated that for the case of non-coupled sublattices, thermally induced switching never occurs, confirming the necessity of an antiferromagnetic interaction between sublattices, which is one the requirements for AOS presented in [123, 135].

It is shown in fig. 6.8, that each laser fluence has associated a region of exchange parameters in which deterministic magnetisation reversal befalls. As fluence power increases, then size of the exchange region for which $TIMS$ happens increases too. In addition, as the fluence power increases switching occurs for stronger antiferromagnetic coupling and for stronger iron-iron ferromagnetic coupling.

It must be pointed out that we have decide to consider that, if the absolute value of the z-component of the magnetisation at the end of the simulation is less than a 10% of it initial value, then system does not reverse. To be specific we have consider that demagnetization, which provides stochastic reversal for longer simulation times, is not reversal. In terms of quenching it means that quenchings between 90% and 110% are defined as no reversal. Because of this, we see in case *d*) of fig. 6.8 that for low exchange parameters there is no switching, but it probably would be an stochastic one due to demagnetiation.

6.5 Conclusions

In conclusion, we have studied the effect of considering an ordered atomic structure, the effect of considering long range exchange interaction and the importance of the exchange parameter values, in the ocurrence of thermally driven swichting for ferrimangets. A Laves phase C15 atomic structure has been considered in our simulations in order to mimic a realistic crystalline ferrimagnet. Starting with a long range *ab-initio* exchange parameterization, we have also studied the effect of renormalizing long-range *ab-initio* exchange parameters to first neighbor exchange. Finally, we have considered the exchange parameters of the system variable in order to study their importance in $TIMS$ occurence.

To summarize the conclusions extracted from this chapter:

- A ferrimagnetic system with an ordered atomic structure might produce deterministic thermally induced magnetisation swichting as well as in disordered alloys. We have demostrated it for Laves phase C15 atomic structure. Thus, it means that the change of the atomic exchange field, from one atom to another, due to the different number of neighbors of the same specie sorrounding it, does not determine in the ocurrence of $TIMS$.

- Assuming long range exchange interaction or not in atomistic spin simulations, will not determine the ocurrence of deterministic magnetisation switching. Exchange interaction is known to be long range, therefore it seems to be clear that it must not influence the ocurrence of $TIMS$. However, the might play an important role in the case of stochastic reversal.

- The main parameters determining the ocurrence of $TIMS$ are the exchange parameters. It has been shown that for a given fluence value it exits a region of exchange parameters for which magnetisation switching is deterministic. Comparing results of the free exchange parameters study with the corresponding to *ab-initio* exchange calculation, we determine that the reason for not observing thermally induced switching in the *ab-initio* case is that the exchange parameters are far away from the region of exchange interactions for which a ferrimagnetic LAVES PHASE C15 material might reverse. To be specific, the antiferromagnetic *ab-initio* exchange interactions are much bigger than the needed to produce $TIMS$.

- On the other hand, it has been demonstrated the necessity of an antiferromagnetic interaction between sublattices, which has been proposed as a requirement to produce $TIMS$. Its value is lower limited by $J_{Fe-Tb} = 2meV$ for all the laser fluencies studied here. However it seems not to be upper limited because as the laser fluence increases, stronger values J_{Fe-Tb} produce deterministic switching.

- As the fluence increases, the region of exchange interaction cases that produce deterministic $TIMS$ increases too, both in J_{Fe-Tb} and J_{Fe-Fe} exchange interaction range. This region displace to higher values of iron bulk exchange (J_{Fe-Fe}) with increasing the laser fluence.

- The laser fluencies used for the free exchange parameters case are lower than the used for the *ab-initio* case because, although the ferromagnetic exchange parameters (J_{Fe-Fe} and J_{Tb-Tb}) have similar values, the *ab-initio* antiferromagnetic exchange was much bigger than the parameters used in the free exchange study.

- In contrast to what we observed in the previous chapter for $TbCo$ disordered alloys, all the exchange cases for which deterministic magnetisation magnetisation reversal happens, present a compensation point (T_M). In addition, no deterministic switching has occured if T_M is below than room temperature.

- It is not needed to considered a spin resolved Hamiltonian as it was done in [163] to obtain thermally induced magnetisation reversal in a LAVES PHASE C15 ferrimagnet. It is enough to consider suitable exchange parameters.

  Finally, we note that, although $TIMS$ might occur both for disordered alloys and ordered atomic structures, the requirements for $TIMS$ are dependent on the structure considered. The fact that we have not found any case in which $TIMS$ occurs without a T_M over the room temperature (T_{room}), seems to be the main difference between $TbCo$ disordered alloys and LAVES PHASE C15 ferrimagnets.

Agradecimientos

Me gustaría agredecer en primer lugar a Oksana, aparte de por todas las cosas que me ha enseñado, por haber confiado en mí sin conocerme de nada y haber defendido el contrato que el CSIC anuló antes de empezar la tesis, y además, después de conocerme, siguió confiando en mí. También me gustaría agradecer a María del Carmen Muñoz lo mismo que a Oksana y además la paciencia que ha tenido conmigo para enseãrme cosas útiles.

Como mi grupo era pequeño (Serantes y Pablo) y se marcharon pronto, fui acogido por la comunidad magnética de mi planta y por ello me gustaría agradecer al grupo de estudiantes dirigidos por Manuel Vázquez, Rafael Pérez y Agustina Asenjo su compañía y su ayuda en momentos duros. Gracias a las dos Esteres, Alejandro (y Lina), Eider, Cristina, Jesús, David (G), Juana, ... y a todos sus visitantes con los que lo he pasado genial. Por supuesto, gracias a Serantes y Pablo.

Además he tenido la suerte de coincidir en mi planta con una gran generación de químicos, como Javi, la persona que me convenció de que el sistema científico podía ser divertido y que ha dejado como legado a tres grandes estudiantes: Mar, Reus y por supuesto Ediana (madre mía).

Me gustaría también agradecer a Juanma haber mantenido nuestros clúster funcionando, parece mentira que en mi primer día de trabajo mi labor fue montar Ebro con él.

También me gustaría agradecer al grupo de teatro (Jorge, Nacho, Javi, Álvaro, Rafa, ...) todo lo que trabajan porque cada Navidad no nos vayamos de vacaciones sin unas sonrisas.

Mención aparte merece la comunidad chilena, encabezada por Dora Altbir y David Laroze, que me ofrecieron la oportunidad de continuar mi doctorado en Chile y hacer el gran viaje de mi vida, hasta el momento. Gracias a ellos y gracias a Álvaro, Nico, Roberto, y a todos los chicos de la USACH y del CEDENNA. Por supuesto, gracias a Henrikh Baghramyan, el armenio más importante de Arica.

A mi Familia, padres, hermanos, Pedro y Luci, Pablito y el monstruito que está por venir, qué les voy a decir que no sepan.

AGRADECIMIENTOS

A toda la gente que no ha entrado en estos agradecimientos, no es porque no lo merezcan es que son muchos y en algún momento tengo que parar. Espero que nadie se sienta ofendido.

Por último, me gustaría nombrar a Ana, ella me encontró la oferta de trabajo de Oksana y gracias a ella estoy aquí.

Vale.

AGRADECIMIENTOS

References

[1] **http://math.nist.gov/oommf/. 68**

[2] **https://mogadalai.wordpress.com/2007/10/11/the-case-of-the-curious-reference/. 25**

[3] **https://sites.google.com/site/ed350201003/Task. 37**

[4] **http://www.geocities.jp/ohba**$_l ab_o b_p age/structure5.html.$ 100

[5] **VAMPIRE software package v.4 http://vampire.york.ac.uk (2015). 65, 66, 69**

[6] I. A. Abrikosov and H. L. Skriver. **Self-consistent linear-muffin-tin-orbitals coherent-potential technique for bulk and surface calculations: Cu-Ni, Ag-Pd, and Au-Pt random alloys.** ***Phys. Rev. B*****, 47:16532–16541, Jun 1993. 60**

[7] M. Aeschlimann, M. Bauer, S. Pawlik, W. Weber, R. Burgermeister, D. Oberli, and H. C. Siegmann. **Ultrafast Spin-Dependent Electron Dynamics in fcc Co.** ***Phys. Rev. Lett.*****, 79:5158–5161, Dec 1997. 6**

[8] A. Aharoni. ***Introduction to the Theory of Ferromagnetism.*** **Oxford University Press, Oxford, 1996. 56, 57, 66, 68**

[9] Sabine Alebrand, Ute Bierbrauer, Michel Hehn, Matthias Gottwald, Oliver Schmitt, Daniel Steil, Eric E. Fullerton, Stéphane Mangin, Mirko Cinchetti, and Martin Aeschlimann. **Sub-picosecond magnetization dynamics in TbCo alloys.** ***Phys. Rev. B*****, 89:144404, Apr 2014. 6, 81, 85, 89, 94, 97**

[10] Sabine Alebrand, Matthias Gottwald, Michel Hehn, Daniel Steil, Mirko Cinchetti, Daniel Lacour, Eric E. Fullerton, Martin Aeschlimann, and Stphane Mangin. **Light-induced magnetization reversal of high-anisotropy TbCo alloy films.** ***Applied Physics Letters*****, 101(16):162408, 2012. ii, 6, 7, 14, 15, 17, 24, 80, 81, 82, 85, 86, 97, 102**

[11] Sabine Alebrand, Alexander Hassdenteufel, Daniel Steil, Mirko Cinchetti, and Martin Aeschlimann. **Interplay of heating and helicity in all-optical magnetization switching.** ***Phys. Rev. B*****, 85:092401, Mar 2012. 80**

[12] V.P. Antropov, M.I. Katsnelson, and A.I. Liechtenstein. **Exchange interactions in magnets.** ***Physica B: Condensed Matter*****, 237:336 – 340, 1997. 34**

[13] N. W. Ashcroft and N. D. Mermin. ***Solid State Physics*****. Brooks Cole;, 1976. 41, 48**

[14] P. Asselin, R. F. L. Evans, J. Barker, R. W. Chantrell, R. Yanes, O. Chubykalo-Fesenko, D. Hinzke, and U. Nowak. **Constrained Monte Carlo method and calculation of the temperature dependence of magnetic anisotropy.** ***Phys. Rev. B*****, 82:054415, Aug 2010. 23, 27, 66**

[15] U. Atxitia. ***Modeling of ultrafast laser-induced magnetization dynamics within the Landay-Lifshitz-Bloch equations.*** **PhD thesis, Department Condensed Matter, Universidad Autonoma de Madrid, June 2012. 21, 83**

[16] U. Atxitia, O. Chubykalo-Fesenko, N. Kazantseva, D. Hinzke, U. Nowak, and R. W. Chantrell. **LLB-Micromagnetic modelling of laser-induced magnetisation dynamics.** ***Appl. Phys. Lett.*** **, 91:232507, 2007. 8**

[17] U. Atxitia, D. Hinzke, O. Chubykalo-Fesenko, U. Nowak, H. Kachkachi, O. N. Mryasov, R. F. Evans, and R. W. Chantrell. **Multiscale modeling of magnetic materials: Temperature dependence of the exchange stiffness.** ***Phys. Rev. B*****, 82:134440, Oct 2010. 59, 70, 71**

[18] C. H. Back, R. Allenspach, W. Weber, S. S. P. Parkin, D. Weller, E. L. Garwin, and H. C. Siegmann. **Minimum Field Strength in Precessional Magnetization Reversal.** ***Science*****, 285:864, 1999. 3**

[19] C. H. Back, D. Weller, J. Heidmann, D. Mauri, D. Guarisco, E. L. Garwin, and H. C. Siegmann. **Magnetization Reversal in Ultrashort Magnetic Field Pulses.** ***Phys. Rev. Lett.*****, 81:3251–3254, Oct 1998. 3**

[20] Alexander Baral and Hans Christian Schneider. **Magnetic switching dynamics due to ultrafast exchange scattering: A model study.** ***Phys. Rev. B*****, 91:100402, Mar 2015. 8**

[21] J. Barker, U. Atxitia, T. A. Ostler, O Hovorka, O. Chubykalo-Fesenko, and R. W. Chantrell. **Two-magnon bound state causes ultrafast thermally induced magnetisation switching.** ***Scientific Reports*****, 3(3262):3262. 14, 15, 32, 81, 97, 102, 110, 116**

[22] R. Bastardis, U. Atxitia, O. Chubykalo-Fesenko, and H. Kachkachi. **Unified decoupling scheme for exchange and anisotropy contributions and temperature-dependent spectral properties of anisotropic spin systems.** ***Phys. Rev. B*****, 86:094415, Sep 2012. 70, 74**

[23] Gerrit E. W. Bauer, Eiji Saitoh, and Bart J. van Wees. **Spin caloritronics.** ***Nat Mater*****, 11(5):391–399, May 2012. 4**

[24] E. Beaurepaire, J.-C. Merle, A. Daunois, and J. Y. Bigot. **Ultrafast spins dynamics in ferromagnetic nickel.** ***Phys. Rev. Lett.*****, 76:4250, 1996. 5, 6, 7**

[25] J.-Y. Bigot, V. Mircea, and E. Beaurepaire. **Coherent ultrafast magnetism induced by femtosecond laser pulses.** ***Nat. Phys.*****, 5:515–520, 2009. 6**

[26] Felix Bloch. **Über die Quantenmechanik der Elektronen in Kristallgittern.** ***Zeitschrift für Physik*****, 52(7):555–600, 1929. 21, 34**

[27] W. Brown. **Thermal fluctuation of fine ferromagnetic particles.** ***IEEE Transactions on Magnetics*****, 15(5):1196–1208, Sep 1979. 25**

[28] D. Bttcher, A. Ernst, and J. Henk. **Temperature-dependent Heisenberg exchange coupling constants from linking electronic-structure calculations and Monte Carlo simulations.** ***Journal of Magnetism and Magnetic Materials*****, 324(4):610 – 615, 2012. 62, 65**

[29] H.B. Callen and E. Callen. **The present status of the temperature dependence of magnetocrystalline anisotropy, and the l(l+1)2 power law.** ***Journal of Physics and Chemistry of Solids*****, 27(8):1271 – 1285, 1966. 27, 65, 66**

[30] L. S. Campana, A. Caramico D'Auria, M. D'Ambrosio, U. Esposito, L. De Cesare, and G. Kamieniarz. **Spectral-density method for classical systems: Heisenberg ferromagnet.** ***Phys. Rev. B*****, 30:2769–2775, Sep 1984. 59, 70**

[31] E. Carpene. **Ultrafast laser irradiation of metals: Beyond the two-temperature model.** ***Phys. Rev. B*****, 74:024301, Jul 2006. 31**

[32] E. Carpene, E. Mancini, C. Dallera, M. Brenna, E. Puppin, and S. De Silvestri. **Dynamics of electron-magnon interaction and ultrafast demagnetization in thin iron films.** ***Phys. Rev. B*****, 78:174422, Nov 2008. 6**

[33] K. Carva, M. Battiato, and P. M. Oppeneer. **Ab Initio.** ***Phys. Rev. Lett.*****, 107:207201, Nov 2011. 8, 25**

[34] J.K. Chen, D.Y. Tzou, and J.E. Beraun. **A semiclassical two-temperature model for ultrafast laser heating.** ***International Journal of Heat and Mass Transfer*****, 49(12):307 – 316, 2006. 31**

[35] Jonathan Chico, Corina Etz, Lars Bergqvist, Olle Eriksson, Jonas Fransson, Anna Delin, and Anders Bergman. **Thermally driven domain-wall motion in Fe on W(110).** ***Phys. Rev. B*****, 90:014434, Jul 2014. 56**

[36] O. Chubykalo-Fesenko, U. Nowak, R. W. Chantrell, and D. Garanin. **Dynamic approach for micromagnetics close to the Curie temperature.** ***Phys. Rev. B*****, 74:094436, 2006. 29**

[37] Ronald E. Cohen, L. Stixrude, and Evgeny Wasserman. **Tight-binding computations of elastic anisotropy of Fe, Xe, and Si under compression.** ***Phys. Rev. B*****, 56:8575–8589, Oct 1997. 36**

[38] J. Crangle. **LIX. The magnetic moments of cobalt-copper alloys.** ***The London, Edinburgh, and Dublin Philosophical Magazine and Journal of Science*****, 46(376):499–513, 1955. 63**

[39] B. D. Cullity. **Introduction to magnetic materials, 1972. 53, 63, 74**

[40] Vctor Antonio de la Pea OShea, Iberio de P. R. Moreira, Alberto Roldn, and Francesc Illas. **Electronic and magnetic structure of bulk cobalt: The , , and -phases from density functional theory calculations.** ***The Journal of Chemical Physics*****, 133(2):024701, 2010. 48**

[41] H. F. Ding, A. K. Schmid, Dongqi Li, K. Yu. Guslienko, and S. D. Bader. **Magnetic Bistability of Co Nanodots.** ***Phys. Rev. Lett.*****, 94:157202, Apr 2005. 55**

[42] H. F. Ding, W. Wulfhekel, and J. Kirschner. **Ultra sharp domain walls in the closure domain pattern of Co(0001).** ***EPL (Europhysics Letters)*****, 57(1):100, 2002. 55**

[43] K. M. Döbrich, G. Bihlmayer, K. Starke, J. E. Prieto, K. Rossnagel, H. Koh, E. Rotenberg, S. Blügel, and G. Kaindl. **Electronic band**

structure and Fermi surface of ferromagnetic Tb: Experiment and theory. *Phys. Rev. B*, 76:035123, Jul 2007. 24, 85

[44] M. S. El Hadri, P. Pirro, C.-H. Lambert, S. Petit-Watelot, Y. Quessab, M. Hehn, F. Montaigne, G. Malinowski, and S. Mangin. **Two types of all-optical magnetization switching mechanisms using femtosecond laser pulses. *Phys. Rev. B*, 94:064412, Aug 2016. 7, 10, 80, 81, 82, 91, 94**

[45] J. F. Elliott, S. Legvold, and F. H. Spedding. **Some Magnetic Properties of Gadolinium Metal. *Phys. Rev.*, 91:28–30, Jul 1953. 104**

[46] R F L Evans, W J Fan, P Chureemart, T A Ostler, M O A Ellis, and R W Chantrell. **Atomistic spin model simulations of magnetic nanomaterials. *Journal of Physics: Condensed Matter*, 26(10):103202, 2014. 8, 26, 33, 39, 52, 63, 65, 66, 69, 75, 82, 116**

[47] R. F. L. Evans, D. Hinzke, U. Atxitia, U. Nowak, R. W. Chantrell, and O. Chubykalo-Fesenko. **Stochastic form of the Landau-Lifshitz-Bloch equation. *Phys. Rev. B*, 85:014433, Jan 2012. 8**

[48] Richard F. L. Evans, Thomas A. Ostler, Roy W. Chantrell, Ilie Radu, and Theo Rasing. **Ultrafast thermally induced magnetic switching in synthetic ferrimagnets. *Applied Physics Letters*, 104(8):082410, 2014. 6, 80**

[49] J.J.M. Franse and R.J. Radwaski. **Chapter 5 Magnetic properties of binary rare-earth 3d-transition-metal intermetallic compounds. 7 of *Handbook of Magnetic Materials*, pages 307 – 501. Elsevier, 1993. 98, 102**

[50] D. A. Garanin. **Self-consistent Gaussian approximation for classical spin systems: Thermodynamics. *Phys. Rev. B*, 53:11593–11605, May 1996. 15, 33, 82**

[51] D. A. Garanin. **Fokker-Planck and Landau-Lifshitz-Bloch equations for classical ferromagnets. *Phys. Rev. B*, 55:3050–3057, Feb 1997. 8, 29**

[52] Jess Garduo-Meja, Michael P. Higlett, and Stephen R. Meech. **Modelling the influence of nonthermal electron dynamics in thin and ultrathin gold films. *Chemical Physics*, 341(13):276 – 284, 2007. Ultrafast Dynamics of Molecules in the Condensed Phase: Photon Echoes and Coupled ExcitationsA Tribute to Douwe A. Wiersma. 31**

[53] Th. Gerrits, H. A. M. van den Berg, J. Hohlfeld, L. Bar, and Th. Rasing. **Ultrafast precessional magnetization reversal by picosecond magnetic field pulse shaping.** ***Nature*****, 418:509–512, Aug 2002. 3, 5**

[54] T.L. Gilbert. **A Lagrangian formulation of the gyromagnetic equation of the magnetic field.** ***Phys. Rev.*****, 100(5):1243, 1995. 25**

[55] J. Gorchon, R. B. Wilson, Y. Yang, A. Pattabi, J. Y. Chen, L. He, J. P. Wang, M. Li, and J. Bokor. **Role of electron and phonon temperatures in the helicity-independent all-optical switching of GdFeCo.** ***Phys. Rev. B*****, 94:184406, Nov 2016. 12, 17, 81, 91, 97**

[56] M. Grimsditch, Eric E. Fullerton, and R. L. Stamps. **Exchange and anisotropy effects on spin waves in epitaxial Co films.** ***Phys. Rev. B*****, 56:2617–2622, Aug 1997. 55, 75**

[57] Darko Grujicic and Batric Pesic. **Micromagnetic studies of cobalt microbars fabricated by nanoimprint lithography and electrodeposition.** ***Journal of Magnetism and Magnetic Materials*****, 285(3):303 – 313, 2005. 55**

[58] J. Güdde, U. Conrad, V. Jähnke, J. Hohlfeld, and E. Matthias. **Magnetization dynamics of Ni and Co films on Cu(001) and of bulk nickel surfaces.** ***Phys. Rev. B*****, 59:R6608–R6611, Mar 1999. 6**

[59] P. Hansen, C. Clausen, G. Much, M. Rosenkranz, and K. Witter. **Magnetic and magnetooptical properties of rareearth transitionmetal alloys containing Gd, Tb, Fe, Co.** ***Journal of Applied Physics*****, 66(2):756–767, 1989. 13, 85, 94, 104**

[60] A. Hassdenteufel, B. Hebler, C. Schubert, A. Liebig, M. Teich, M. Helm, M. Aeschlimann, M. Albrecht, and R. Bratschitsch. **Thermally Assisted All-Optical Helicity Dependent Magnetic Switching in Amorphous Fe100xTbx Alloy Films.** ***Advanced Materials*****, 25(22):3122–3128, 2013. 6, 110**

[61] D. E. Hegland, S. Legvold, and F. H. Spedding. **Magnetization and Electrical Resistivity of Terbium Single Crystals.** ***Phys. Rev.*****, 131:158–162, Jul 1963. 104**

[62] Volker Heine. **Electronic Structure from the Point of View of the Local Atomic Environment. 35 of *Solid State Physics*, pages 1 – 127. Academic Press, 1980. 40**

[63] D. Hinzke, U. Nowak, R. W. Chantrell, and O. N. Mryasov. **Orientation and temperature dependence of domain wall properties in FePt.** ***Applied Physics Letters*****, 90(8):082507, 2007. 23**

[64] J. Hohlfeld, Th. Gerrits, M. Bilderbeek, Th. Rasing, H. Awano, and T. Ohta. **Fast magnetization reversal of GdFeCo induced by femtosecond laser pulses.** ***Phys. Rev. Lett.*****, 65:012413, 2001. 8**

[65] J. Hohlfeld, E. Matthias, R. Knorren, and K. H. Bennemann. **Nonequilibrium Magnetization Dynamics of Nickel.** ***Phys. Rev. Lett.*****, 78:4861–4864, Jun 1997. 6**

[66] A. B. Kashuba F. King H. C. Siegmann J. Stohr G. Ju B. Lu I. Tudosa, C. Stamm and D. Weller. **The ultimate speed of magnetic switching in granular recording media.** ***Nature*****, 428:831–833, April 2004. 4, 5**

[67] Yu P Ivanov, M Vzquez, and O Chubykalo-Fesenko. **Magnetic reversal modes in cylindrical nanowires.** ***Journal of Physics D: Applied Physics*****, 46(48):485001, 2013. 56**

[68] J. E. Beraun J. K. Chen. **NUMERICAL STUDY OF ULTRASHORT LASER PULSE INTERACTIONS WITH METAL FILMS.** ***Numerical Heat Transfer, Part A: Applications*****, 40(1):1–20, 2001. 31**

[69] Xiankai Jiao, Zongzhi Zhang, and Yaowen Liu. **Modeling of Temperature Dependence of Magnetization in TbFe Films An Atomistic Spin Simulation Study.** ***SPIN*****, 06(01):1650003, 2016. 81**

[70] D. Jiles. **In *Introduction to magnetism and magnetic materials*. Chapman and Hall, London, 1995. 65, 104**

[71] R. John, M. Berritta, D. Hinzke, C. Mller, T. Santos, H. Ulrichs, P. Nieves, J. Walowski, R. Mondal, O. Chubykalo-Fesenko, J. McCord, P. M. Oppeneer, U. Nowak, and M. Mnzenberg. **Magnetization switching of FePt nanoparticle recording medium by femtosecond laser pulses.** ***arXiv:1606.08723 [cond-mat.mes-hall]*****. 6, 8, 10**

[72] T. Kampfrath, A. Sell, G. Klatt, A. Pashkin, S. Mahrlein, T. Dekorsy, M. Wolf, M. Fiebig, A. Leitenstorfer, and R. Huber. **Coherent terahertz control of antiferromagnetic spin waves.** ***Nat Photon*****, 5(1):31–34, Jan 2011. 6**

[73] M. I. Katsnelson and A. I. Lichtenstein. **First-principles calculations of magnetic interactions in correlated systems.** ***Phys. Rev. B*****, 61:8906–8912, Apr 2000. 34, 102**

[74] N. Kazantseva, D. Hinzke, U. Nowak, R. W. Chantrell, U. Atxitia, and O. Chubykalo-Fesenko. **Towards multiscale modeling of magnetic materials: Simulations of FePt.** ***Phys. Rev. B*****, 77:184428, May 2008. 23, 24, 28**

[75] N. Kazantseva, R. Wieser, and U. Nowak. **Transition to Linear Domain Walls in Nanoconstrictions.** ***Phys. Rev. Lett.*****, 94:037206, Jan 2005. 29**

[76] N. Kazantseva, R. Wieser, and U. Nowak. **Transition to Linear Domain Walls in Nanoconstrictions.** ***Phys. Rev. Lett.*****, 94:37206, 2005. 59**

[77] Sergii Khmelevskyi and Peter Mohn. **Layered antiferromagnetism with high Neel temperature in the intermetallic compound Mn2Au.** ***Applied Physics Letters*****, 93(16):162503, 2008. 61**

[78] Sergii Khmelevskyi, Eszter Simon, and László Szunyogh. **Antiferromagnetism in** Ru_2MnZ (Z = Sn, Sb, Ge, Si) **full Heusler alloys: Effects of magnetic frustration and chemical disorder.** ***Phys. Rev. B*****, 91:094432, Mar 2015. 61**

[79] A. R. Khorsand, M. Savoini, A. Kirilyuk, A. V. Kimel, A. Tsukamoto, A. Itoh, and Th. Rasing. **Role of Magnetic Circular Dichroism in All-Optical Magnetic Recording.** ***Phys. Rev. Lett.*****, 108:127205, Mar 2012. 10, 80, 81**

[80] A. R. Khorsand, M. Savoini, A. Kirilyuk, A. V. Kimel, A. Tsukamoto, A. Itoh, and Th. Rasing. **Element-Specific Probing of Ultrafast Spin Dynamics in Multisublattice Magnets with Visible Light.** ***Phys. Rev. Lett.*****, 110:107205, Mar 2013. 89, 94, 97**

[81] J. W. Kim, K. D. Lee, J. W. Jeong, and . S. C. Shin. **Ultrafast spin demagnetization by nonthermal electrons of TbFe alloy film.** ***Appl. Phys. Lett*****, 94:192506, 2009. 110**

[82] A. V. Kimel, A. Kirilyuk, P. A. Usachev, R. V. Pisarev, A. M. Balbashov, and Th. Rasing. **Ultrafast non-thermal control of magnetization by instantaneous photomagnetic pulses.** ***Nature*****, 435:655–657, Jun 2005. 9, 80**

[83] A. V. Kimel, R. V. Pisarev, J. Hohlfeld, and Th. Rasing. **Ultrafast Quenching of the Antiferromagnetic Order in** $FeBO_3$**: Direct Optical Probing of the Phonon-Magnon Coupling.** ***Phys. Rev. Lett.*****, 89:287401, Dec 2002. 6**

[84] Alexey V. Kimel. **All-optical switching: Three rules of design.** ***Nat Mater*****, 13(3):225–226, Mar 2014. News and Views. 12**

[85] Andrei Kirilyuk, Alexey V. Kimel, and Theo Rasing. **Ultrafast optical manipulation of magnetic order.** ***Rev. Mod. Phys.*****, 82:2731–2784, Sep 2010. 16**

[86] E. Kneller. ***Ferromagnetism.*** **Springer Science, 1962. 56**

[87] B. Koopmans, G. Malinowski, F. Dalla Longa, D. Steiauf, M. Fahnle, T. Roth, M. Cinchetti, and M. Aeschlimann. **Explaining the paradoxical diversity of ultrafast laser-induced demagnetization.** ***Nat Mater*****, 9(3):259–265, Mar 2010. 8**

[88] B. Koopmans, M. van Kampen, J. T. Kohlhepp, and W. J. M. de Jonge. **Ultrafast Magneto-Optics in Nickel: Magnetism or Optics?** ***Phys. Rev. Lett.*****, 85:844, 2000. 8**

[89] J. Kötzler, D. A. Garanin, M. Hartl, and L. Jahn. **Evidence for critical fluctuations in Bloch walls near their disordering temperature.** ***Phys. Rev. Lett.*****, 71:177–180, Jul 1993. 29**

[90] Michael Krauss, Tobias Roth, Sabine Alebrand, Daniel Steil, Mirko Cinchetti, Martin Aeschlimann, and Hans Christian Schneider. **Ultrafast demagnetization of ferromagnetic transition metals: The role of the Coulomb interaction.** ***Phys. Rev. B*****, 80:180407, Nov 2009. 8**

[91] M. H. Kryder, E. C. Gage, T. W. McDaniel, W. A. Challener, R. E. Rottmayer, G. Ju, Y. T. Hsia, and M. F. Erden. **Heat Assisted Magnetic Recording.** ***Proceedings of the IEEE*****, 96(11):1810–1835, Nov 2008. 4, 5, 21**

[92] T. Kubacka, J. A. Johnson, M. C. Hoffmann, C. Vicario, S. de Jong, P. Beaud, S. Grübel, S.-W. Huang, L. Huber, L. Patthey, Y.-D. Chuang, J. J. Turner, G. L. Dakovski, W.-S. Lee, M. P. Minitti, W. Schlotter, R. G. Moore, C. P. Hauri, S. M. Koohpayeh, V. Scagnoli, G. Ingold, S. L. Johnson, and U. Staub. **Large-Amplitude Spin Dynamics Driven by a THz Pulse in Resonance with an Electromagnon.** ***Science*****, 343(6177):1333–1336, 2014. 6**

[93] M. D. Kuz'min. **Shape of Temperature Dependence of Spontaneous Magnetization of Ferromagnets: Quantitative Analysis.** ***Phys. Rev. Lett.*****, 94:107204, Mar 2005. 74**

[94] Y. O. Kvashnin, W. Sun, I. Di Marco, and O. Eriksson. **Electronic topological transition and noncollinear magnetism in compressed hcp Co.** ***Phys. Rev. B*****, 92:134422, Oct 2015. 49, 60, 61, 63, 67**

[95] M. A. Laguna-Marco, J. Chaboy, and C. Piquer. **Experimental determination of the $R(5d)$–$T(3d)$ hybridization in rare-earth intermetallics.** ***Phys. Rev. B*****, 77:125132, Mar 2008. 107**

[96] C-H. Lambert, S. Mangin, B. S. D. Ch. S. Varaprasad, Y. K. Takahashi, M. Hehn, M. Cinchetti, G. Malinowski, K. Hono, Y. Fainman, M. Aeschlimann, and E. E. Fullerton. **All-optical control of ferromagnetic thin films and nanostructures.** ***Science*****, 345(6202):1337–1340, 2014. ii, 6, 7, 8, 80, 94, 97**

[97] H. Landolt, R. Börnstein, K. H. Hellwege, Manfred Böhn, M. Schulz, Harald Weiss, and O. Madelung. ***Landolt-Börnstein numerical data and functional relationships in science and technology. Group 3, Vol. 17, Group 3, Vol. 17,.*** **Springer, Berlin, 1985. 48**

[98] L. Le Guyader, M. Savoini, S. El Moussaoui, M. Buzzi, A. Tsukamoto, A. Itoh, A. Kirilyuk, T. Rasing, A. V. Kimel, and F. Nolting. **Nanoscale sub-100 picosecond all-optical magnetization switching in GdFeCo microstructures.** ***Nature Communications*****, 6:5839 EP –, Jan 2015. Article. 81**

[99] Kyung-Jin Lee, Alina Deac, Olivier Redon, Jean-Pierre Nozieres, and Bernard Dieny. **Excitations of incoherent spin-waves due to spin-transfer torque.** ***Nat Mater*****, 3(12):877–881, Dec 2004. 55**

[100] A.I. Liechtenstein, M.I. Katsnelson, V.P. Antropov, and V.A. Gubanov. **Local spin density functional approach to the theory of exchange interactions in ferromagnetic metals and alloys.** ***Journal of Magnetism and Magnetic Materials*****, 67(1):65 – 74, 1987. 34, 39, 40, 60, 102**

[101] Tian-Min Liu, Tianhan Wang, Alexander H. Reid, Matteo Savoini, Xiaofei Wu, Benny Koene, Patrick Granitzka, Catherine E. Graves, Daniel J. Higley, Zhao Chen, Gary Razinskas, Markus Hantschmann, Andreas Scherz, Joachim Sthr, Arata Tsukamoto, Bert Hecht, Alexey V. Kimel, Andrei Kirilyuk, Theo Rasing, and Hermann A. Drr. **Nanoscale Confinement of All-Optical Magnetic Switching in TbFeCo - Competition with Nanoscale Heterogeneity.** ***Nano Letters*****, 15(10):6862–6868, 2015. PMID: 26312732. 13**

[102] PerOlov Lwdin. **On the NonOrthogonality Problem Connected with the Use of Atomic Wave Functions in the Theory of Molecules and Crystals.** ***The Journal of Chemical Physics*****, 18(3), 1950. 35**

[103] S. Mangin, M. Gottwald, C-H. Lambert, D. Steil, V. Uhl, L. Pang, M. Hehn, S. Alebrand, M. Cinchetti, G. Malinowski, Y. Fainman, M. Aeschlimann, and E. E. Fullerton. **Engineered materials for all-optical helicity-dependent magnetic switching.** ***Nat Mater*****, 13:286–292, Mar 2014. ii, 6, 80, 81, 82, 97**

[104] M. Mansmann and W. E. Wallace. **Magnetic Properties of GdFe2 and DyFe2.** ***The Journal of Chemical Physics*****, 40(4):1167–1168, 1964. 107**

[105] M. Mansuripur. **Mean-Field Analysis of Amorphous Rare Earth-Transition Metal Alloys for Thermomagnetic Recording.** ***IEEE Trans. Magn.*****, 22:1, 1986. 21, 83, 85, 94**

[106] M. Mansuripur. ***The Physical Principles of Magneto-optical Recording.*** **Cambridge University Press, Cambrige, UK, 1995. 21, 83**

[107] R. Medapalli, D. Afanasiev, D. Kim, Y. Quessab, S. A. Monotoya, A. Kirilyuk, T. Rasing, A. V. Kimel, and E. E. Fullerton. **Mechanism of all-optical control of ferromagnetic multilayers with circularly polarized light.** ***arXiv:1607.02505v1 [cond-mat.mtrl-sci].*** **10**

[108] J. Mendil, P. Nieves, O. Chubykalo-Fesenko, J. Walowski, T. Santos, S. Pisana, and M. MÃŒnzenberg. **Resolving the role of femtosecond heated electrons in ultrafast spin dynamics.** ***Sci Rep*****, 4:3980, Feb 2014. 24496221[pmid]. 6, 32, 89, 97, 118**

[109] J. H. Mentink, J. Hellsvik, D. V. Afanasiev, B. A. Ivanov, A. Kirilyuk, A. V. Kimel, O. Eriksson, M. I. Katsnelson, and Th. Rasing. **Ultrafast Spin Dynamics in Multisublattice Magnets. Jan 2012. 8**

[110] James L. Mercer and M. Y. Chou. **Tight-binding model with intra-atomic matrix elements.** ***Phys. Rev. B*****, 49:8506–8509, Mar 1994. 36**

[111] Nicholas Metropolis, Arianna W. Rosenbluth, Marshall N. Rosenbluth, Augusta H. Teller, and Edward Teller. **Equation of State Calculations by Fast Computing Machines.** ***The Journal of Chemical Physics*****, 21(6):1087–1092, 1953. 26**

[112] Maria Miasek. **Tight-Binding Method for Hexagonal Close-Packed Structure.** ***Phys. Rev.*****, 107:92–95, Jul 1957. 49**

[113] R. Moreno, R. F. L. Evans, S. Khmelevskyi, M. C. Muñoz, R. W. Chantrell, and O. Chubykalo-Fesenko. **Temperature-dependent exchange stiffness and domain wall width in Co.** ***Phys. Rev. B*****, 94:104433, Sep 2016. 4, 24, 34, 54**

[114] O. N. Mryasov, U. Nowak, K. Y. Guslienko, and R. W. Chantrell. **Temperature-dependent magnetic properties of FePt: Effective spin Hamiltonian model.** ***EPL (Europhysics Letters)*****, 69(5):805, 2005. 24**

[115] G. M. Muller, J. Walowski, M. Djordjevic, G.-X. Miao, A. Gupta, A. V. Ramos, K. Gehrke, V. Moshnyaga, K. Samwer, J. Schmalhorst,

A. Thomas, A. Hutten, G. Reiss, J. S. Moodera, and M. Munzenberg. **Spin polarization in half-metals probed by femtosecond spin excitation.** ***Nat Mater*****, 8(1):56–61, Jan 2009. 6**

[**116**] Adil Murtaza, Sen Yang, Chao Zhou, Muhammad Tahir Khan, Awais Ghani, Fanghua Tian, Jieqiong Wang, Xiaoping Song, Matthrew Suchomel, and Yang Ren. **Structural and magnetic properties of morphotropic phase boundary involved Tb1xGdxFe2 compounds.** ***Journal of Alloys and Compounds*****, 680:177 – 181, 2016. 105, 107, 108, 110**

[**117**] H. P. Myers and W. Sucksmith. **The Spontaneous Magnetization of Cobalt.** ***Proceedings of the Royal Society of London A: Mathematical, Physical and Engineering Sciences*****, 207(1091):427–446, 1951. 63**

[**118**] P. Nieves. ***Micromagnetic models for high-temperature magnetization dynamics.*** **PhD thesis, Department Condensed Matter, Universidad Autonoma de Madrid, May 2015. 30, 32**

[**119**] P. Nieves and O. Chubykalo-Fesenko. **Modeling of Ultrafast Heat- and Field-Assisted Magnetization Dynamics in FePt.** ***Phys. Rev. Applied*****, 5:014006, Jan 2016. 6, 8, 9, 91**

[**120**] R.C. O'Handley. ***Modern Magnetic Materials: Principles and Applications.*** **Wiley, 1999. 56, 63, 68, 86**

[**121**] L Oroszlany and L Szunyogh. **Private communication. 40**

[**122**] T. A. Ostler, U. Atxitia, and R. W. Chantrell. ***Unpublished*****, 2017. 91**

[**123**] T.A. Ostler, J. Barker, R.F.L. Evans, R.W. Chantrell, U. Atxitia, O. Chubykalo-Fesenko, S. El Moussaoui, L. Le Guyader, E. Mengotti, L.J. Heyderman, F. Nolting, A. Tsukamoto, A. Itoh, D. Afanasiev, B.A. Ivanov, A.M. Kalashnikova, K. Vahaplar, J. Mentink, A. Kirilyuk, Th. Rasing, and A.V. Kimel. **Ultrafast heating as a sufficient stimulus for magnetization reversal in a ferrimagnet.** ***Nature Communications*****, 3:666, 2012. ii, 4, 5, 7, 8, 11, 12, 14, 15, 21, 32, 80, 81, 88, 94, 97, 99, 120**

[**124**] Thomas A. Ostler, Richard F. L. Evans, Roy W. Chantrell, Unai Atxitia, Oksana Chubykalo-Fesenko, Ilie Radu, Radu Abrudan, Florin Radu, Arata Tsukamoto, A. Itoh, Andrei Kirilyuk, Theo Rasing, and Alexey Kimel. **Crystallographically amorphous ferrimagnetic alloys: Comparing a localized atomistic spin model with experiments.** ***Phys. Rev. B*****, 84:024407, Jul 2011. 16, 21, 83, 86**

[125] A Oswald, R Zeller, P J Braspenning, and P H Dederichs. **Interaction of magnetic impurities in Cu and Ag.** ***Journal of Physics F: Metal Physics*****, 15(1):193, 1985. 40**

[126] M. Pajda, J. Kudrnovský, I. Turek, V. Drchal, and P. Bruno. ***Ab initio*** **calculations of exchange interactions, spin-wave stiffness constants, and Curie temperatures of Fe, Co, and Ni.** ***Phys. Rev. B*****, 64:174402, Oct 2001. 34, 39, 49, 51, 52, 53, 60, 61, 69, 116**

[127] D. A. Papaconstantopoulos. ***Handbook of the band structure of elemental solids.*** **Plenum Press, New York, 1986. 37, 42, 48, 49, 54, 63, 66**

[128] D A Papaconstantopoulos and M J Mehl. **The SlaterKoster tight-binding method: a computationally efficient and accurate approach.** ***Journal of Physics: Condensed Matter*****, 15(10):R413, 2003. 21, 34, 38**

[129] S. Pathak and M. Sharma. **Electron Spin Resonance In Electrodeposited Cobalt Nanowire Arrays.** ***Advanced Materials*****, 3(6):526–532, 2012. 55**

[130] J. L. Pérez-Díaz and M. C. Muñoz. **Spin-polarized electrons at interfaces: Co/Cu systems.** ***Phys. Rev. B*****, 50:8824–8831, Sep 1994. 42**

[131] B. Pfau, S. Schaffert, L. MÃŒller, C. Gutt, A. Al-Shemmary, F. BÃŒttner, R. Delaunay, S. DÃŒsterer, S. Flewett, R. FrÃ¶mter, J. Geilhufe, E. Guehrs, C. M. GÃŒnther, R. Hawaldar, M. Hille, N. Jaouen, A. Kobs, K. Li, J. Mohanty, H. Redlin, W. F. Schlotter, D. Stickler, R. Treusch, B. Vodungbo, M. KlÃ€ui, H. P. Oepen, J. LÃŒning, G. GrÃŒbel, and S. Eisebitt. **Ultrafast optical demagnetization manipulates nanoscale spin structure in domain walls.** ***Nature Communications*****, 3:1100 EP –, Oct 2012. Article. 56**

[132] I L Prejbeanu, M Kerekes, R C Sousa, H Sibuet, O Redon, B Dieny, and J P Nozires. **Thermally assisted MRAM.** ***Journal of Physics: Condensed Matter*****, 19(16):165218, 2007. 4**

[133] I. L. Prejbeanu, W. Kula, K. Ounadjela, R. C. Sousa, O. Redon, B. Dieny, and J. P. Nozieres. **Thermally assisted switching in exchange-biased storage layer magnetic tunnel junctions.** ***IEEE Transactions on Magnetics*****, 40(4):2625–2627, July 2004. 5**

[134] T. Q. Qiu and C. L. Tien. **Heat Transfer Mechanisms During Short-Pulse Laser Heating of Metals.** ***Journal of Heat Transfer*****, 115(4):835–841, Nov 1993. 31**

[135] I. Radu, K. Vahaplar, C. Stamm, T. Kachel, N. Pontius, H. A. Durr, T. A. Ostler, J. Barker, R. F. L. Evans, R. W. Chantrell, A. Tsukamoto, A. Itoh, A. Kirilyuk, Th. Rasing, and A. V. Kimel. **Transient ferromagnetic-like state mediating ultrafast reversal of antiferromagnetically coupled spins.** ***Nature*****, 472:205, 2011. 7, 8, 10, 11, 12, 32, 81, 94, 99, 120**

[136] A.V. Ruban and H.L. Skriver. **Calculated surface segregation in transition metal alloys.** ***Computational Materials Science*****, 15(2):119 – 143, 1999. 60, 63**

[137] T. L. Perel'man S. I. Anisimov, B. L. Kapeliovich. **Electron emission from metal surfaces exposed to ultrashort laser pulses.** ***Journal of Experimental and Theoretical Physics*****, 39(2):375, 1976. 31**

[138] G. Salvatella, R. Gort, K. BÃŒhlmann, S. DÃ€ster, A. Vaterlaus, and Y. Acremann. **Ultrafast demagnetization by hot electrons: Diffusion or super-diffusion?** ***Struct Dyn*****, 3(5):055101, Sep 2016. 1.4964892[PII]. 31**

[139] F. Schlickeiser, U. Atxitia, S. Wienholdt, D. Hinzke, O. Chubykalo-Fesenko, and U. Nowak. **Temperature dependence of the frequencies and effective damping parameters of ferrimagnetic resonance.** ***Phys. Rev. B*****, 86:214416, Dec 2012. 14**

[140] A. Scholl, L. Baumgarten, R. Jacquemin, and W. Eberhardt. **Ultrafast Spin Dynamics of Ferromagnetic Thin Films Observed by fs Spin-Resolved Two-Photon Photoemission.** ***Phys. Rev. Lett.*****, 79:5146–5149, Dec 1997. 6**

[141] K Schwarz, P Mohn, P Blaha, and J Kubler. **Electronic and magnetic structure of BCC Fe-Co alloys from band theory.** ***Journal of Physics F: Metal Physics*****, 14(11):2659, 1984. 24**

[142] A. Secchi, S. Brener, A.I. Lichtenstein, and M.I. Katsnelson. **Non-equilibrium magnetic interactions in strongly correlated systems.** ***Annals of Physics*****, 333:221 – 271, 2013. 34**

[143] G. Shirane, V. J. Minkiewicz, and R. Nathans. **Spin Waves in 3d Metals.** ***Journal of Applied Physics*****, 39(2):383–390, 1968. 55, 68, 75**

[144] J. C. Slater and G. F. Koster. **Simplified LCAO Method for the Periodic Potential Problem.** ***Phys. Rev.*****, 94:1498–1524, Jun 1954. 21, 34, 35, 37**

[145] C. D. Stanciu, F. Hansteen, A. V. Kimel, A. Kirilyuk, A. Tsukamoto, A. Itoh, and Th. Rasing. **All-Optical Magnetic Recording with Circularly Polarized Light.** ***Phys. Rev. Lett.*****, page 047601, 2007. ii, 5, 6, 7, 8, 9, 21, 80, 81**

[146] J. Staunton, B.L. Gyorffy, A.J. Pindor, G.M. Stocks, and H. Winter. **The disordered local moment picture of itinerant magnetism at finite temperatures.** ***Journal of Magnetism and Magnetic Materials*****, 45(1):15 – 22, 1984. 62, 102**

[147] D. Steiauf and M. Fähnle. **Elliott-Yafet mechanism and the discussion of femtosecond magnetization dynamics.** ***Phys. Rev. B*****, 79:140401, Apr 2009. 8, 25**

[148] A. Stupakiewicz, K. Szerenos, D. Afanasiev, A. Kirilyuk, and A. V. Kimel. **Ultrafast nonthermal photo-magnetic recording in a transparent medium.** ***Nature*****, 542(7639):71–74, Feb 2017. Letter. 6**

[149] J. Sthr and H.C. Siegmann. ***Magnetism.*** **Springer-Verlag, Berlin, 2006. 3, 16, 21, 33, 48, 82, 85**

[150] O. J. Suarez, P. Nieves, D. Laroze, D. Altbir, and O. Chubykalo-Fesenko. **Ultrafast relaxation rates and reversal time in disordered ferrimagnets.** ***Phys. Rev. B*****, 92:144425, Oct 2015. 17, 81**

[151] W. Sucksmith and J. E. Thompson. **The Magnetic Anisotropy of Cobalt.** ***Proceedings of the Royal Society of London A: Mathematical, Physical and Engineering Sciences*****, 225(1162):362–375, 1954. 55**

[152] R. C. Taylor and A. Gangulee. **Magnetic properties of the $3d$ transition metals in the amorphous ternary alloys: $Gd_{0.2}(Fe_xCo_{1-x})_{0.8}$, $Gd_{0.2}(Co_xNi_{1-x})_{0.8}$, and $Gd_{0.2}(Fe_xNi_{1-x})_{0.8}$.** ***Phys. Rev. B*****, 22:1320–1326, Aug 1980. 85, 94**

[153] W. C. Thoburn, S. Legvold, and F. H. Spedding. **Magnetic Properties of Terbium Metal.** ***Phys. Rev.*****, 112:56–58, Oct 1958. 86**

[154] P. Tolédano, G. Krexner, M. Prem, H.-P. Weber, and V. P. Dmitriev. **Theory of the martensitic transformation in cobalt.** ***Phys. Rev. B*****, 64:144104, Sep 2001. 53, 55, 73**

[155] Arata Tsukamoto, Tetsuya Sato, Shingo Toriumi, and Akiyoshi Itoh. **Precessional switching by ultrashort pulse laser: Beyond room temperature ferromagnetic resonance limit.** ***Journal of Applied Physics*****, 109(7):07D302, 2011. 14**

[156] I. Turek, J. Kudrnovsk, V. Drchal, P. Bruno, and S. Blgel. **Ab initio theory of exchange interactions in itinerant magnets.** ***physica status solidi (b)*****, 236(2):318–324, 2003. 34, 49, 51, 53, 54, 60, 61, 62, 63, 67, 68, 71, 72**

[157] K. Uchida, S. Takahashi, K. Harii, J. Ieda, W. Koshibae, K. Ando, S. Maekawa, and E. Saitoh. **Observation of the spin Seebeck effect.** ***Nature*****, 455:778–781, Oct 2008. 4**

[158] K. Vahaplar, A. M. Kalashnikova, A. V. Kimel, S. Gerlach, D. Hinzke, U. Nowak, R. Chantrell, A. Tsukamoto, A. Itoh, A. Kirilyuk, and Th. Rasing. **All-optical magnetization reversal by circularly polarized laser pulses: Experiment and multiscale modeling.** ***Phys. Rev. B*****, 85:104402, Mar 2012. 7, 9, 91, 97**

[159] S. P. Vernon, S. M. Lindsay, and M. B. Stearns. **Brillouin scattering from thermal magnons in a thin Co film.** ***Phys. Rev. B*****, 29:4439–4442, Apr 1984. 55**

[160] G. Vrtesy and I. Tom. **Temperature dependence of the exchange parameter and domain-wall properties.** ***Journal of Applied Physics*****, 93(7):4040–4044, 2003. 4, 56**

[161] J. Wang, Ł. Cywinski, C. Sun, J. Kono, H. Munekata, and L. J. Sham. **Femtosecond demagnetization and hot-hole relaxation in ferromagnetic $Ga_{1-x}Mn_xAs$.** ***Phys. Rev. B*****, 77:235308, Jun 2008. 6**

[162] J.A. Weil and J.R. Bolton. ***Electron Paramagnetic Resonance: Elementary Theory and Practical Applications.*** **Wiley, 2007. 85, 105**

[163] S. Wienholdt, D. Hinzke, K. Carva, P. M. Oppeneer, and U. Nowak. **Orbital-resolved spin model for thermal magnetization switching in rare-earth-based ferrimagnets.** ***Phys. Rev. B*****, 88:020406, Jul 2013. 98, 104, 105, 116, 122**

[164] R. B. Wilson, J. Gorchon, Y. Yang, C.-H. Lambert, S. Salahuddin, and J. Bokor. **Ultrafast Magnetic Switching of GdFeCo with Electronic Heat Currents.** ***arXiv:1609.05155v1 [cond-mat.mtrl-sci].*** **12, 18, 97**

[165] E. P. Wohlfarth. ***Ferromagnetic Materials.*** **Elsevier, 1980. 48, 85, 104**

[166] A. Q. Wu, Y. Kubota, T. Klemmer, T. Rausch, C. Peng, Y. Peng, D. Karns, X. Zhu, Y. Ding, E. K. C. Chang, Y. Zhao, H. Zhou, K. Gao, J. U. Thiele, M. Seigler, G. Ju, and E. Gage. **HAMR Areal Density**

Demonstration of 1+ Tbpsi on Spinstand. ***IEEE Transactions on Magnetics*****, 49(2):779–782, Feb 2013. 13**

[**167**] C. Xu, T. A. Ostler, and R. W. Chantrell**. Thermally induced magnetization switching in Gd/Fe multilayers.** ***Phys. Rev. B*****, 93:054302, Feb 2016. 6, 80, 99**

[**168**] A. Yakoubi, O. Baraka, and B. Bouhafs**. Structural and electronic properties of the Laves phase based on rare earth type BaM2 (M = Rh, Pd, Pt).** ***Results in Physics*****, 2:58 – 65, 2012. 100**

[**169**] Hongxin Yang, André Thiaville, Stanislas Rohart, Albert Fert, and Mairbek Chshiev**. Anatomy of Dzyaloshinskii-Moriya Interaction at** Co/Pt **Interfaces.** ***Phys. Rev. Lett.*****, 115:267210, Dec 2015. 24**

[**170**] Y. Yang, R. B. Wilson, J. Gorchon, C.-H. Lambert, S. Salahuddin, and J. Bokor**. Ultrafast Magnetization Reversal by Picosecond Electrical Pulses. 5, 12**